Supporting Information for

Impact of γ-Amino Acid Residue Preorganization on α/γ-Peptide Foldamer Helicity in Aqueous Solution

Brian F. Fisher, Samuel H. Gellman

Table of Contents

I. Materials and Instrumentation

Materials and reagents

Most solvents and reagents used were purchased from Sigma-Aldrich. Amino acids and coupling reagents were purchased from Chem-Impex. International, Inc. Fmoc-γ^4-amino acids were purchased from PolyPeptide Group. Solid-phase peptide synthesis (SPPS) resins were purchased from EMD Millipore. Sigma-Aldrich ACS-grade DMF was used as a washing solvent during SPPS, and Sigma-Aldrich biotech-grade DMF was used during amino acid coupling. Silica column chromatography was performed using Sigma-Aldrich technical grade silica gel, pore size 60 Å, 40-63 μm mesh size. TLC was performed using SiliCycle Siliaplate glass-backed TLC plates, 60 Å pore size, 250 μm thickness, F-254 indicator. Visualization of TLC plates was performed with 254 nm UV light, ninhydrin stain (1.5 g ninhydrin in 100 mL butanol and 3 mL AcOH), $KMnO_4$ stain (1.5 g $KMnO_4$, 10 g K_2CO_3, and 1.25 mL 10% NaOH in 200 mL H_2O), PMA stain (10% PMA in EtOH), or p-anisaldehdye stain (135 mL EtOH, 5 mL H_2SO_4, 1.5 mL AcOH, 3.7 mL p-anisaldehyde).

Instrumentation

Microwave-assisted SPPS was performed in Torviq polypropylene syringes fitted with a porous polypropylene disc at the bottom using a CEM MARS microwave system. Preparative HPLC was performed using a Shimadzu HPLC system (SCL-10VP system controller, LC-6AD pumps, SIL-10ADVP autosampler, SPD-10VP UV-vis detector, FRC-10A fraction collector) equipped with a Discovery BIO Wide Pore C5 column (10 μm particle size, 21.2 mm × 250 mm,) operating at 13 mL/min. Peptide purity and concentration were checked with a Waters Acquity H-Class UPLC equipped with an Acquity UPLC BEH C18 column (130 Å pore size, 1.7 μm particle size, 2.1 mm × 50 mm) operating at 0.5 mL/min. Measurements of pH were performed using a Fisher Scientific Accumet AB15 Basic pH meter. Circular dichroism measurements were conducted on an Aviv Biomedical Model 420. UV-vis measurements were performed on a Varian Cary 50 UV-vis spectrometer.

This material is based upon work supported by the National Science Foundation and National Institutes of Health under the following grant numbers. Any opinions, findings, and conclusions or recommendations expressed in this material are those of the authors and do not necessarily reflect the views of the National Science Foundation.

Instrument acknowledgements

Instrument Name	Instrument Type	**Grant**	**Award year**
Bruker AC-300	NMR spectrometer	NSF CHE-9208463	1993
Bruker AC-300	NMR spectrometer	NIH S10 RR08389-01	1993
Varian INOVA-600	NMR spectrometer	NIH S10 RR13866-01	2000
Bruker Avance III-400	NMR spectrometer	NSF CHE-1048642	2010
Bruker Avance III-500	NMR spectrometer	Generous gift from Paul J. Bender	2012
Bruker Avance III-HD 600	NMR spectrometer	NIH S10 OD012245	2013
Waters Micromass LCT	Mass spectrometer	NSF CHE-9974839	1999
Bruker ULTRAFLEX-III MALDI	MALDI-TOF-MS	NIH NCRR 1S10RR024601-01	2008
Waters Acquity H-Class	UPLC	DARPA N66001-15-2-4023	2014

II. Synthesis

A. Nomenclature

Abbrev.	**Full name**
SPPS	Solid-phase peptide synthesis
HCTU	(2-(6-Chloro-1H-benzotriazole-1-yl)-1,1,3,3-tetramethylaminium hexafluorophosphate)
Cl-HOBt	6-chloro 1-hydroxybenzotriazole
DIEA	Diisopropylethylamine
DMF	Dimethylformamide
TFA	Trifluoroacetic acid
EtOAc	Ethyl acetate
TIPS	Triisopropylsilane
NMI	1-methylimidazole
TEMPO	2,2,6,6-Tetramethyl-1-piperidinyloxy, free radical, 2,2,6,6-Tetramethylpiperidine 1-oxyl
DSS	2,2-Dimethyl-2-silapentane-5-sulfonate
KACHA	**II** from the main text (lysine-like sidechain (**K**) **A**mino **C**yclo**H**exane carboxylic **A**cid)

B. General Procedures

General procedure: Solid-phase peptide synthesis

NovaPEG Rink Amide resin (10 μmol by amine loading [0.45 mml/g], 22.2 mg) is added to a Torviq solid-phase peptide synthesis vessel along with a micro stir bar. Resin is swelled in DMF for at least 30 minutes before beginning synthesis. Fmoc amino acids (4 eq., 40 μmol) and HCTU (3.95 eq., 39 μmol, 16.3 mg) are weighed into 1.7 mL Eppendorf tubes. Amino acid + coupling reagent are pre-activated by adding 400 μL 0.1 M Cl-HOBt in DMF, adding DIEA (8 eq., 80 μmol, 13.9 μL), and vortexing. DMF used to swell the resin is aspirated from the vessel, which is then capped at the bottom, and the pre-activated amino acid solution is added to the vessel. **For coupling of α- or acyclic γ-amino acids:** The reaction vessel is transferred to the microwave reactor, the temperature sensor is placed into the open reaction vessel, and the microwave coupling program is initiated (2 minute ramp to 70°C, 2 minute hold at 70°C). **For coupling of II:** The reaction mixture is stirred for 24 hr at room temperature. After coupling is complete (as determined by Kaiser test), the solution is aspirated from the vessel and the resin is washed 3× with DMF. Deprotection solution (20% piperidine in DMF) is added to the washed resin and microwaved according to the deprotection program (2 minute ramp to 80°C, 2 minute hold at 80°C). During the deprotection, the next amino acid to be added to the peptide is pre-activated. Deprotected resin is washed 6× with DMF, and the next coupling is initiated.

N-terminal acetylation is performed by deprotecting the final Fmoc group and stirring the resin with 50 eq. Ac_2O and 50 eq. DIEA in DMF for 30 minutes. Acetylation solution is aspirated, and the resin is washed 3× with DMF and dried by washing with DCM, MeOH, DCM, MeOH and leaving on the aspirator for 15 minutes.

Cleavage is performed by withdrawing 1 mL of 2.5% TIPS, 2.5% H_2O, 95% TFA into the reaction vessel using the syringe plunger and rocking the vessel for 3 hr. Crude peptide solution is expunged into a 50-mL centrifuge tube, resin is washed 3× with TFA, and TFA is blown off

under a stream of N_2. Once most of the TFA is removed, the crude peptide is precipitated from 20 mL cold Et_2O and pelleted using a centrifuge at 4.3k rpm for 5 minutes. The supernatant Et_2O is decanted, and the crude peptide solid is dried under a stream of N_2.

Crude peptide is prepared for HPLC purification by dissolving the crude solid in H_2O:MeCN (≈1 mL) and transferring to an HPLC vial. HPLC Solvent A is 0.1% TFA in filtered/degassed Millipore H_2O, and Solvent B is 0.1% TFA in acetonitrile. A linear gradient of 10-60%B is used to identify product peaks (determined by MALDI on collected fractions) and to assess proper conditions for further method development.

Collected peptide fractions are frozen over dry ice and lyophilized. Purity is assessed by UPLC using a 10-50%B linear gradient over 5 minutes. Concentration of pure peptide solutions is determined by correlating the integral of the peptide peak in the 275 nm chromatogram with a calibration curve generated by known concentrations of Ac-Tyr-OH. Aliquots for NMR were allocated based on concentration determined this way (which agrees with concentration measurement by UV-vis absorbance at 275 nm and ERETIC[S1]) and lyophilized.

C. Procedures for Synthesis

Compounds listed in the supporting information but not in the main text are prefixed with "S" to denote them separately from the peptides analyzed in the main text.

S1: 6-(Boc-amino)-1-hexanol

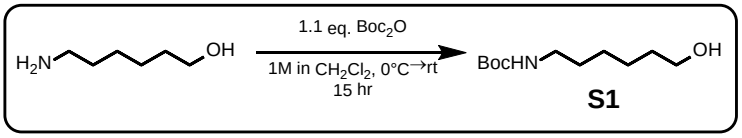

6-Amino-1-hexanol (100 mmol, 11.7 g) was dissolved in CH_2Cl_2 (100 mL) and cooled to 0°C in an ice bath. Solid Boc_2O (1.1 eq., 110 mmol, 24.0 g) was added and the reaction mixture was stirred overnight (15 hr) at room temperature. Solvent was reduced by rotary evaporation and crude product was extracted with EtOAc from 10 % aqueous citric acid, saturated $NaHCO_3$, and brine. The organic phase was dried over Na_2SO_4 and concentrated by rotary evaporation to yield **S1** quantitatively as a clear viscous oil. **TLC** R_f = 0.27 (10% MeOH in CH_2Cl_2, ninhydrin stain) **^{1}H NMR** (300 MHz, $CDCl_3$) δ 4.53 (s, 1H), 3.64 (t, J = 6.5 Hz, 2H), 3.12 (q, J = 6.6 Hz, 2H), 1.78 – 1.20 (m, 18H). **HRMS** *m/z* (ESI): calc. for $[C_{11}H_{24}NO_3]^+$ ($[M+H]^+$) 218.1751, found 218.1743.

S2: 6-(Boc-amino)-1-hexanal

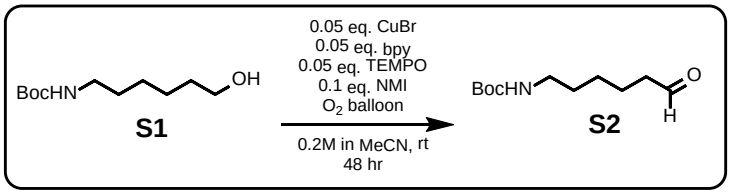

S2 (21.7 g, 100 mmol) was dissolved in 500 mL MeCN in a 1 L round-bottom flask to which CuBr (0.05 eq., 5 mmol, 717 mg), 2,2'-bipyridine (0.05 eq., 5 mmol, 781 mg), TEMPO (0.05 eq., 5 mmol, 781 mg), and 1-methylimidazole (0.1 eq., 10 mmol, 797 μL) in succession. The round-bottom flask was capped with a rubber septum into which the needle of a syringe equipped with an O_2 balloon was inserted. The reaction was stirred at room temperature for 48 hr. After completion, water was added, from which product was extracted 3 × with pentane. The combined organic phases were dried over Na_2SO_4 and solvent was removed by rotary evaporation to yield crude product. Purification was carried out with silica column chromatography eluting with 3:1 hexanes:EtOAc to yield 15.8 g **S2** as a clear oil (73.4 mmol, 73% yield). **TLC** R_f = 0.26 (3:1 hexanes:EtOAc, ninhydrin stain) **^{1}H NMR** (400 MHz, $CDCl_3$) δ 9.76 (t, J = 1.7 Hz, 1H), 4.58 (s, 1H), 3.11 (q, J = 6.7 Hz, 2H), 2.44 (td, J = 7.3, 1.7 Hz, 2H), 1.65 (p, J = 7.4 Hz, 2H), 1.60 – 1.46 (m, 2H), 1.44 (s, 9H), 1.41 – 1.29 (m, 2H). **HRMS** *m/z* (ESI): calc. for $[C_{11}H_{22}NO_3]^+$ ($[M+H]^+$) 216.1595, found 216.1589.

S3: O_2N-[II]-CHO

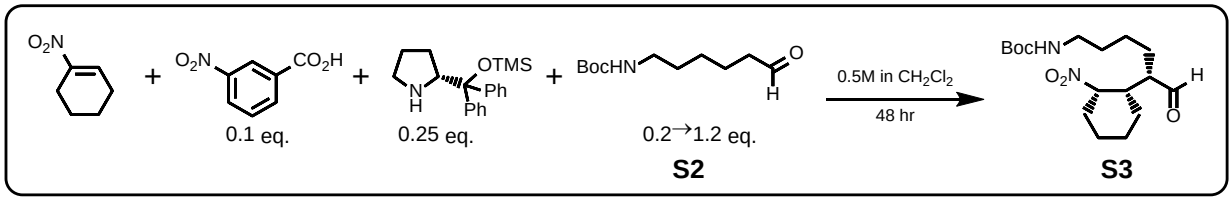

1-Nitrocyclohexene (30 mmol, 3.38 mL) was dissolved in 60 mL CH_2Cl_2, to which was added *m*-nitrobenzoic acid (0.1 eq., 3 mmol, 501 mg), (*R*)-α,α-diphenylprolinol trimethylsilyl ether (0.25 eq., 7.5 mmol, 2.44 g), and **S2** (0.2 eq., 6 mmol, 1.29 g). The round-bottom flask was capped with a rubber septum into which the needle of a syringe containing 9 mL of **S2** (1 eq., 30 mmol, 6.46 g) as a solution in CH_2Cl_2 was inserted. The syringe was attached to a syringe pump (KD Scientific KDS100) dispensing at a rate of 0.3 mL/hr. The reaction vessel was connected to a bubbler under a slight positive pressure of N_2 via Tygon tubing and a needle inserted into the rubber septum to equalize the pressure of the syringe addition. After 48 hr, solvent was removed by rotary evaporation, and crude product was purified by silica column chromatography eluting with 10:1 hexanes:EtOAc to yield 5.03 g **S3** as an orange viscous oil (14.7 mmol, 49% yield). **TLC** R_f = 0.42 (1:1 hexanes:EtOAc, ninhydrin stain) **^{1}H NMR** (400 MHz, $CDCl_3$) δ 9.71 (d, J = 1.8 Hz, 1H), 4.85 (q, J = 3.5 Hz, 1H), 4.51 (s, 1H), 3.10 (q, J = 7.3 Hz, 2H), 2.55 (td, J = 10.3, 9.5, 6.0 Hz, 1H), 2.34 – 2.26 (m, 1H), 2.18 – 2.07 (m, 1H), 1.93 – 1.84 (m, 1H), 1.82 – 1.57 (m, 8H), 1.50 – 1.45 (m, 2H), 1.44 (s, 9H), 1.40 – 1.12 (m, 2H). **HRMS** *m/z* (ESI): calc. for $[C_{17}H_{34}N_3O_5]^+$ ($[M+NH_4]^+$) 360.2493, found 360.2491.

S4: O_2N-[II]-CO_2H

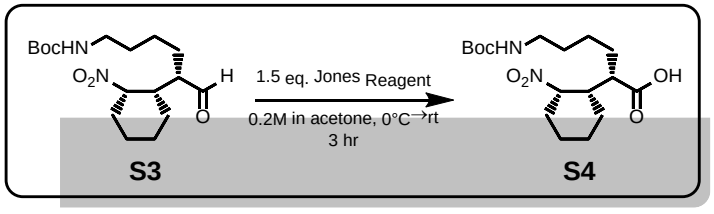

S3 (8.50 mmol, 2.91 g) was dissolved in 40 ml acetone and cooled to 0°C in an ice bath. Jones reagent was prepared fresh (1.5 eq. Jones reagent; 3.80 g $Na_2Cr_2O_7$, 12.8 mL H_2O, 2.7 mL H_2SO_4) and added to the reaction mixture at 0°C. After 5 min, the flask was removed from the ice bath and allowed to warm to room temperature. After 3 hr, the reaction was quenched with excess isopropanol. Solvent was removed by rotary evaporation, and crude product was extracted with EtOAc from 0.5 M HCl three times. The combined organic phases were washed with brine, dried over $MgSO_4$, and concentrated with rotary evaporation to yield crude product as a dark green foam. Crude product was purified by silica column chromatography eluting with 2:1 hexanes EtOAc, then 2:1 hexanes:EtOAc + 2.5% AcOH, to yield 2.58 g **S4** as a pale yellow viscous oil (7.19 mmol, 85% yield). **TLC** R_f = 0.12 (1:1 hexanes:EtOAc, p-anisaldehyde stain) **^{1}H NMR** (400 MHz, $CDCl_3$) δ 9.71 (d, J = 1.8 Hz, 1H), 4.85 (q, J = 3.5 Hz, 1H), 4.51 (s, 1H), 3.10 (q, J = 7.3 Hz, 2H), 2.55 (td, J = 10.3, 9.5, 6.0 Hz, 1H), 2.34 – 2.26 (m, 1H), 2.18 – 2.07 (m, 1H), 1.93 – 1.84 (m, 1H), 1.82 – 1.57 (m, 8H), 1.50 – 1.45 (m, 2H), 1.44 (s, 9H), 1.40 – 1.12 (m, 2H). **HRMS** *m/z* (ESI): calc. for $[C_{17}H_{34}N_3O_5]^+$ ($[M+NH_4]^+$) 360.2493, found 360.2491.

S5: H_2N-[II]-CO_2H

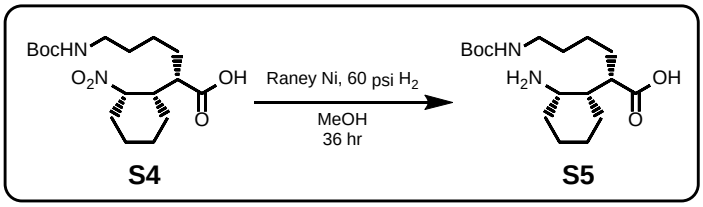

S4 (7.19 mmol, 2.58 g) was dissolved in MeOH and transferred to a 150-mL ChemGlass heavy-walled round-bottom pressure vessel. Two spatula scoops of Raney Ni were transferred to the reaction vessel without washing. Note: sufficient Raney Ni must be used for this step; if insufficient Raney Ni is used, a gray tacky solid is produced from the reaction which could not be assigned to a structure by MS or NMR. The vessel was charged with 60 psi H_2 and stirred for 36 hr. The reaction mixture was filtered through Celite under a gentle stream of N_2 to remove the Raney Ni, which was quickly transferred to a waste container. Rotary evaporation of the filtrate resulted in 1.69 g **S5** green solid (5.15 mmol, 72% yield) which was used without further purification. **TLC** Stained strongly with ninhydrin. **^{1}H NMR** (300 MHz, CD_3OD) δ 3.56 (s, 1H), 3.15 – 2.98 (m, 2H), 2.35 (s, 1H), 1.94 – 1.51 (m, 11H), 1.46 (s, 9H), 1.43 – 1.22 (m, 4H). **HRMS** *m/z* (ESI): calc. for $[C_{17}H_{33}N_2O_4]^+$ ($[M+H]^+$) 329.2435, found 329.2431.

S6: FmocHN-[II]-CO_2H

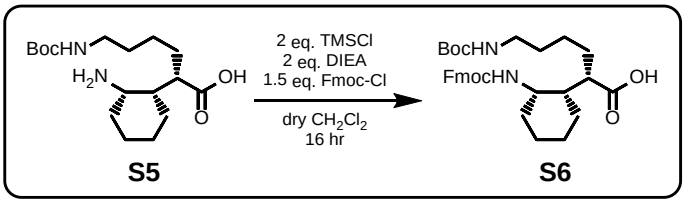

S5 (3.37 mmol, 1.11 g) was suspended in 15 mL CH_2Cl_2 dried with 3 Å molecular sieves. TMSCl (freshly distilled over CaH_2) (2 eq., 6.74 mmol, 856 μL) was added, and the reaction mixture was stirred for 2 hr, during which the suspension became soluble and turned blue-gray.

The mixture was cooled to 0°C in an ice bath, then DIEA (2 eq., 6.74 mmol, 1.17 mL) and Fmoc-Cl (1.5 eq., 5.06 mmol, 1.31 g) were added. The mixture was allowed to warm to room temperature and was stirred overnight (16 hr). The reaction mixture was concentrated by rotary evaporation, diluted with EtOAc, and extracted from 0.1 M HCl. The organic phase was washed with brine, dried over Na_2SO_4, and concentrated by rotary evaporation to provide a gray-brown viscous oil. The crude product was purified by silica column chromatography eluting with 2:1 hexanes:EtOAc then 1:2 hexanes:EtOAc to yield 877 mg **S6** as a pale yellow foam (1.59 mmol, 47%). **TLC** R_f = 0.36 (1:2 hexanes:EtOAc, $KMnO_4$ stain) **^{1}H NMR** (400 MHz, $CDCl_3$) δ 7.76 (d, J = 7.5 Hz, 2H), 7.59 (t, J = 6.6 Hz, 2H), 7.39 (t, J = 7.4 Hz, 2H), 7.30 (t, J = 7.5 Hz, 2H), 5.28 (s, 1H), 4.61 (s, 1H), 4.39 (d, J = 7.2 Hz, 2H), 4.23 (t, J = 6.9 Hz, 1H), 3.96 (s, 1H), 3.06 (s, 2H), 2.34 – 2.18 (m, 1H), 1.77 (d, J = 22.6 Hz, 4H), 1.61 – 1.45 (m, 10H), 1.42 (s, 9H), 1.28 (s, 2H). **HRMS** *m/z* (ESI): calc. for $[C_{32}H_{41}N_2O_6]^-$ ($[M-H]^-$) 549.2970, found 549.2955.

III. NMR Experimental

A. 1D ^{1}H-NMR Experimental

CD_3OH concentration tests

Samples were analyzed by ^{1}H-NMR at 600 MHz at variable concentrations to qualitatively evaluate the aggregation propensity for the tested α/γ-peptides. Amide resonances changing by greater than 0.025 ppm over at least an order of magnitude concentration range (here, typically 100 μM to 3 mM) is suggestive of non-monomeric aggregation state and difficulty assigning structural features to the propensities of the individual solvated molecules.

Since the peptides are isolated as the TFA salts after HPLC purification, more concentrated peptide solutions in the absence of buffer will be more acidic. This change in pH* ("pH*" is used here to denote that measurements of methanolic solutions were performed using a pH meter electrode with an aqueous reference solution and calibrated to aqueous buffer[S2]) is responsible for changes of amide chemical shift at low (≈100 μM) concentrations. When low-concentration solutions are acidified with HCl in MeOH, the amide chemical shifts match those in the higher concentration (> 1 mM) spectra.

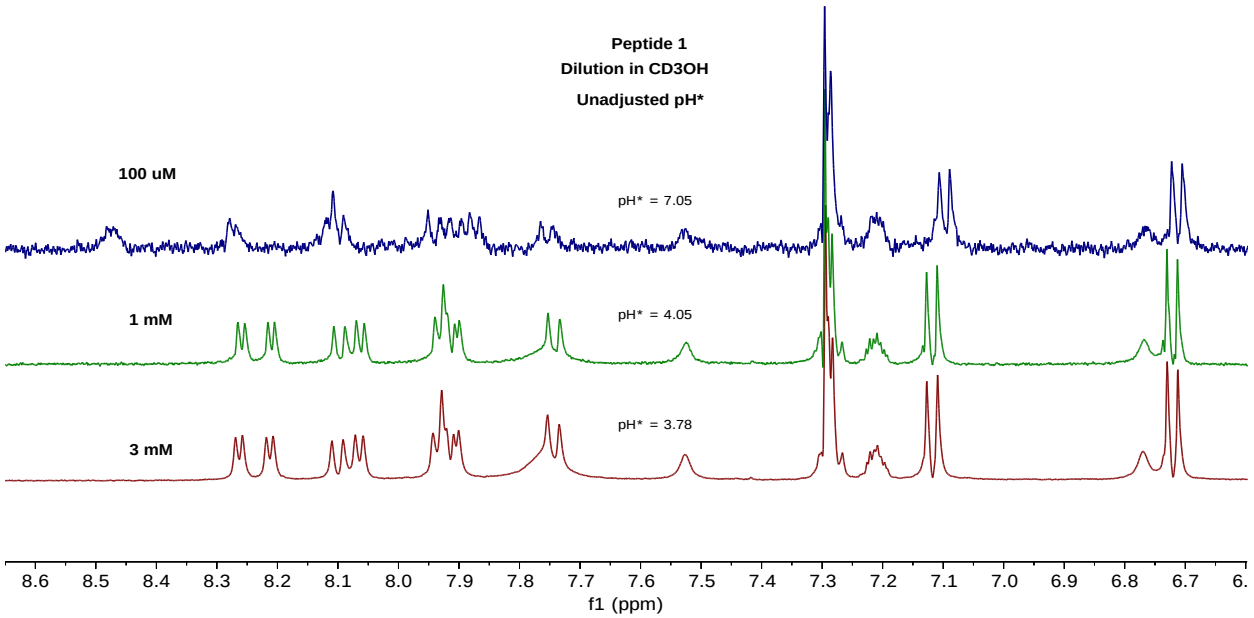

Figure S1: Comparison of the W5es water-suppressed ^{1}H-NMR amide region of peptide **1** in CD_3OH. Lyophilized peptide TFA salts were dissolved directly in CD_3OH to the listed concentration, resulting in the denoted pH* readings.

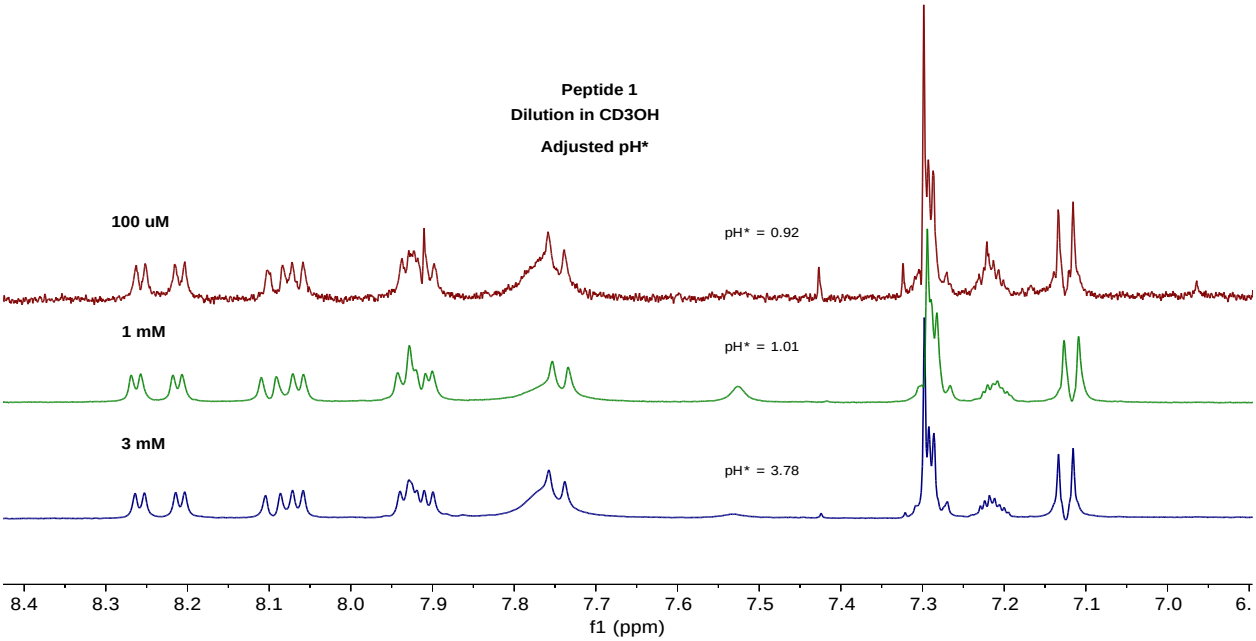

Figure S2: Comparison of the W5es water-suppressed ^{1}H-NMR amide region of peptide **1** in CD_3OH at different peptide concentrations after addition of ≈1 µL of 0.47 M HCl in CH_3OH.

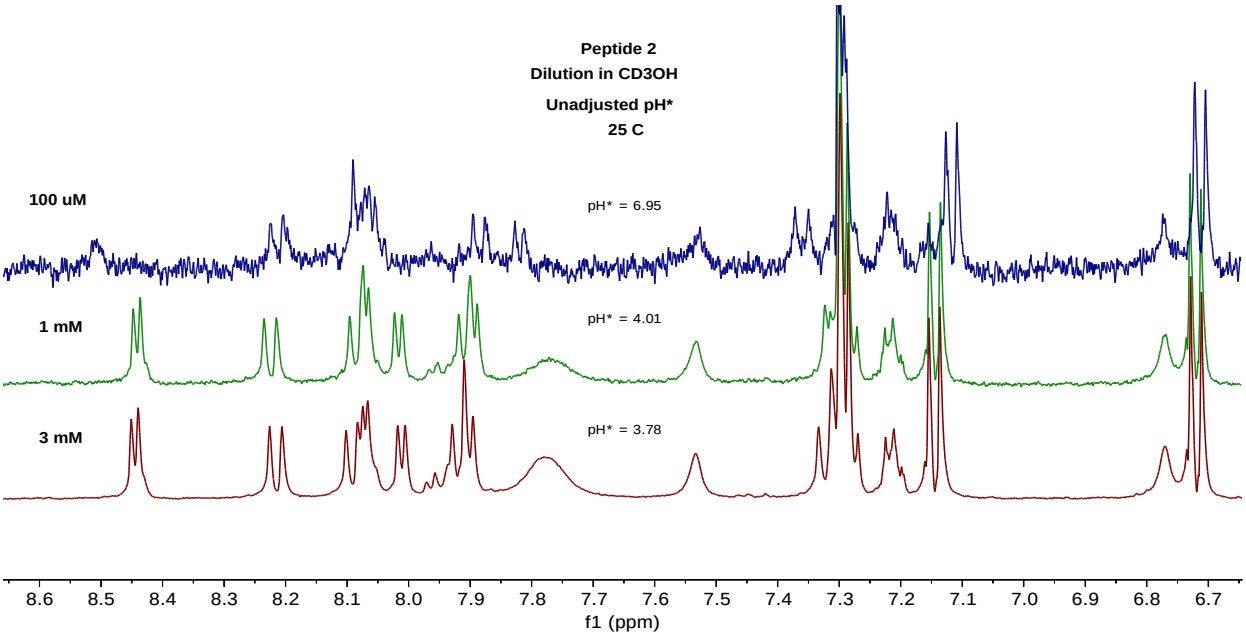

Figure S3: Comparison of the W5es water-suppressed ^{1}H-NMR amide region of peptide **2** in CD_3OH. Lyophilized peptide TFA salts were dissolved directly in CD_3OH to the listed concentration, resulting in the denoted pH* readings.

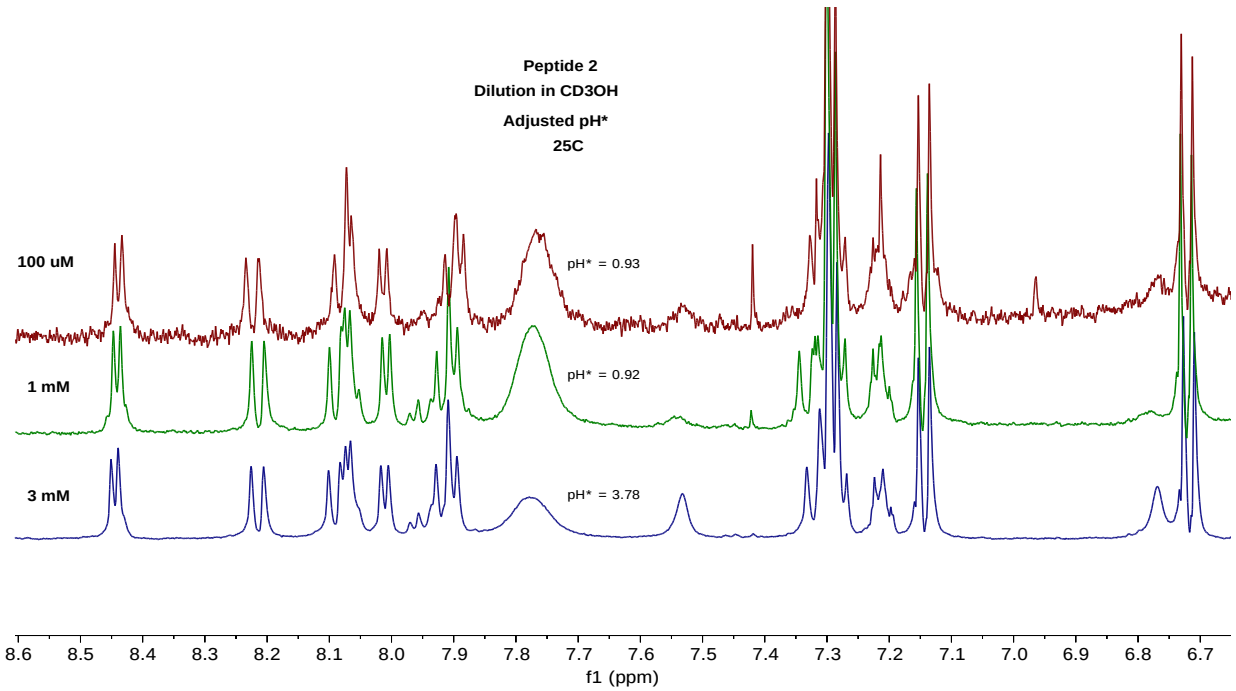

Figure S4: Comparison of the W5es water-suppressed ^{1}H-NMR amide region of peptide **2** in CD_3OH at different peptide concentrations after addition of ≈1 µL of 0.47 M HCl in CH_3OH.

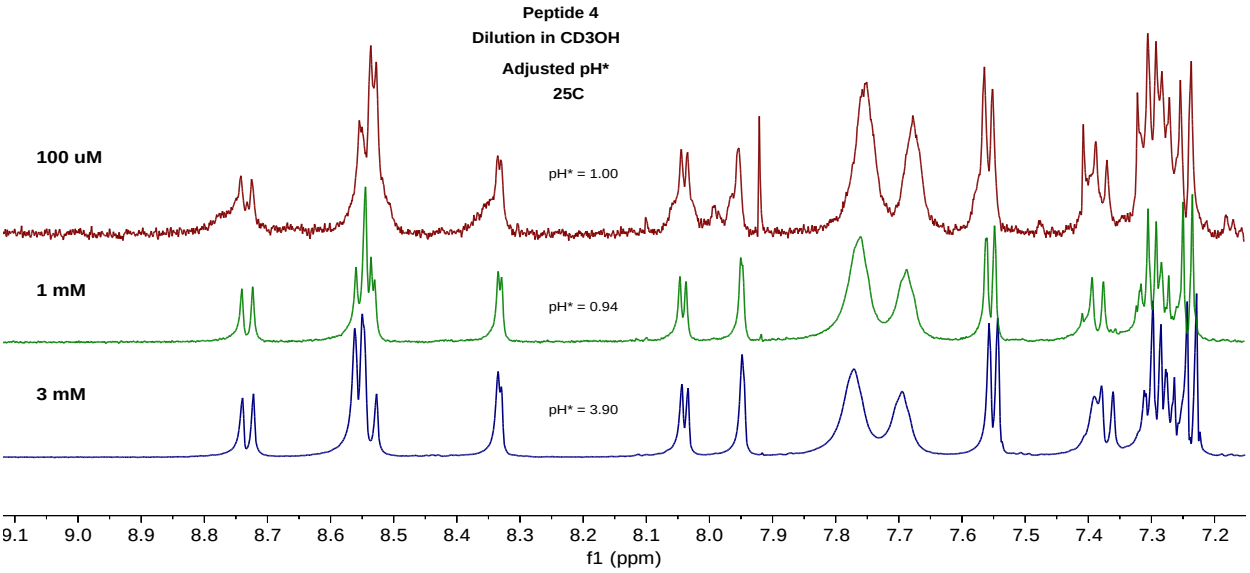

Figure S5: Comparison of the W5es water-suppressed ^{1}H-NMR amide region of peptide **4** in CD_3OH at different peptide concentrations after addition of ≈1 μL of 0.47 M HCl in CH_3OH.

H_2O concentration tests

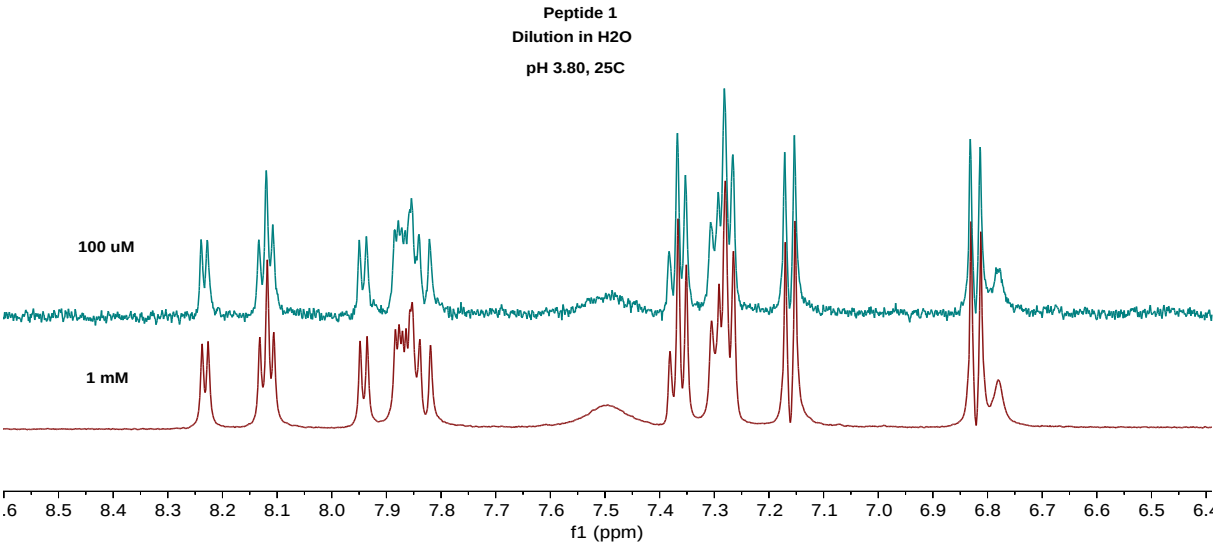

Figure S6: Comparison of the W5es water-suppressed amide region of peptide **1** in water (9:1 H_2O D_2O, 100 mM acetate, pH 3.8, ref. DSS) at different peptide concentrations.

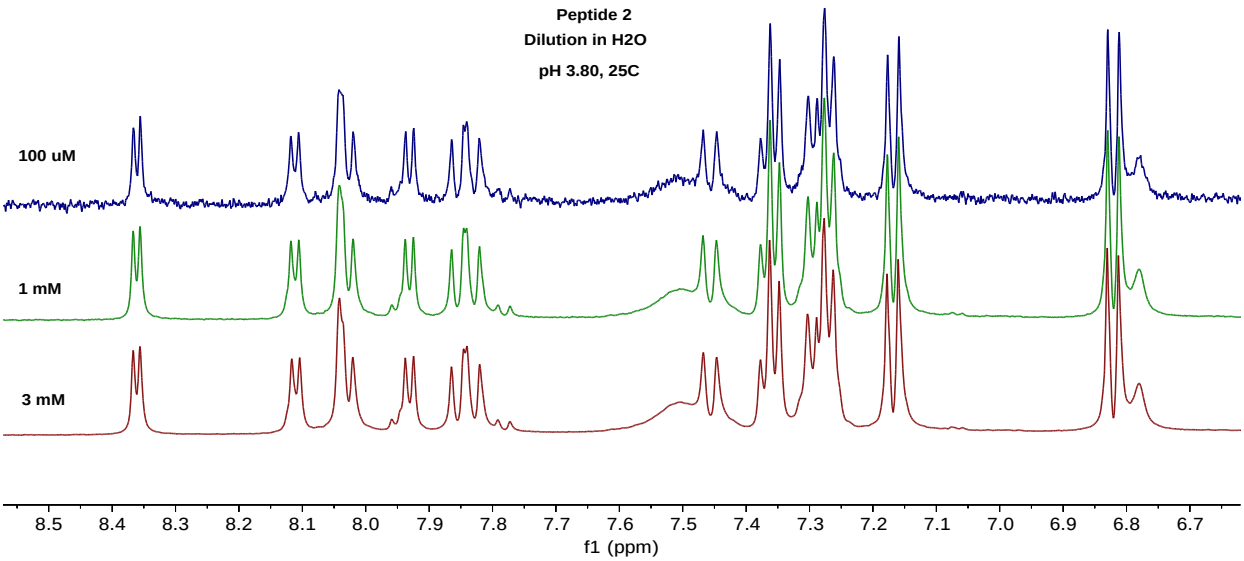

Figure S7: Comparison of the W5es water-suppressed amide region of peptide **2** in water (9:1 H_2O D_2O, 100 mM acetate, pH 3.8, ref. DSS) at different peptide concentrations.

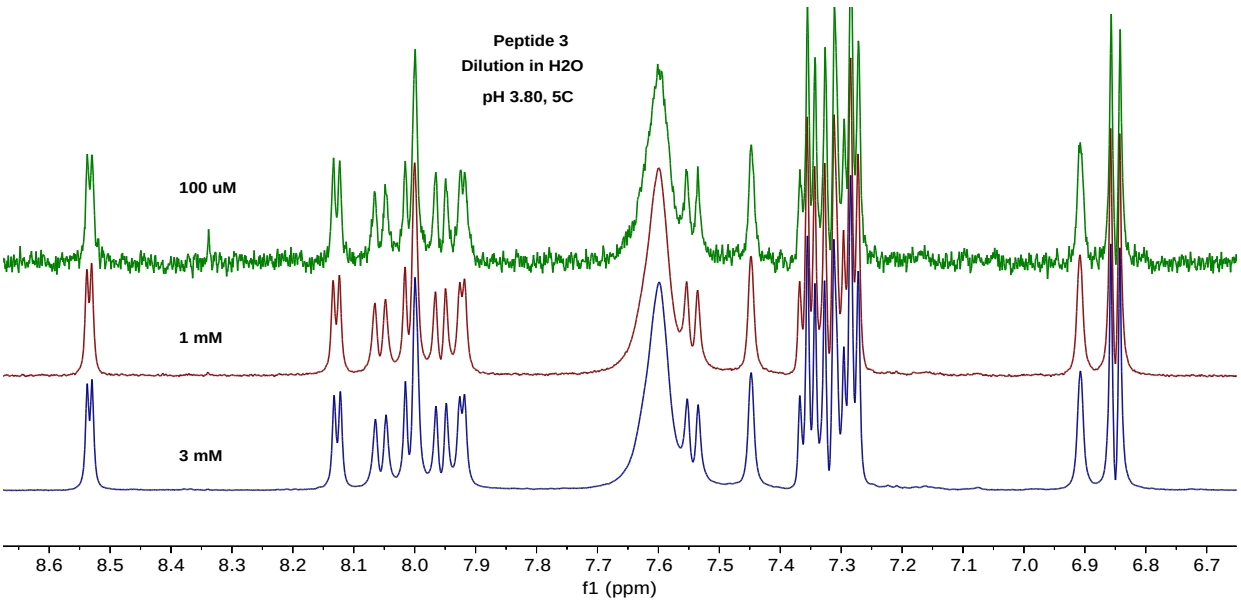

Figure S8: Comparison of the W5es water-suppressed amide region of peptide **3** in water (9:1 H_2O D_2O, 100 mM acetate, pH 3.8, ref. DSS) at different peptide concentrations.

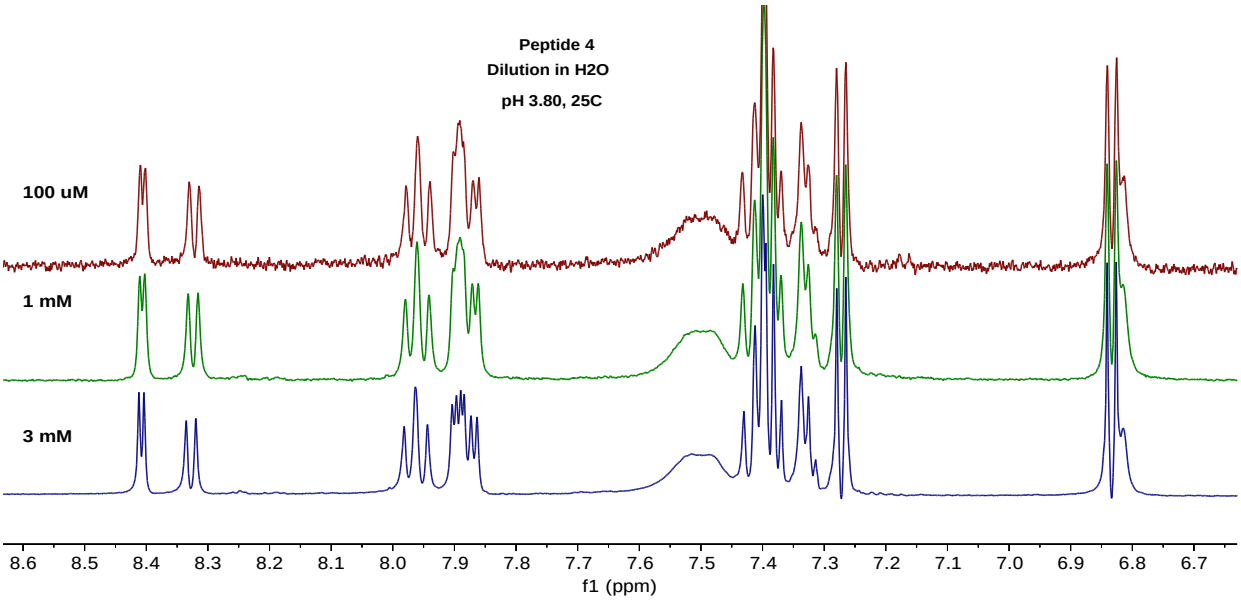

Figure S9: Comparison of the W5es water-suppressed amide region of peptide **4** in water (9:1 H_2O D_2O, 100 mM acetate, pH 3.8, ref. DSS) at different peptide concentrations.

Hydrogen-Deuterium Exchange (HDX)

Known quantities of lyophilized peptide TFA salt were dissolved in 450 µL D_2O, 100 mM d_3-acetate, measured pH 3.4 (with trace DSS) to 1 mM peptide to initiate the hydrogen-deuterium exchange reaction. Samples were immediately transferred to an economy NMR, capped, and inserted into the NMR spectrometer at 20°C. An in-house developed pulse program for monitoring kinetics (kin1d) was used to acquire 1D ^{1}H-NMR periodically, generally every 30 sec at early timepoints, increasing to 5 min between experiments at later timepoints. Time from dissolution in D_2O to first acquisition was about 3 minutes. Relevant pulse program parameters: ns=4 to 8; d1=1.5 sec; 90°pw. For short model peptides, amide resonance assignments were made by spiking the HDX solution with H_2O and acquiring 1D-TOCSY spectra.

NMR spectral data were processed using Mestrenova. FIDs were FT'd and an initial automatic phase correction was applied. Individual spectra were phased manually to ensure consistency. Bernstein polynomial fit was used as the baseline correction algorithm. Amide hydrogen peaks were integrated with the Data Analysis tools in Mestrenova, which were also used to fit exponential decay curves to extract HDX rate constants. For some resonances, only one peak of a doublet was well-resolved; in these cases, the half-doublet integral was used to track HDX. Integrating in this way for well-resolved doublets resulted in essentially identical HDX rates.

VT-NMR

Samples for VT-NMR studies were prepared by dissolving known quantities of lyophilized peptide TFA salt in 450 µL 9:1 H_2O:D_2O, 100 mM d_3-acetate, pH 3.8 (with trace DSS) to 1 mM peptide concentration. Samples were transferred to economy NMR tubes, capped, and wrapped in parafilm.

VT-NMR data were acquired on a Bruker Avance III 500 MHz NMR spectrometer equipped with a 5 mm BBFO probe or 5 mm Prodigy CryoProbe. NMR temperature was calibrated with

4% CH_3OH in CD_3OD for 5°C→20°C and neat ethylene glycol for 25°C and above. W5es solvent suppression was used to suppress the water signal. At least 5 minutes of equilibration time was allowed between temperature steps.

B. 2D-NMR Experimental Procedures

Samples were prepared by dissolving known quantities of lyophilized peptide in the NMR solvent. The solutions were transferred to Wilmad P-535-PP-7 NMR tubes, capped, and sealed with Parafilm. Solutions were stored at −10°C in a freezer for 24 hr to monitor for precipitation tendencies which were not observed (after thawing for aqueous solutions).

2D-NMR data were collected on either a Bruker Avance III 500 MHz or Bruker Avance III HD 600 MHz spectrometer running TopSpin 3.2. Methanol experiments were performed at room temperature, while aqueous experiments were normally performed at 5°C to distance the water resonance from peaks of interest, to improve chemical shift dispersion in the amide region, and (presumably) to increase the foldamer helical content. Peptide **4** in water was analyzed at 10°C due to slightly more severe resonance overlap of the amides at 5°C (although the increased temperature seems to not have decreased the secondary content significantly, as long-distance NOEs this peptide at 30°C are still more intense than those for other peptides at 5°C).

Data were processed with TopSpin 3.2, generally using Bruker default processing parameters. Chemical shifts were referenced to 0 ppm for DSS; DQF-COSY data were referenced using arbitrarily chosen resonances of the referenced TOCSY spectrum. Baseline correction was occasionally done with BC_MOD=qfil to further suppress the water signal. For the water spectra, baseline correction in F2 was done with the abs2.water command. Spectra were analyzed using the NMRFAM distribution of SPARKY[S3] on data converted to .ucsf format with the bruk2ucsf utility.

Solvent suppression of 1D ^{1}H-NMR spectra was found to be optimal with W5es solvent suppression. Delay for binomial solvent suppression (D19) was optimized to balance intensity reduction of peaks near solvent with solvent suppression and DSS intensity (which tended to be reduced to undetectable levels at D19 > 170 μs). Pre-saturation was found to provide adequate solvent suppression in the COSY spectra without significant amide signal deterioration. Double quantum-filtered (DQF) COSY was used in some experiments for *J*-coupling measurement and reduced noise near the diagonal. W5es solvent suppression was found to be excellent for solvent suppression in the TOCSY spectra. 3-9-19 WATERGATE solvent suppression was used in all ROESY spectra.

Pulsewidth calibration was performed with the Bruker pulsecal program for all 2D-NMR data acquired. Sweep widths and O1 were optimized based on 1D ^{1}H-NMR spectra. Receiver gain was determined with rga for TOCSY and ROESY spectra and with the default automation program for COSY spectra.

Table S1. Selected parameters in 2D-NMR experiments in CD_3OH.

Name	1	2	3	4
^{1}H-NMR Frequency	500 MHz	500 MHz	600 MHz	600 MHz
Spectrometer	Bruker Avance III-500	Bruker Avance III-500	Bruker Avance III-HD 600	Bruker Avance III-HD 600
Probe	5 mm DCH	5 mm DCH	5 mm CPTCI	5 mm CPTCI
Solvent	CD_3OH	CD_3OH	CD_3OH	CD_3OH
Concentration	3 mM	3 mM	3 mM	3 mM
Temperature	24°C	24°C	24°C	24°C
COSY pulseprog	cosygpprqf	cosygpprqf	cosydfphpr	cosydfgpph19
NS	4	4	8	8
DS	32	32	64	32
TD(f2)	2048	2048	4096	4096
TD(f1)	256	256	256	256
TOCSY pulseprog	mlevgpphw5es	mlevgpphw5es	mlevgpphw5es	mlevgpphw5es
NS	8	8	8	8
DS	64	64	32	32
D9	80 ms	80 ms	80 ms	80 ms
Spinlock frequency	9.62 kHz	9.62 kHz	9.62 kHz	9.62 kHz
TD(f2)	4096	4096	4096	4096
TD(f1)	256	256	256	256
ROESY pulseprog	roesygpph19.2	roesygpph19.2	roesygpph19.2	roesygpph19.2
NS	32	32	32	40
DS	64	64	32	32
D1	3 sec	3 sec	3 sec	3 sec
D19	200 μs	200 μs	150 μs	150 μs
O1p	4.910 ppm	4.910 ppm	4.910 ppm	4.910 ppm
P15	200 ms	200 ms	200 ms	200 ms
Spinlock frequency	5.95 kHz	5.95 kHz	5.95 kHz	5.95 kHz
TD(f2)	2048	2048	2048	2048
TD(f1)	256	256	256	256

Table S2. Selected parameters in 2D-NMR experiments in H_2O.

Name	1	2	3	$\mathbf{4}_{10°C}$	$\mathbf{4}_{30°C}$
^{1}H-NMR Frequency	600 MHz	600 MHz	600 MHz	600 MHz	600 MHz
Spectrometer	Bruker Avance III-HD 600	Bruker Avance III-HD 600	Bruker Avance III-HD 600	Bruker Avance III-HD 600	Bruker Avance III-HD 600
Probe	5 mm CPTCI	5 mm CPTCI	5 mm CPTCI	5 mm CPTCI	5 mm CPTCI
Solvent	9:1 H_2O:D_2O, 100 mM d_3-acetate buffer, pH 3.8, trace DSS	9:1 H_2O:D_2O, 100 mM d_3-acetate buffer, pH 3.8, trace DSS	9:1 H_2O:D_2O, 100 mM d_3-acetate buffer, pH 3.8, trace DSS	9:1 H_2O:D_2O, 100 mM d_3-acetate buffer, pH 3.8, trace DSS	9:1 H_2O:D_2O, 100 mM d_3-acetate buffer, pH 3.8, trace DSS
Concentration	3 mM	3 mM	3 mM	3 mM	3 mM
Temperature	5°C	5°C	5°C	10°C	30°C
COSY pulseprog	cosydfphpr	cosydfphpr	cosydfphpr	cosydfphpr	cosydfphpr
NS	16	8	8	8	8
DS	64	64	64	64	64
TD(f2)	4096	4096	4096	4096	4096
TD(f1)	256	256	256	256	256
TOCSY pulseprog	mlevgpphw5es	mlevgpphw5es	mlevgpphw5es	mlevgpphw5es	mlevgpphw5es
NS	16	8	8	8	4
DS	32	32	32	32	32
D9	80 ms	80 ms	80 ms	80 ms	80 ms
Spinlock frequency	9.62 kHz	9.62 kHz	9.62 kHz	9.62 kHz	9.62 kHz
TD(f2)	4096	4096	4096	4096	4096
TD(f1)	256	256	256	256	256
ROESY pulseprog	roesygpph19.2	roesygpph19.2	roesygpph19.2	roesygpph19.2	roesygpph19.2
NS	48	40	40	48	32
DS	32	32	32	32	32
D1	3 sec	3 sec	3 sec	3 sec	3 sec
D19	150 µs	150 µs	150 µs	160 µs	160 µs
O1p	4.700 ppm	4.700 ppm	4.700 ppm	4.700 ppm	4.700 ppm
P15	200 ms	200 ms	200 ms	200 ms	200 ms
Spinlock frequency	5.95 kHz	5.95 kHz	5.95 kHz	5.95 kHz	5.95 kHz
TD(f2)	2048	2048	2048	2048	2048
TD(f1)	256	256	256	256	256

C. 2D-NMR Data Interpretation

NOE distance calculation

Resonance assignment was accomplished partially using sequential assignment procedures.[S4] Integrated ROESY crosspeak volumes were converted into distances r_{ij} (assuming the initial rate approximation) by r^{-6} averaging.[S5] Comparison was made with an integrated known reference distance r_{ref} using **Equation 1**:

$$r_{ij} = r_{ref}\left(\frac{I_{ref}}{I_{ij}}\right)^{1/6} \quad \textbf{(1)}$$

Where I_{ij} represents the multiplicity-corrected volume integral of the crosspeak involving nuclei *i* and *j*. For crosspeaks involving only two protons, I_{ij} is simply equal to the measured crosspeak integral I_{meas}. For crosspeaks involving groups with multiple equivalent or stereo-unassigned protons, the measured integral is corrected using **Equation 2:**

$$I_{ij} = \frac{I_{meas}}{n_i \times n_j} \quad \textbf{(2)}$$

Where n_i is the number of nuclei *i* and n_j is the number of nuclei *j*.

ROESY offset correction

ROESY crosspeak volume integrals were not corrected for resonance offset effects; however, the difference in calculated distance would be negligible. ROESY crosspeak intensities attenuate as a function of distance of the center of the spectrum (O1 or O1p on Bruker instruments) due to NOE transfer during the spinlock of $x'-y'$ magnetization.[S5] However, the impact on calculated distance would be negligible. The maximum volume attenuation is calculated to be about 10%, based on the following equations:

$$B_1 = \frac{2\pi\omega_1}{\gamma} \quad \textbf{(3)}$$

$$\theta_{i,j} = \arctan\left[\frac{\gamma B_1}{2\pi(\nu_{i,j} - \nu_0)}\right] \quad \textbf{(4)}$$

$$I_{corr} = I_{meas}\left(\frac{1}{\sin^2\theta_i \sin^2\theta_j}\right) = I_{ij} \times k_{corr} \quad \textbf{(5)}$$

Where B_1 is the spinlock magnetic field strength in T, ω_1 is the spinlock frequency in Hz, γ is the magnetogyric ratio of ^{1}H (26.7×10^7 rad^{-1} T^{-1} s^{-1}), $\theta_{i,j}$ is the angle of the precession vector of nucleus *i* or *j* relative to the spinlock axis, $\nu_{i,j}$ is the precession frequency of nucleus *i* or *j* in Hz, ν_0 is the center of the spectrum in Hz (O1), I_{corr} is the resonance offset-corrected ROESY crosspeak volume, I_{meas} is the integrated ROESY crosspeak volume, and k_{corr} is the resonance offset correction factor. ROESY spectra were acquired on a 600 MHz spectrometer, and spinlock frequency was 5.95 kHz.

As an example, we can examine the effect of ROESY resonance offset correction on the integrated crosspeak **II**-2(Hγ)···**II**-4(HN) (we can simply refer to it as distance **a**) observed in its aqueous spectrum and see how it translates to the calculated internuclear distance, which according to **Equations 1** and **2** is 2.94 Å prior to correction. First, we need to correct the internuclear distance calibrant, which is Tyr5(Hδ)···(Hε) in this case. The correction for their resonance offsets is a factor of 1.12. Applying this correction changes the calculated distance **a** to 3.00 Å. Next, we of course need to correct the measured integral of crosspeak **a**. Using the

measured chemical shifts of the two resonances, we find a correction factor $k_{corr,\mathbf{a}}$ of 1.12. The calculated distance is now 2.94 Å. The distance is no different from the original distance in cases where the average off-resonance chemical shift difference of the nuclei within a particular crosspeak is similar to the average off-resonance chemical shift difference of the distance calibrant resonances.

What if the resonance offset of a pair of nuclei contributing to a ROESY crosspeak is more different from that of the distance calibrants? Crosspeak **II**-2(Hγ)···**II**-4(Hα) (distance **b**; 2.76 Å before correction) is the nearest to this description among the long-range ROESY crosspeaks described here. Plugging in the chemical shifts of these resonances results in a correction factor $k_{corr,\mathbf{b}}$ of 1.08. Applying this to the integrated crosspeak changes the calculated distance to 2.72 Å, a difference of 0.04 Å from the original calculated distance.

Correcting for ROESY resonance offset effects for all crosspeaks in the reported spectra has very little impact on the calculated distances and no impact on the overall structural conclusions drawn from the data.

Selection of reference distances

The reference distance for all spectra was chosen to be the Tyr5(Hδ-Hε) crosspeak at 2.80 Å due to the excellent chemical shift dispersion about their crosspeaks and their unchanging internuclear distances. We found that referencing to this internuclear distance tended to overestimate internuclear distances to a consistent degree across all spectra by comparing it to other fixed distances in the peptides (**Table S3**). This is likely a result of significant TOCSY or zero-quantum transfer artifacts observed for the Tyr5(Hδ-Hε) crosspeaks leading to consistent integral overestimation by the Sparky integration algorithm.[S5] In many cases, the crosspeaks of the other fixed distances featured overlapping too severe for their reliable use as a reference distance, and generally, the degree of overlap for these crosspeaks varied among the eight ROESY spectra due to variations in chemical shifts among the peptides and between the solvents. Since the integral overestimation of Tyr5(Hδ-Hε) is consistent among all ROESY spectra, its use as a reference distance was deemed optimal. Due to the consistent distance overestimation from the utilized reference distance, we used the calculated internuclear distances directly as upper-bound distance restraints in our calculations rather than adding to the upper bound.

Discussion of 2D-NMR data interpretation of peptide secondary structure

It should be noted that calculation of distances from ROESY crosspeak volumes is, strictly speaking, only correct for conformational equilibria dominated by a single conformational cluster with negligible contribution to the spectroscopic signals from low-population clusters within the ensemble.[S6] However, conformational heterogeneity is the norm for short peptides.[S7] Cooperatively-folded α-helical peptides tend to feature frayed ends.[S8] In contrast, polypeptides with non-α residues tend to not be cooperatively folded and thus the center of the helix is likely less stabilized compared to their α-peptide helix counterparts.[S9] For all peptide foldamer types, particularly short ones, the possibility that some quantity of frayed conformers (at any position along the sequence) contributes to the spectroscopic signal cannot be excluded.

Since significant fluctuation of internuclear distances between non-sequential ^{1}H nuclei on the ROESY timescale is likely within peptide foldamers, calculation of "distance" gives the mistaken impression of a fixed or time-averaged distance giving rise to a precise description of

the conformational behavior of a peptide in solution. However, for the former interpretation, fixed internuclear distances over the timescale of the ROESY mixing time (200 ms here) are likely fluxional. For the latter, ROESY intensities are proportional to distances at their inverse sixth-power, so the calculated distances are not a simple linear time average. A fixed unit such as distance thus is unable to provide a useful description of the *entire* structural ensemble of the peptide, either as a fixed structure (it is not) or as a time-averaged ensemble (very close internuclear distances in low-population conformational clusters can result in detectable NOE crosspeaks and bias the "average" structure determined from the data). Peptide structure is perhaps best represented as a movie rather than an image or superposition of images, but NOESY or ROESY experimental data do not provide the information on how to spread the structural images over time to create a movie which realistically depicts a peptide's conformational properties.[S10] Indeed, it has been argued that, for conformationally promiscuous molecules, "the 'average' derived from spectroscopic data represents a virtual structure devoid of physical meaning".[S11] Molecular dynamics simulations can partially address the time-resolution problem, but different force fields can result in ensembles with drastically different properties.[S12] Interpreting the theoretical data with experimental data on hand is essential, then, to draw confident conclusions about the structural properties of peptides or peptide foldamers in solution. Molecular dynamics studies of α/γ-peptides are ongoing in our laboratory.

In summary, since conformational heterogeneity of short linear peptides in solution must in general be assumed, the NOE-calculated distances reported should not be interpreted as fixed or time-averaged distances, and their use as restraints here have been made cautiously. Intra-residue NOEs were excluded in structural calculations (*vide infra*).

Table S3. Calculated fixed internuclear distances w/ Tyr5(H_δ–H_ε) 2.80 Å reference distance.

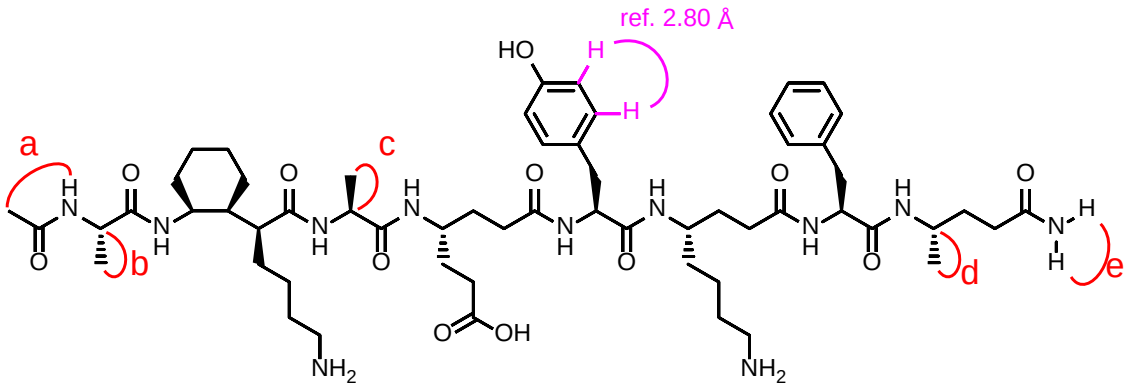

Peptide	Spectrum	a	b	c	d	e
1	CD_3OH	3.47	3.31	3.45	3.20	2.07
1	H_2O	3.62	(overlap)	(overlap)	3.33	1.97
2	CD_3OH	3.54	3.26	3.23	3.36	2.24
2	H_2O	3.42	3.19	3.04	3.20	2.68
3	CD_3OH	3.34	3.16	3.06	3.09	2.09
3	H_2O	(overlap)	3.15	3.14	3.17	2.63
4	CD_3OH	3.37	3.21	2.90	3.26	2.06
4	H_2O	3.34	3.15	3.13	3.10	2.85
	Average	3.44	3.20	3.14	3.21	2.32
	Actual	2.90	2.40	2.40	2.40	1.80
	Difference	0.54	0.80	0.74	0.81	0.52

D. Other ^{1}H-NMR Observables

As mentioned above, there are limits in the ability of NOE crosspeaks to provide complete detail into the conformational behavior of short peptides in solution. In combination with other NMR observables, a clearer picture on the qualitative aspects of its conformational ensemble emerges.[S6] Four observables will be focused on here, all of which were measured in aqueous solvent: ^3J-coupling (focusing on HN–H_α coupling within α-residues), temperature coefficients (the sensitivity of amide HN to chemical shift perturbation with changes in temperature), chemical shift deviation (CSD; here, the difference in chemical shift of H_α nuclei relative to random coil) and hydrogen-deuterium exchange (HDX; rate of exchange of amide hydrogens with solvent deuteriums). Individually, all but CSD contribute to supporting the conclusions drawn from 2D-NMR data of cyclic γ-residues stabilizing helical secondary structure. Collectively, the three measurements correlate well with one another, further strengthening the NOE-based conclusions.

$^3J_{HN-H\alpha}$ Coupling

The use of ^3J-coupling in the conformational analysis of organic molecules has a long history, a specific example being the use of $^3J_{HN-H\alpha}$ coupling to characterize secondary structure of peptides and proteins.[S13] The $^3J_{HN-H\alpha}$ coupling constant is sensitive to the ϕ torsion separating the two nuclei according to a Karplus correlation, parametrized for α-peptides by Bax and coworkers[S14] (among others). In general, α-helical residues typically show small coupling constants (≈4 Hz), random coil residues show medium coupling constants (≈7 Hz), and β-strand residues show large coupling constants (≈9 Hz). However, because coupling constants are degenerate with respect to the Karplus torsion, and because the relationship between the observed coupling constant and the torsion populations is non-linear, the observed coupling constant may not correspond to a highly populated torsion but instead the result of several conformational populations averaging to generate a "virtual" coupling constant. In short, its use in conformational analysis can be convoluted by conformational heterogeneity. This problem can be overcome in molecular dynamics by applying a time-averaged J-coupling potential energy term,[S15] but conventional NMR structure calculation packages utilize instantaneous J-coupling restraints. It can be seen in the case of the present α/γ-peptides that the J-couplings authentically report on the evolution of secondary structure as cyclic γ-amino acids are introduced.

Table S4. Values of $^3J_{HN-H\alpha}$ (α-residues) and $^3J_{HN-H\gamma}$ (γ-residues) in **1**-**4** (Hz).

Residue	1	2	3	4
Ala1	5.7	5.3	4.9	5.0
γ2	9.3	**10.4**	**10.8**	**10.7**
Ala3	5.2	3.9	3.5	4.4
γ4	9.5	9.4	**10.7**	**10.6**
Tyr5	6.1	6.2	5.1	4.1
γ6	10.0	9.8	10.2	**10.8**
Phe7	6.6	7.2	6.3	5.4
γAla8	9.5	9.8	9.4	9.6

Table S4 lists and **Figure S10** shows the distribution of coupling constants among the α-amino acid residues in peptides **1**-**4** measured in H_2O. Overall, the coupling constants become smaller as cyclic γ-residues are introduced. Peptide **1** with no cyclic γ-residues features no α-amino acid coupling constant smaller than 5 Hz, whereas peptide **4** with three cyclic γ-residues features only one >5 Hz coupling constant. Notably, the all-acyclic peptide **1** features coupling constants that are still smaller than typical random coil values,[S16] which might lead one to the conclusion that helix formation remains favored, even with no cyclic γ-residues. However, "random coil" is now well known to be a misnomer,[S17] and it is likely that the disordered state of an α-residue is dependent on the identity of its sequence neighbors (α- or γ-residue, etc.). Thus the precise physical meaning of the absolute values of the coupling constants of the α-residues in α/γ-peptides as it relates to their conformational properties remains uncertain, whereas the change in coupling constants with cyclic constraint content is fairly clear.

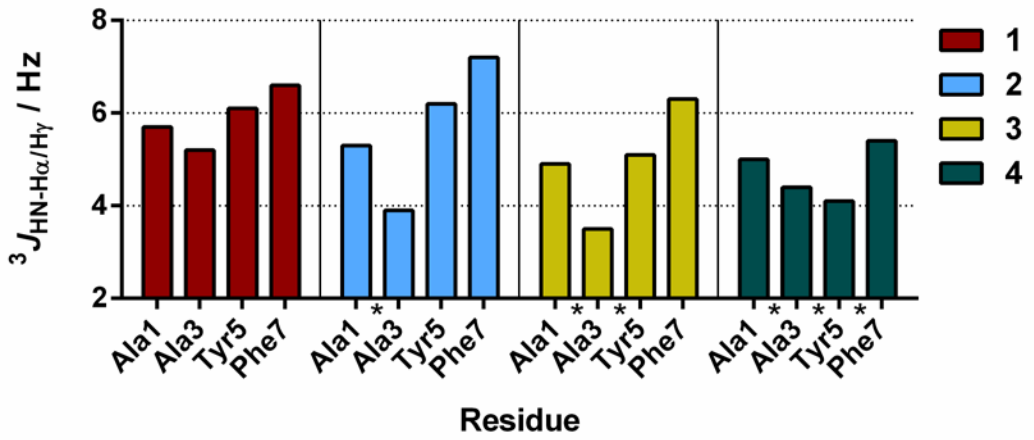

Figure S10. $^3J_{HN-H\alpha}$ coupling constants of α-residues within α/γ-peptides **1**-**4**. Asterisks indicate the positions of KACHA residues.

Chemical shift deviation

An additional empirical relation between an NMR observable and local polypeptide conformation developed within the protein NMR community is the chemical shift deviation[S18] (CSD; also called chemical shift index[S19] or, more generally, secondary chemical shifts[S20]). CSD is the empirical observation that the deviation in chemical shift values for a nuclei of a residue relative to that particular residue's random coil tends to reflect the local conformation of the residue. The most extensively utilized nucleus is the $^1H_\alpha$, but $^{13}C_\beta$ and backbone ^{15}N CSDs are also routinely used for protein NMR structure determination.[S21] Residues in α-helical local conformations tend to feature negative CSD for $^1H_\alpha$ (more upfield), whereas residues in β-sheet local conformations tend to feature more positive CSD for $^1H_\alpha$ (more downfield).

Application of this empirical observation to conformational analysis of foldamers containing α-residues is, as in the case of $^3J_{HN-H\alpha}$ analysis, complicated by the fact that the empirical trend may not hold true as the nature of the unfolded ensemble of each α-residue likely depends on the residue types within the foldamer. Nevertheless, collecting the data is simple, and comparing the CSD data between structured and unstructured foldamers (as judged by NOE crosspeaks, the "gold standard" in solution-phase conformational analysis of polypeptides with arbitrary backbone composition) may yield interesting trends that could prove useful if cautiously applied in conjunction with other observables with clearer physical meaning.

Table S5. Chemical shift deviation of H_α relative to random coil[a] of α-residues in **1**-**4** (ppm).

Residue	1	2	3	4
Ala1	-0.17	-0.07	-0.11	-0.09
Ala3	-0.17	-0.28	-0.19	-0.18
Tyr5	-0.13	-0.18	-0.30	-0.19
Phe7	-0.20	-0.23	-0.22	-0.30

[a]From Wishart *et al.*[S22]

Figure S11 shows the trend of CSD of the α-residues within peptides **1**-**4** in water, also listed in **Table S5**. Since ROESY analysis indicates that **1** is largely unstructured in solution, we interpret

this peptide as adopting the α/γ-peptide "random coil" state. The reference chemical shifts for each α-residue are taken as the random coil chemical shifts determined by Wishart and coworkers.[S22]

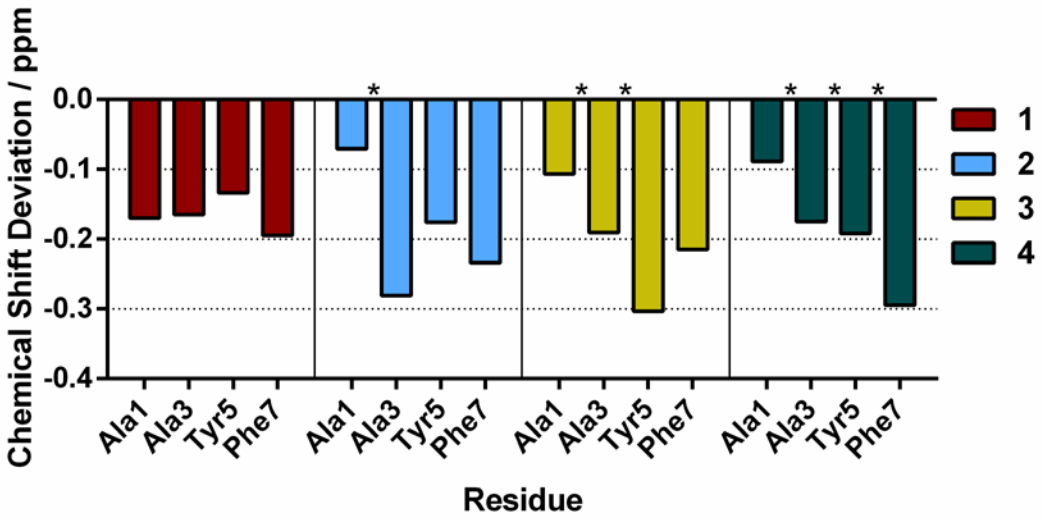

Figure S11. Chemical shift deviation relative to random coil (from Wishart *et al*.[S22]) of H_α of α-residues in **1**-**4**. Asterisks indicate the positions of KACHA residues.

All α-residues, even the "α/γ-peptide random coil" α-residues of **1**, show significantly negative CSD relative to the α-peptide random coil. The unstructured state of α/γ-peptides may bias the α-residue torsions toward the α-helical region of the Ramachandran plot relative to the α-peptide random coil. There is not a uniform trend of upfield chemical shift with increased structuring of the foldamers. Since ROESY, despite its flaws (*vide supra*), provides more direct information on the secondary structure of foldamers, CSD does not appear to be a useful general tool for conformational analysis for α/γ-peptides. Interestingly, the large negative CSD is felt only at a single α-residue within **2**-**4**: the α-residue immediately following the C-terminal KACHA residue of the sequence. This may hint at particular conformational features of this α-residue. Perhaps the capping α-residue adopts a more positive value of ϕ than the α-residues within the α/KACHA segment, according to the functions correlating ϕ with $\Delta\delta$.[S23] In the absence of clearer experimental data, this remains speculation.

VT-NMR

Amide temperature coefficients—the change in amide chemical shift with change in temperature, reported as $\Delta\delta/\Delta T$ (ppb/°C)—have been often used as qualitative indicators of protein[S24] and peptide[S25] secondary structure. The simplest interpretation of the data bins the temperature coefficients into two classes: amide NHs with temperature coefficients more negative than −4 ppb/°C are classed as "exposed", and amide NHs with temperature coefficients more positive than −4 ppb/°C are classed as "sequestered. However, use of temperature coefficients in this way has been shown to have "zero predictive validity" on top of being misguided as to the physical processes underlying the chemical shift change.[S26] This interpretation of the data relies on the assumption of a single rigid conformation unchanging in dynamics across the temperature range, resulting in zero change in average distance from sequestered amide hydrogens to their

intramolecular H-bond acceptor and essentially zero change in chemical shift, which depends on the inverse third power of H-bond donor-acceptor internuclear distance.[S27] The solvent-exposed amide hydrogens, in contrast, experience an increased average distance to their H-bond acceptors with increasing temperature as the magnitude of thermal fluctuations increases, resulting in upfield chemical shift change.[S27] This interpretation was called into question by multiple authors.[S24, 26, 28] In reality, especially for partially folded peptides, increasing temperature tends to denature the folded state, the increased magnitude of thermal fluctuations also shifts upfield amide hydrogens engaged in intramolecular hydrogen bonds. Because these intramolecularly H-bonded amides are already shifted downfield due to their H-bond, as the secondary structure is disrupted, the magnitude of upfield chemical shift change is increased.[S26] Indeed, there is a linear relationship between chemical shift and $\Delta\delta$, indicating that strong hydrogen bond engagement can often be the *cause* of a temperature coefficient binned into the "exposed" class. For these reasons, temperature coefficients without other supportive data can lead to spurious conclusions.

Table S6. Temperature coefficients of amide resonances in **1**-**4** (ppb/°C).

Residue	1	2	3	4
Ala1	-8.2	-6.2	-5.7	-5.9
γ2	-7.4	**-6.7**	**-6.2**	**-6.2**
Ala3	-7.1	-6.4	-5.8	-5.8
γ4	-6.6	-3.8	**-5.1**	**-5.4**
Tyr5	-8.1	-9.1	-4.0	-4.7
γ6	-7.8	-7.8	-2.3	**-2.9**
Phe7	-8.9	-8.5	-8.0	-5.7
γAla8	-6.7	-6.5	-6.4	-5.4

It is with these cautions in mind that we first examine the temperature coefficient data on its own for **1**-**4** (**Figure S12** and **Table S6**). The general trend is toward more positive temperature coefficient with increasing cyclic γ-residue content, consistent with a greater proportion of secondary structure content as residue preorganization increases. Furthermore, "sequestered" amides within partially folded peptides **2**-**4** are exclusively within the segments of the foldamers known to be helical by ROESY analysis. The combined observations support one another and make us more certain in our original 2D-NMR structural analysis.

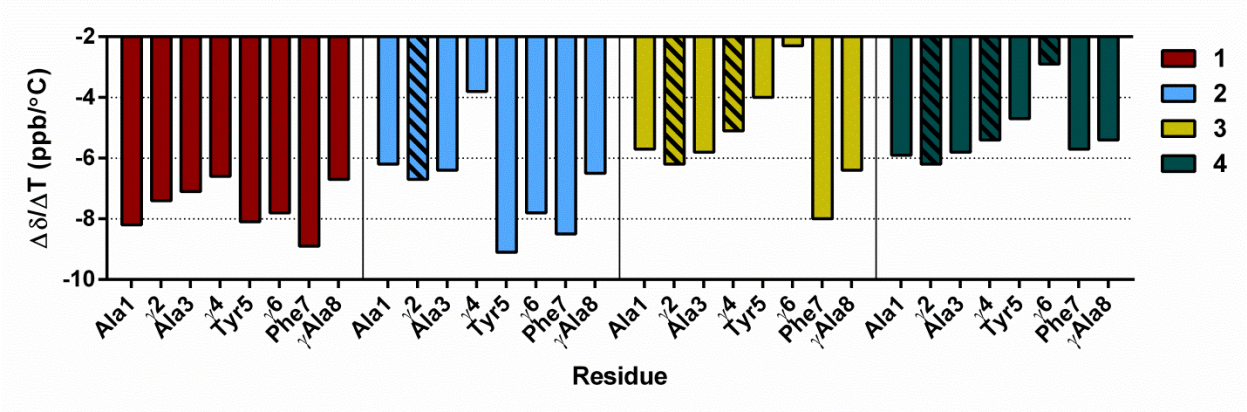

Figure S12. Temperature coefficients of amide resonances in α/γ-peptides **1**-**4**. Diagonal stripes indicate KACHA residues.

Comparisons of temperature coefficients with other NMR observables are discussed below.

Hydrogen-deuterium exchange

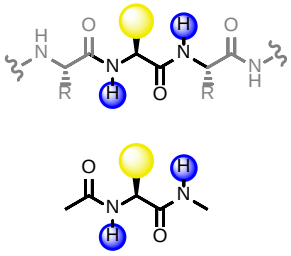

Figure S13. Amide resonances impacted by primary structure effects (blue) by sidechain identity of an α-amino acid (yellow).

Finally, hydrogen-deuterium exchange[S29] (HDX) provides more direct information on the strength of the hydrogen bonds defining helical peptide structures, and thus (with ^{1}H-NMR as the detection method) atomic-level detail of the secondary structure engagement along the peptide sequence. The rate of exchange of amide hydrogen atoms of a polypeptide with solvent deuterium (or hydrogen, or tritium) is inversely correlated with that amide's exclusion from solvent. In the case of proteins, the exclusion is mostly from tertiary structure formation occluding amides in the protein interior from solvent interactions.[S30] For isolated peptide secondary structures, the exclusion is mostly due to involvement in intramolecular hydrogen bonding.[S31] However, the primary structure of the peptide sequence also has significant effects on the exchange rates of nearby amide hydrogens.[S32] Polar sidechains such as serine enhance the rate of base-catalyzed amide hydrogen exchange of neighboring amides.[S32a] Hydrophobic sidechains such as the isopropyl group of valine desolvate neighboring amides, reducing the rate of amide hydrogen exchange.[S32b] For these reasons, normalization of observed exchange rates of a structured polypeptide (k_{ex}) using the intrinsic exchange rates of its constituent residues in the absence of secondary structure (k_{ch}) to generate a protection factor (P) is necessary to probe secondary structure (**Equation 6**).[S33] Primary structure effects have been found to be highly local; α-amino acid sidechains perturb the HDX rates only of the amide of the sidechain-bearing residue and the next amide in the sequence (**Figure S13**). For α-amino acids within α-peptides, the most extensive set of measurements if k_{ch} have been made using short dipeptide derivatives Ac-X-NHCH$_3$, where X is one of the 20 proteinogenic amino acids.[S32b]

$$P = log\left(\frac{k_{ch}}{k_{ex}}\right) \qquad \textbf{(6)}$$

In order to understand how increased secondary structure content changes HDX rates of non-natural polypeptides, it is necessary to have an unfolded baseline HDX rate to normalize to. For the α/γ-peptides explored here, peptide **1** provides a useful unfolded baseline for most residues within **2-4** because it is known to be unstructured in water and replicates most residues' primary environments in **2-4**. However, as cyclic γ-residues are introduced, the primary context of the subsequent α-residue is altered; the hydrophobicity of the cyclic constraint likely shields the α-residue's amide from exchange. Peptide **1** also provides for no reference KACHA residue since it does not contain one. In order to determine intrinsic exchange rates for KACHA-adjacent α-residues and for KACHA itself, several short model peptides were synthesized. **HDX-1**, **HDX-2**, and **HDX-3** were synthesized to simulate the primary environment of Ala, Tyr, and Phe residues, respectively, following a KACHA residue (**Figure S14**). The design features of these model peptides include: 1) A 2-ethylbutyryl (2-EB) cap at the N-terminus of the α-residue, which we had previously found to be an effective method to approximate the steric bulk of a cyclic γ-amino acid;[S34] 2) An N-terminal α-residue, which bears the amide to be tested; 3) additional α-residues too distant for HDX perturbation but enhance solubility in water (Lys) and provide a spectroscopic handle for UV-vis concentration measurement (Tyr). The 2-EB cap is utilized instead of KACHA itself because, due to the non-cooperative behavior of unnatural polypeptide folding,[S9] the single KACHA residue would likely nucleate a hydrogen bond to the α-residue's amide, creating the secondary environment that must be abolished for a correct k_{ch} model. In order to compare the 2-EB cap HDX shielding abilities with those of KACHA, **HDX-4** and **HDX-5** with Tyr as their test α-residue were synthesized. A large difference in HDX rates of the Tyr amide hydrogen between these two model peptides would indicate close spatial proximity of the amide hydrogen and the N-terminal cap on the KACHA residue, demonstrating the presence of excessive residual secondary structure.

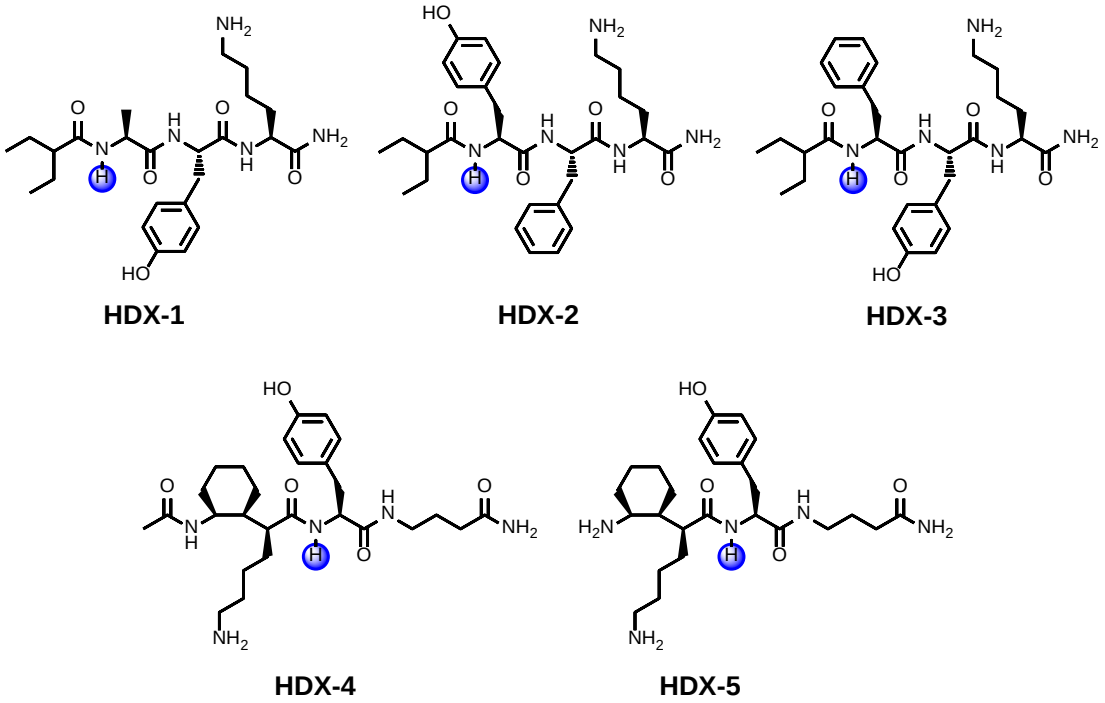

Figure S14. Structures of short model peptides **HDX-1** through **HDX-5** designed to approximate intrinsic HDX rate k_{ch} for α-amino acids following KACHA (blue).

HDX rate data for HDX model peptides is shown in **Figure S15**. Similar to the k_{ch} rates found in the Englander model dipeptides,[S32b] the bulky sidechains of Tyr and Phe in **HDX-2** and **HDX-3** slow hydrogen exchange relative to Ala in **HDX-1**. The exchange rate of 2-EB-containing **HDX-2**, 66 × 10^{-5} s^{-1}, is about three times that of KACHA-containing **HDX-4** (23 × 10^{-5} s^{-1}). This difference is either due to 2-EB insufficiently mimicking the hydrogen exchange shielding ability of the KACHA residue's steric bulk or due to residual secondary structure due to the preorganizing effect of KACHA in **HDX-4**. The results with **HDX-5** favor the latter interpretation. The exchange rate of the Tyr residue amide was too high to measure accurately (>500 × 10^{-5} s^{-1}). The free amine thus assists in deprotonating the amide, either directly or by attracting water molecules near to the amide. In either case, KACHA's N-terminus interacts with the Tyr amide hydrogen, and thus KACHA still provides secondary structure, making **HDX-4** and **HDX-5** poor models for KACHA primary structure.

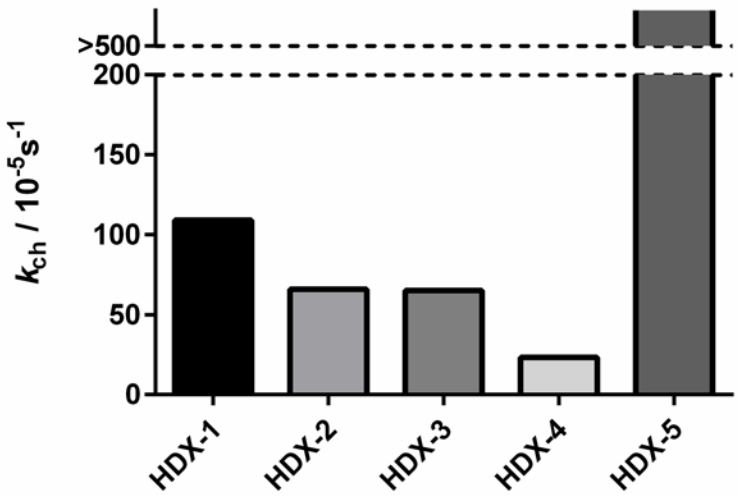

Figure S15. Hydrogen-deuterium exchange rates measured for **HDX-1** through **HDX-5**. The exchange of the amide hydrogen of **HDX-5** was too rapid to measure.

Table S7. Measured HDX rates for **1-4** ($10^{-5}s^{-1}$).

Residue	1	2	3	4
Ala1	n.d.	n.d.	n.d.	n.d.
γ2	41	**3.8**	**3.2**	**2.1**
Ala3	364	14	9.2	5.0
γ4	29	26	**1.8**	**2.3**
Tyr5	168	83	5.4	5.4
γ6	18	12	13	**1.5**
Phe7	183	132	50	9.6
γAla8	23	19	14	9.1

With appropriate k_{ch} values in hand—for α-residues next to acyclic γ-amino acids, as well as acyclic γ-amino acids, the exchange rates measured in **1**; for α-residues adjacent to KACHA, the exchange rates measured in **HDX-1**, **HDX-2**, and **HDX-3**; for KACHA itself, its exchange rate measured in **2**—we can calculate HDX protection factors for peptides **2**-**4**. Prior to this, it is useful to view how raw measured HDX rates vary among **1**-**4** (**Figure S16**). Most immediately apparent is the ≈20-fold to ≈5-fold decrease HDX rate at the α-residue immediately following the introduced cyclic γ-residues (diagonal stripes in **Figure S16**). At this point in the analysis, it is too early to conclude whether the HDX protection provided by KACHA is due to improved hydrogen bonding or greater steric shielding.

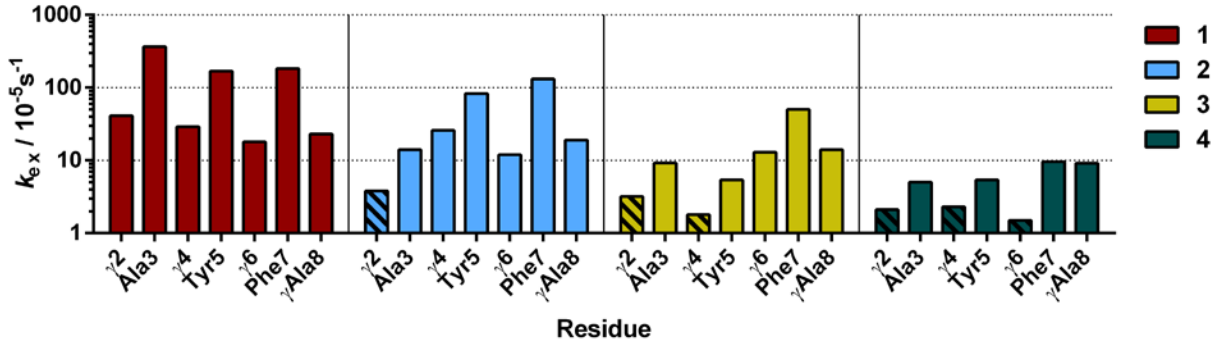

Figure S16. Hydrogen-deuterium exchange rates measured for α/γ-peptides **1**-**4**. Diagonal stripes indicate KACHA residues.

KACHA's HDX protecting effects do not, however, propagate as strongly through the sequence, although it does appear to have a stronger influence on sequence-distant α-residues than sequence-distant γ-residues (most easily seen in **Table S7**). The HDX rates of the α-residues *i*+3 relative to an introduced KACHA decrease by about a factor of two: the HDX rate of Tyr5 in **2** ($83 \times 10^{-5}s^{-1}$) is about half that of Tyr5 in **1** ($168 \times 10^{-5}s^{-1}$), and the HDX rate of Phe7 in **3** ($50 \times 10^{-5}s^{-1}$) is about half that of Phe7 in **2** ($132 \times 10^{-5}s^{-1}$). Importantly, these α-residues donate their amide hydrogen to the KACHA carbonyl H-bond acceptor in the γ→α H-bond in the 12-helix. In contrast, the γ-residues *i*+2 relative to the introduced KACHA are hardly impacted in their amide HDX rates. These γ-residues, in the 12-helix state, donate their amide hydrogen to the α-residue immediately preceding the introduced KACHA to form the α→γ H-bond. This is somewhat unexpected; the expected trend would be more strongly impacted α→γ H-bond, since this H-bonded pseudocycle contains the cyclic constraint (**Figure S17**). However, the structuring effect (as measured by non-normalized HDX rates) would support a strengthening γ→α H-bond that does *not* include the cyclic constraint. However, since the unstructured α-residues' amide hydrogens exchange more rapidly than those of the γ-residues, the greater change in HDX rate may reflect instead a greater HDX sensitivity to structural changes rather than a greater magnitude of structural change.

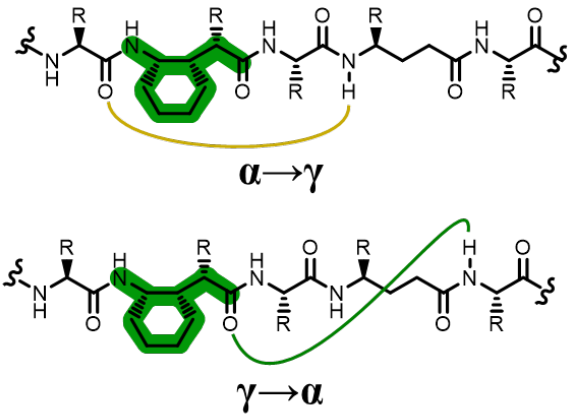

Figure S17. Depiction of the two types of hydrogen bonds within α/γ-peptide 12-helices: α→γ (above) and γ→α (below). Cyclic γ-amino acid constraint is highlighted in green.

The conception of KACHA's impacts on H-bonding strength discussed with the non-normalized HDX rates in mind do not alter much after normalization with the HDX models (**Figure S18** and **Table S8**). The largest increases to protection factor with introduction of KACHA occur at the same positions along the sequence as reduction in HDX rate: α-residues *i*+1 and *i*+3 relative to KACHA are more protected, whereas γ-residues within the sequence are not affected significantly.

Table S8. HDX protection factors calculated for **2**-**4**.[a]

Residue	1	2	3	4
Ala1	–[b]	n.d.[c]	n.d.	n.d.
γ2	–	**0**[b]	**0.07**	**0.25**
Ala3	–	0.88	1.07	1.34
γ4	–	0.06	**0.32**	**0.22**
Tyr5	–	0.31	1.09	1.09
γ6	–	0.16	0.14	**0.41**
Phe7	–	0.14	0.56	0.83
γAla8	–	0.09	0.24	0.41

[a]Relative to residues in 1 for α- and acyclic γ-residues.
[b]Used as k_{ch} references.
[c]Not determined (exchange too rapid to measure).

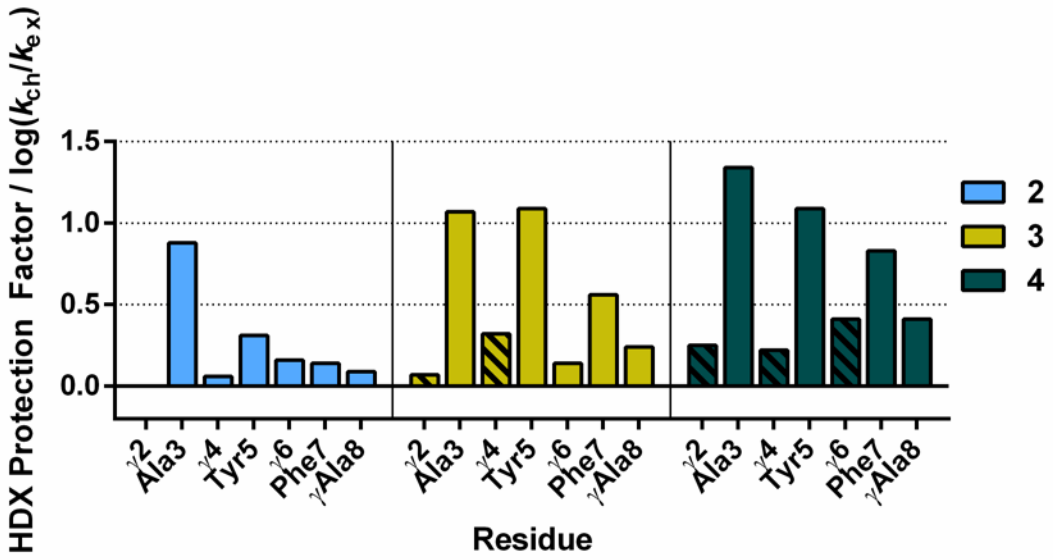

Figure S18. HDX protection factors calculated for **2-4** according to **Equation 3**. HDX rates measured in **1** were used as intrinsic HDX rates (k_{ch}) for α-residues not following KACHA and γ^4 residues in **2-4**. HDX rates for **HDX-1**, **HDX-2**, and **HDX-3** were used as k_{ch} for α-residues following KACHA. HDX rate of KACHA within **2** was used as k_{ch} for KACHA in **3-4**. Diagonal stripes indicate KACHA.

Correlations between ^{1}H-NMR observables

Ultimately, as discussed at various points above, the clearest picture of peptide secondary structure can only emerge from a combination of multiple types of experiments which interrogate different physical features of folded structures. Good correlations between the measurement types can give us high confidence that the overall structural conclusions are sound. The focus here is on $^3J_{HN-H\alpha}$, temperature coefficients, and HDX, since H_α chemical shift deviations did not yield clear trends. Only observables for the α-residues are considered here, since the empirical basis for interpreting γ-residue data with these measurements is shakier.

Figure S19 depicts the correlation between the $^3J_{HN-H\alpha}$ coupling constants of the α-residues within **1-4** and the temperature coefficients of their amide hydrogens. A linear correlation with a negative slope exists between these two measurements; residues with more positive temperature coefficients tended to also have smaller $^3J_{HN-H\alpha}$ coupling constants. The α-residues within α/γ-peptide 12-helices adopt α-helix like torsion angles, which feature ϕ values giving rise to smaller coupling constants relative to the random coil.[S35] The α-residues in peptides **1-4** which most strongly feature spectroscopic signatures of 12-helicity are those nearest the cyclic γ-residues. In fact, the upper-left portion of the curve is occupied exclusively by these helical α-residues. These two measurements in concert thus support the structural conclusions drawn from the 2D-NMR spectral data.

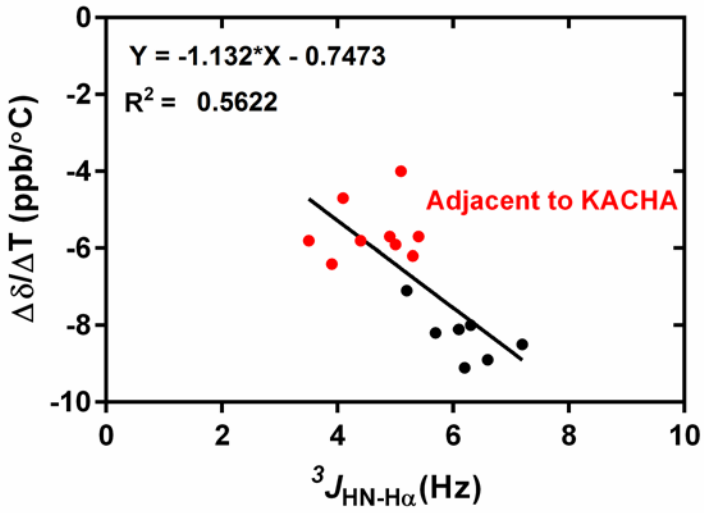

Figure S19. Correlation between $^{3}J_{HN-H\alpha}$ and temperature coefficients ($\Delta\delta/\Delta T$) for α-residues within **1-4**. α-Residues immediately following KACHA, which are expected to be most engaged in H-bonding based on HDX analysis, are shown in red.

Figure S20 represents the correlation between the measured $^{3}J_{HN-H\alpha}$ coupling constants and the HDX protection factors. Again, a linear correlation with a negative slope is apparent, with the 12-helical α-residues being the sole occupants of upper-left half of the data set. Smaller $^{3}J_{HN-H\alpha}$ occurs in combination with larger HDX protection factors—precisely the expected trend if both measurements report on local secondary structure stability. The trend is particularly important in our assignment of confidence to using $^{3}J_{HN-H\alpha}$ coupling constants as secondary structural reporters for α/γ-peptides, since HDX rate has a physical meaning more directly related to secondary structure engagement of the amides.

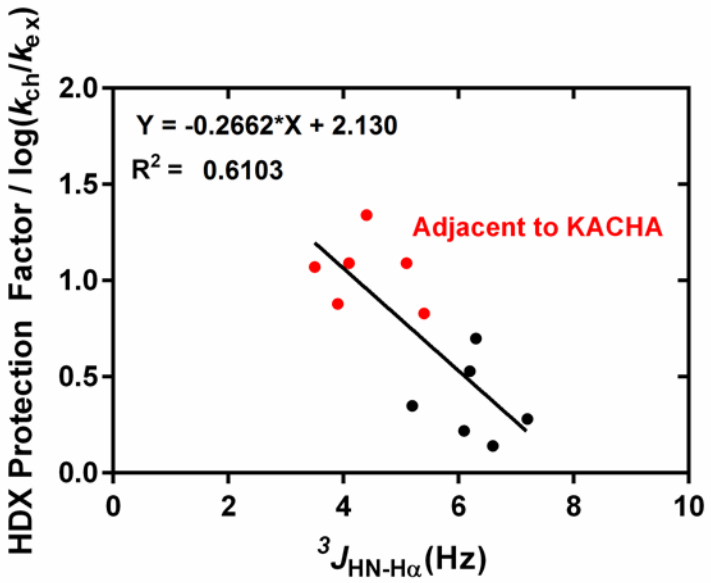

Figure S20. Correlation between $^3J_{HN-H\alpha}$ and HDX protection factors for α-residues in **1**-**4**. α-Residues immediately following KACHA, which are expected to be most engaged in H-bonding based on HDX analysis, are shown in red.

Figure S21 depicts the correlation between the temperature coefficients and the HDX protection factors of the α-residues. The correlation is linear with a positive slope, with all helical α-residues having the most positive temperature coefficients and HDX protection factors.

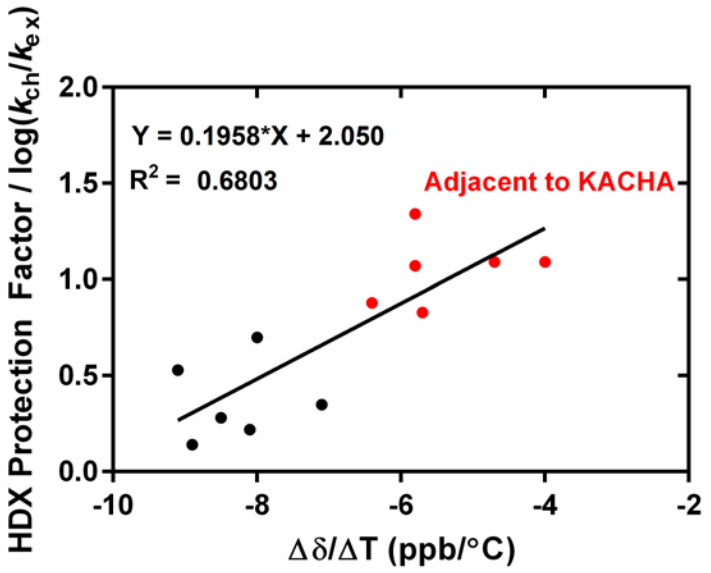

Figure S21. Correlation between temperature coefficient (Δδ/ΔT) and HDX protection factors for α-residues in **1**-**4**. α-Residues immediately following KACHA, which are expected to be most engaged in H-bonding based on HDX analysis, are shown in red.

Although the H_α CSD data were inconclusive, it is instructive to examine how well the data correlate with the other three measurements to convince ourselves that useful information cannot

be extracted from CSD data in α/γ-peptides (**Figure S22**). The correlations between H_α CSD and $^3J_{HN-H\alpha}$, temperature coefficient, and HDX protection factor are all very poor, with R^2 values all less than 0.03.

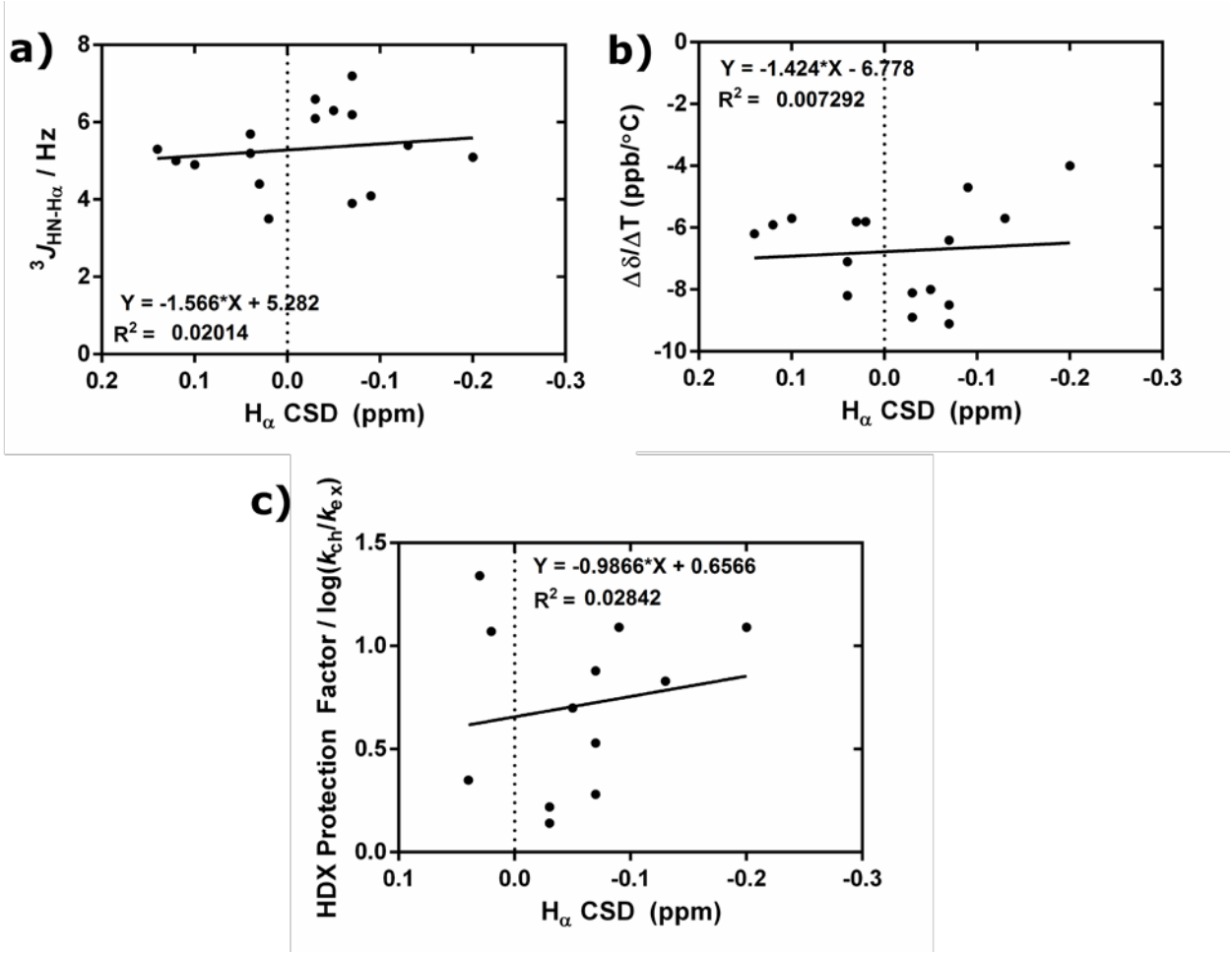

Figure S22. a) Correlation between H_α CSD and $^3J_{HN-H\alpha}$ of α-residues in **1**-**4**. b) Correlation between H_α CSD and temperature coefficient (Δδ/ΔT) of α-residues in **1**-**4**. c) Correlation of H_α CSD and HDX protection factors in **1**-**4**.

On the whole, temperature gradients, $^3J_{HN-H\alpha}$ coupling constants, and HDX protection factors unite with 2D-ROESY data to form a more complete picture of α/γ-peptide structure in solution. H_α CSD data was analyzed but found to not correlate with the other NMR observables. The structure-disrupting capabilities of polar solvents may warrant a more thorough approach than NOE data alone in structure analysis of short peptides. It is hoped that once novel solution-phase structural data in $CDCl_3$ is finally exhausted, similarly meticulous approaches will be employed to guard against the spurious conclusions that may emerge from naïve interpretation of NOE crosspeaks in unstructured peptide foldamers. Recall that unstructured peptide **1** featured long-range crosspeaks that could not be assigned to secondary structure. In other cases, a set of NOE crosspeaks observed in an unstructured foldamer may map to a single (incorrect) structural interpretation, resulting in spurious conclusions. For strongly structure-promoting chloroform, this is probably an unlikely event; in water, it ought to be guarded against.

E. Resonance Assignments

Table S9. Resonance assignment of **1** in CD_3OH.

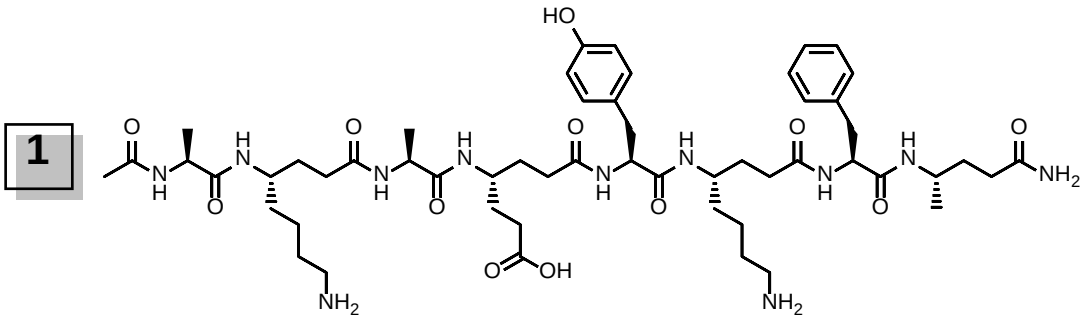

Ala1 gLys2 Ala3 gGlu4 Tyr5 gLys6 Phe7 gAla8

	Backbone				Sidechain					
Residue	**NH**	**γ**	**β**	**α**	**HB'**	**HG'**	**HD'**	**HE'**	**HZ'**	**^3J (Hz)**
N-terminus	Ac: 2.010									
Ala1	8.263			4.183	1.415					5.9
γLys2	7.746	3.744		2.286						9.8
Ala3	8.214			4.160	1.403					5.7
γGlu4	7.919	3.775		2.307						9.9
Tyr5	8.065			4.372	2.844, 3.077		7.124	6.727		6.6
γLys6	7.910	3.793		2.120, 2.152						10.0
Phe7	7.935			4.513	2.916, 3.197		7.295	7.295	7.209	7.3
γAla8	8.100	3.931	1.698	2.120	1.162					9.2
C-Terminus	H1: 6.769	H2: 7.526								

Table S10. Resonance assignment of **1** in H_2O.

	Backbone				Sidechain					
Residue	**NH**	**γ**	**β**	**α**	**HB'**	**HG'**	**HD'**	**HE'**	**HZ'**	**^3J (Hz)**
N-terminus	Ac: 2.013									
Ala1	8.198			4.160	1.374					5.7
γLys2	7.836	3.688								9.3
Ala3	8.085			4.165	1.372					5.2
γGlu4	7.846	3.713								9.5
Tyr5	8.090			4.416	2.951		7.163	6.820		6.1
γLys6	7.802	3.623	1.606	1.742, 1.870	1.392					10.0
Phe7	7.907			4.435	3.010, 3.062		7.275	7.368		6.6
γAla8	7.836	3.723	1.427, 1.559	1.753, 1.865	1.031					9.5
C-Terminus	H1: 6.759	H2: 7.276								

Table S11. Resonance assignment of **2** in CD_3OH.

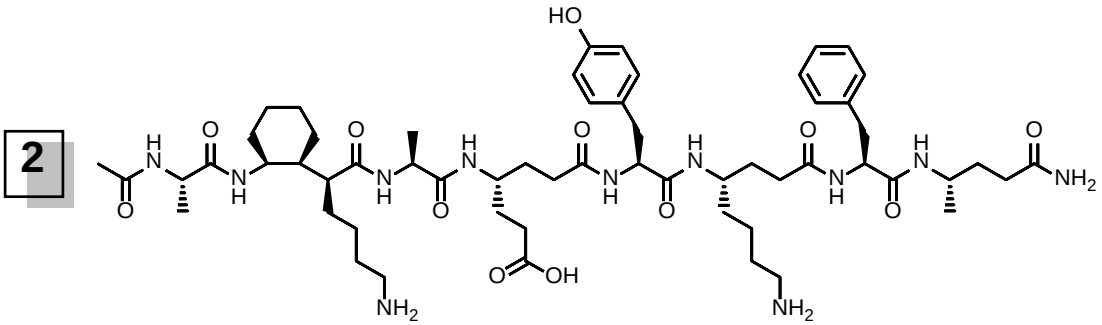

	Backbone				Sidechain					
Residue	**NH**	**γ**	**β**	**α**	**HB'**	**HG'**	**HD'**	**HE'**	**HZ'**	**^3J (Hz)**
N-terminus	Ac: 2.074									
Ala1	8.451			4.303	1.428					5.7
KACHA2	7.327	3.960	1.590	2.093				2.930	7.784	10.5
Ala3	8.073			4.054	1.442					4.2
γGlu4	8.221	3.834	1.580	2.187, 2.317	1.842, 1.937	2.322				10.1
Tyr5	8.017			4.300	2.859, 3.041		7.156	6.729		6.1
γLys6	7.922	3.772	1.527	2.143	1.850			2.930	7.784	10.1
Phe7	7.903			4.501	2.924, 3.196		7.305			7.6
γAla8	8.094	3.933	1.707	2.132	1.172					9.3
C-Terminus	H1: 6.769	H2: 7.540								

Table S12. Resonance assignment of **2** in H_2O.

	Backbone				Sidechain					
Residue	**NH**	**γ**	**β**	**α**	**HB'**	**HG'**	**HD'**	**HE'**	**HZ'**	**^3J (Hz)**
N-terminus	Ac: 2.050									
Ala1	8.483			4.259	1.418					5.3
KACHA2	7.600	3.765	–	2.035						10.4
Ala3	8.168			4.049	1.420					3.9
γGlu4	8.105	3.797	1.536, 1.827	2.290	1.742, 1.849					9.4
Tyr5	8.299			4.374	2.956		7.166	6.817		6.2
γLys6	7.986	3.615		1.790						9.8
Phe7	8.104			4.396	2.971, 3.103					7.2
γAla8	7.986	3.697	1.383, 1.524	1.607, 1.775	1.052					9.8
C-Terminus	H1: 6.888	H2: 7.413								

Table S13. Resonance assignment of **3** in CD_3OH.

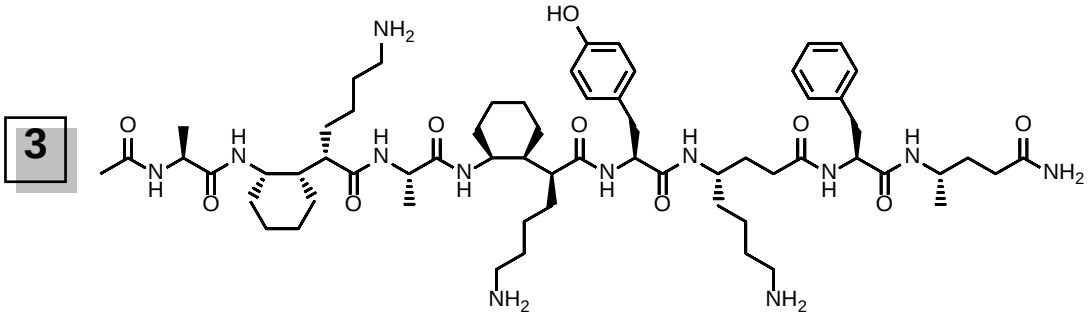

Ala1 KACHA2 Ala3 KACHA4 Tyr5 gLys6 Phe7 gAla8

	Backbone				Sidechain					
Residue	**NH**	**γ**	**β**	**α**	**HB'**	**HG'**	**HD'**	**HE'**	**HZ'**	**^3J (Hz)**
N-terminus	Ac: 2.108									
Ala1	8.549			4.235	1.443					5.1
KACHA2	7.361	4.120	–	2.127						10.0
Ala3	7.940			3.998	1.457					2.2
KACHA4	8.491	4.121	–	2.089						10.4
Tyr5	8.139			4.097			7.352	6.753		4.9
γLys6	8.351	3.872		2.316						9.8
Phe7	7.856			4.437	2.899, 3.207		7.339	7.272		7.0
γAla8	8.117	3.977	1.767	2.174	1.198					9.1
C-Terminus	H1: 6.801	H2: 7.567								

Table S14. Resonance assignment of **3** in H_2O.

	Backbone				Sidechain					
Residue	**NH**	**γ**	**β**	**α**	**HB'**	**HG'**	**HD'**	**HE'**	**HZ'**	**^3J (Hz)**
N-terminus	Ac: 2.072									
Ala1	8.531			4.223	1.432					4.9
KACHA2	7.540	3.936		2.080						10.8
Ala3	7.995			4.139	1.444					3.5
KACHA4	8.051	3.945		1.924						10.7
Tyr5	7.922			4.246	2.935, 3.080		7.317	6.852		5.1
γLys6	7.959	3.740		2.158						10.2
Phe7	8.125			4.415	3.002, 3.077		7.280	HEZ: 7.355		6.3
γAla8	8.008	3.727	1.417	1.841	1.059					9.4
C-Terminus	H1: 6.904	H2: 7.447								

Table S15. Resonance assignment of **4** in CD_3OH.

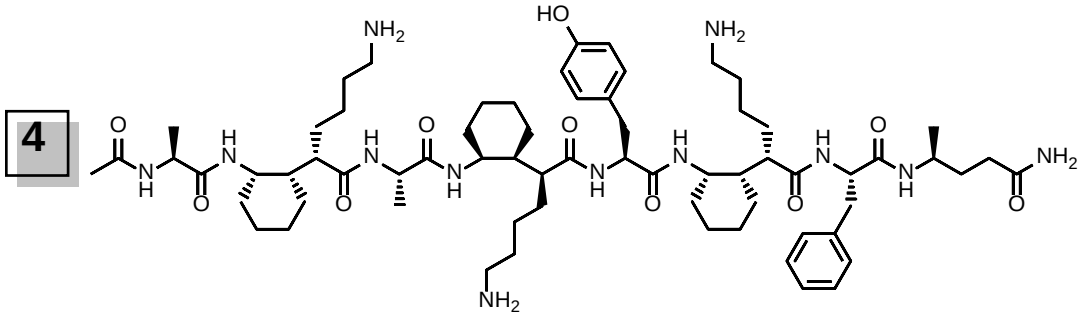

	Backbone				Sidechain					
Residue	**NH**	**γ**	**β**	**α**	**HB'**	**HG'**	**HD'**	**HE'**	**HZ'**	**^3J (Hz)**
N-terminus	Ac: 2.103									
Ala1	8.552			4.250	1.452					5.8
KACHA2	7.369	4.157		2.120	–	–	1.616, 1.719	2.904	7.766	11.0
Ala3	7.945			4.039	1.459					2.1
KACHA4	8.536	4.255		2.234	–	1.088	1.592	2.765	7.769	10.7
Tyr5	8.330			4.138	3.010		7.235	6.722		2.7
KACHA6	8.729	4.150		2.052	1.775	0.418, 0.624	1.231, 1.347	2.527	7.693	10.6
Phe7	8.037			4.195	2.799, 3.205		7.548	7.294	7.294	6.0
γAla8	8.552	4.007	1.737, 1.802	2.191	1.189					8.9
C-Terminus	H1: 6.769	H2: 7.390								

Table S16. Resonance assignment of **4** in H_2O.

	Backbone				Sidechain					
Residue	**NH**	**γ**	**β**	**α**	**HB'**	**HG'**	**HD'**	**HE'**	**HZ'**	**^3J (Hz)**
N-terminus	Ac: 2.072									
Ala1	8.531			4.223	1.432					4.9
KACHA2	7.540	3.936		2.080						10.8
Ala3	7.995			4.139	1.444					3.5
KACHA4	8.051	3.945		1.924						10.7
Tyr5	7.922			4.246	2.935, 3.080		7.317	6.852		5.1
γLys6	7.959	3.740		2.158						10.2
Phe7	8.125			4.415	3.002, 3.077		7.280	HEZ: 7.355		6.3
γAla8	8.008	3.727	1.417	1.841	1.059					9.4
C-Terminus	H1: 6.904	H2: 7.447								

F. ROESY Crosspeak Assignments

Table S17. ROESY crosspeaks detected for **1** in CD_3OH.

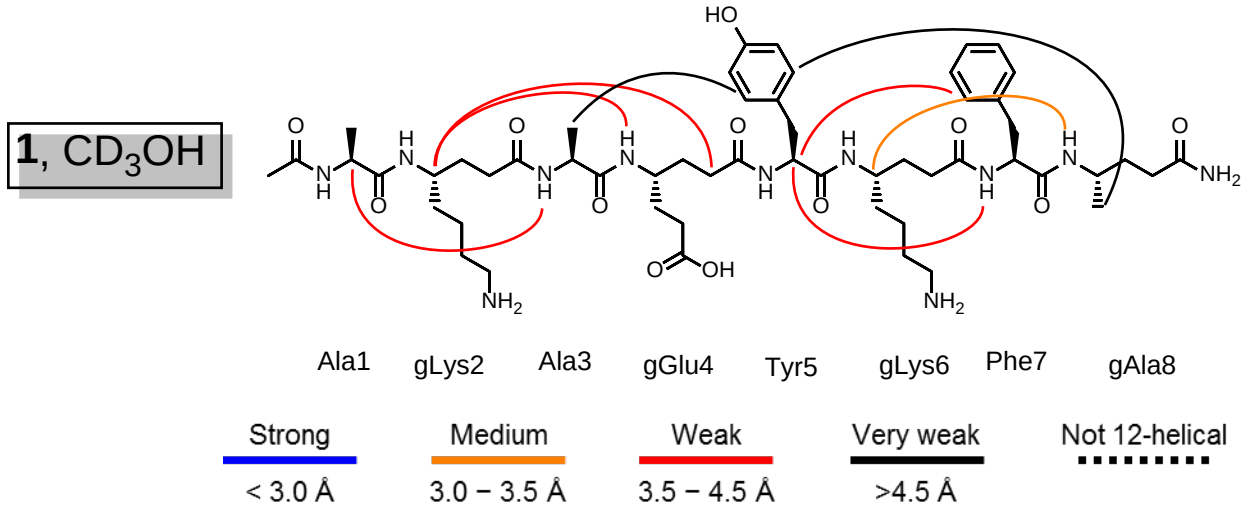

Atom 1	Atom 2	"Distance"	Designation
Reference distance			
Tyr5(Hδ)	(Hε)	2.80	
Sequential NOEs			
gLys2(HN)	Ala1(Hα)	2.8	Strong
Ala3(HN)	gLys2(Hα)	3.0	Medium
Ala1(HN)	gLys2(HN)	2.6	Strong
gGlu4(HN)	Ala3(Hα)	3.1	Medium
Tyr5(HN)	gGlu4(Hα)	3.1	Medium
Ala3(HN)	gGlu4(HN)	3.0	Strong
gLys6(HN)	Tyr5(Hα)	3.1	Medium
Phe7(HN)	gLys6(Hα2)	2.8	Strong
Tyr5(HN)	gLys6(HN)	2.7	Strong
gAla8(HN)	Phe7(Hα)	3.1	Medium
gAla8(HN)	Phe7(HN)	3.2	Medium
gAla8(HN)	Phe7(HδE)	5.5	Very weak
gLys6(HN)	Tyr5(Hδ)	4.1	Weak
gAla8(HN)	Phe7(Hβ2)	3.7	Weak
gAla8(Hα)	Phe7(HδE)	5.2	Very weak
Phe7(HδE)	gAla8(Hβ')	5.5	Very weak
gAla8(HN)	Phe7(HδE)	4.6	Very weak
Long-range NOEs			
gLys2(Hγ)	gGlu4(Hα)	3.8	Weak
gGlu4(HN)	gLys2(Hγ)	3.8	Weak
Ala3(HN)	Ala1(Hα)	4.0	Weak

Tyr5(Hα)	Phe7(HN)	5.0	Very weak
gAla8(HN)	gLys6(Hγ)	3.0	Medium
Tyr5(Hδ)	Ala3(Hβ)	5.2	Very weak
Tyr5(Hα)	Phe7(HδE)	5.0	Very weak
Tyr5(Hδ)	gAla8(Hβ')	5.0	Very weak
Tyr5(Hδ)	Ala3(Hβ)	5.4	Very weak
Ala3(Hα)	Tyr5(HN)	5.0	Very weak

Table S18. ROESY crosspeaks detected for **1** in H_2O.

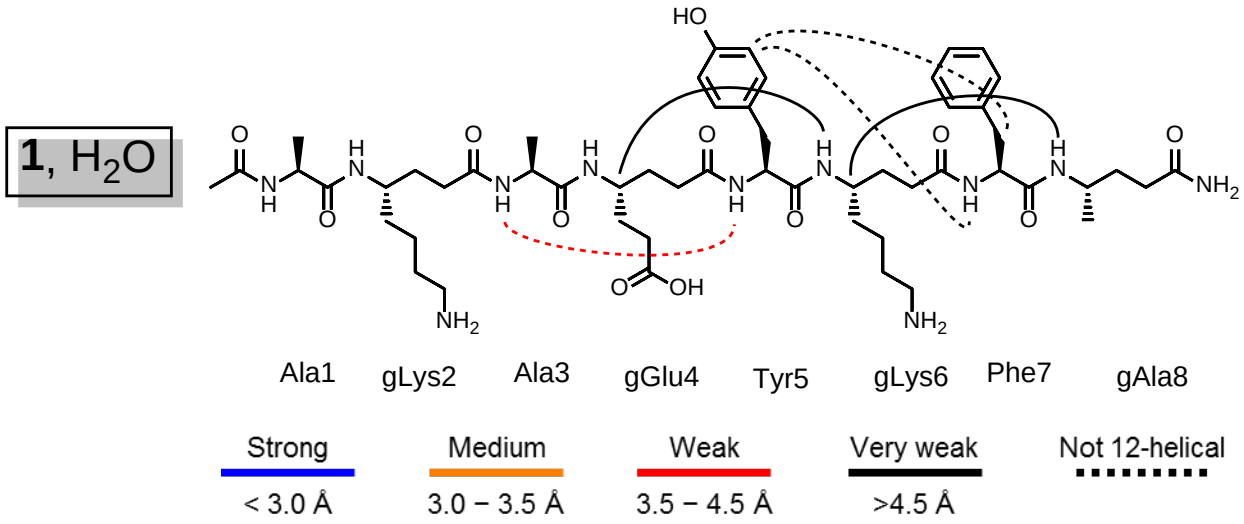

Atom 1	Atom 2	"Distance"	Designation
Reference distance			
Tyr5(Hδ)	(Hε)	2.80	
Sequential NOEs			
Ala3(HN)	gLys2(Hα)	3.3	Medium
Ala1(HN)	gLys2(HN)	3.4	Medium
gGlu4(HN)	Ala3(Hα)	2.7	Strong
Tyr5(HN)	gGlu4(Hγ)	3.6	Weak
Ala3(HN)	gGlu4(HN)	3.5	Weak
Tyr5(HN)	gLys4(Hα)	3.0	Strong
gLys6(HN)	Tyr5(Hα)	3.0	Strong
gLys6(HN)	Tyr5(Hβ)	4.2	Weak
Tyr5(Hδ)	gLys6(Hα1)	4.3	Weak
Tyr5(Hδ)	gLys6(HN)	4.1	Weak
gLys6(Hα1)	Tyr5(Hε)	4.7	Very weak
Phe7(HN)	gLys6(Hα1)	3.3	Medium
Tyr5(Hδ)	gLys6(Hα2)	4.6	Very weak
gLys6(Hα2)	Tyr5(Hε)	3.8	Weak
Phe7(HN)	gLys6(Hα2)	3.0	Medium

gLys6(Hβ)	Tyr5(Hδ)	5.1	Very weak
gLys6(Hβ)	Tyr5(Hε)	5.2	Very weak
Phe7(HN)	gLys6(Hβ)	4.5	Weak
Phe7(HN)	gLys6(Hγ)	4.4	Weak
Tyr5(HN)	gLys6(HN)	3.7	Weak
gAla8(HN)	Phe7(Hα)	3.0	Strong
Phe7(Hβ1)	gAla8(HN)	3.8	Weak
Phe7(Hβ2)	gAla8(HN)	4.1	Weak
Phe7(Hδ)	gAla8(Hβ')	5.9	Very weak
Phe7(Hδ)	gAla8(Hβ2)	4.5	Weak
Phe7(Hδ)	gAla8(Hγ)	5.1	Very weak
Long-range NOEs			
gGlu4(Hγ)	gLys6(HN)	5.0	Very weak
Tyr5(Hα)	Ala3(HN)	3.8	Weak
Tyr5(Hε)	Phe7(Hβ2)	5.0	Very weak
Phe7(HN)	Tyr5(Hε)	4.9	Very weak
gAla8(HN)	gLys6(Hγ)	5.0	Very weak

Table S19. ROESY crosspeaks detected for **2** in CD_3OH.

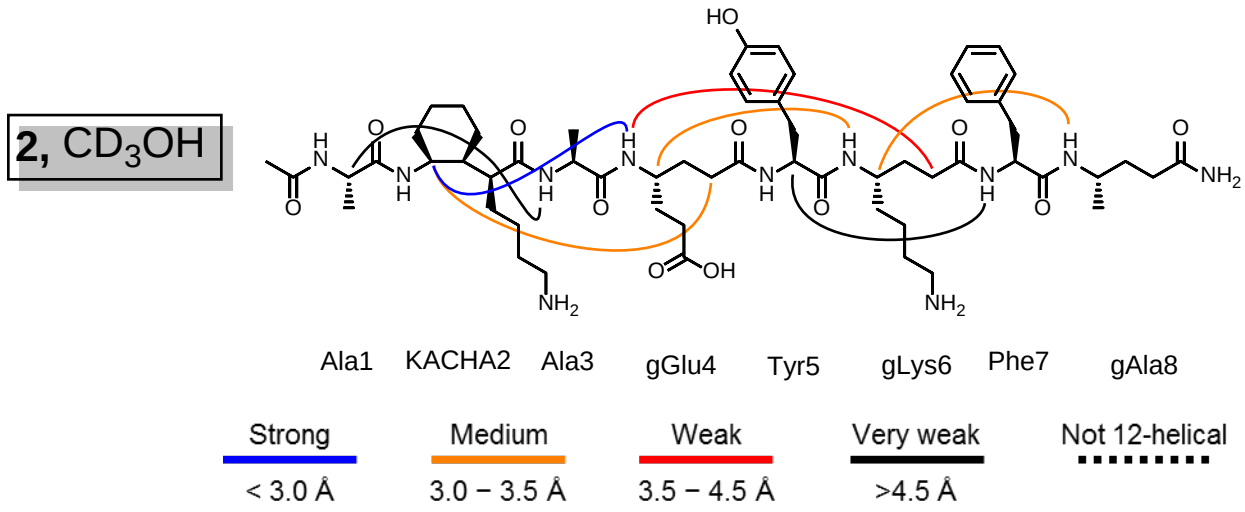

Atom 1	Atom 2	"Distance"	Designation
Reference distance			
Tyr5(Hδ)	(Hε)	2.80	
Sequential NOEs			
gLys2(HN)	Ala1(Hα)	3.0	Medium
Ala3(HN)	gLys2(Hα)	3.0	Medium
Ala1(HN)	gLys2(HN)	3.0	Strong
Ala3(Hβ)	gGlu4(HN)	3.6	Weak
Ala3(Hα)	gGlu4(HN)	3.1	Medium

gGlu4(HN)	Ala3(HN)	3.2	Medium
Tyr5(HN)	gGlu4(Hα1)	3.3	Medium
Tyr5(HN)	gGlu4(Hα2)	2.9	Strong
KACHA6(HN)	Tyr5(Hα)	3.1	Medium
KACHA6(Hα)	Phe7(HN)	3.2	Medium
Tyr5(HN)	KACHA6(HN)	3.1	Medium
gAla8(HN)	Phe7(Hα)	3.2	Medium
gAla8(HN)	Phe7(HN)	2.9	Strong
Long-range NOEs			
gGlu4(HN)	gLys2(Hγ)	2.9	Strong
gLys2(Hγ)	gGlu4(Hα2)	3.0	Medium
KACHA6(HN)	gGlu4(Hγ)	3.1	Medium
gGlu4(Hγ)	KACHA6(Hα)	4.5	Very weak
KACHA6(Hγ)	gAla8(HN)	3.5	Medium
Ala1(Hα)	Ala3(HN)	4.5	Very weak
Tyr5(Hα)	Phe7(HN)	5.0	Very weak

Table S20. ROESY crosspeaks detected for **2** in H_2O.

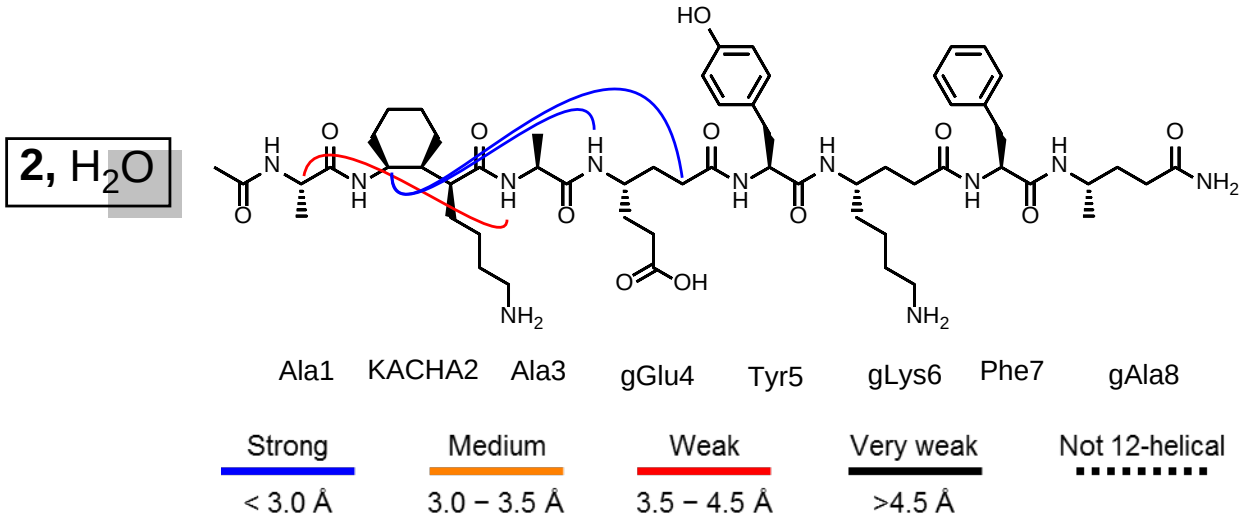

Atom 1	Atom 2	"Distance"	Designation
Reference distance			
Tyr5(Hδ)	(Hε)	2.80	
Sequential NOEs			
KACHA2(HN)	Ala1(Hα)	3.0	Medium
Ala3(HN)	KACHA2(Hα)	2.7	Strong
Ala3(HN)	KACHA2(Hγ)	3.7	Weak
Ala1(HN)	KACHA2(HN)	3.2	Medium
gGlu4(HN)	Ala3(Hα)	2.9	Strong
gGlu4(HN)	Ala3(Hβ)	3.9	Weak

Tyr5(HN)	gGlu4(Hα)	3.1	Medium
gGlu4(Hγ)	Tyr5(HN)	4.1	Weak
gLys6(HN)	Tyr5(Hα)	2.9	Strong
gLys6(HN)	Tyr5(Hβ)	4.0	Weak
Tyr5(Hδ)	gLys6(HN)	3.7	Weak
Phe7(HN)	gLys6(Hα)	3.1	Medium
Tyr5(HN)	gLys6(HN)	3.8	Weak
gAla8(HN)	Phe7(Hα)	2.6	Strong
Long-range NOEs			
Ala1(Hα)	Ala3(HN)	4.4	Weak
gGlu4(HN)	KACHA2(Hγ)	2.9	Strong
KACHA2(Hγ)	gGlu4(Hα)	2.9	Strong

Table S21. ROESY crosspeaks detected for **3** in CD_3OH.

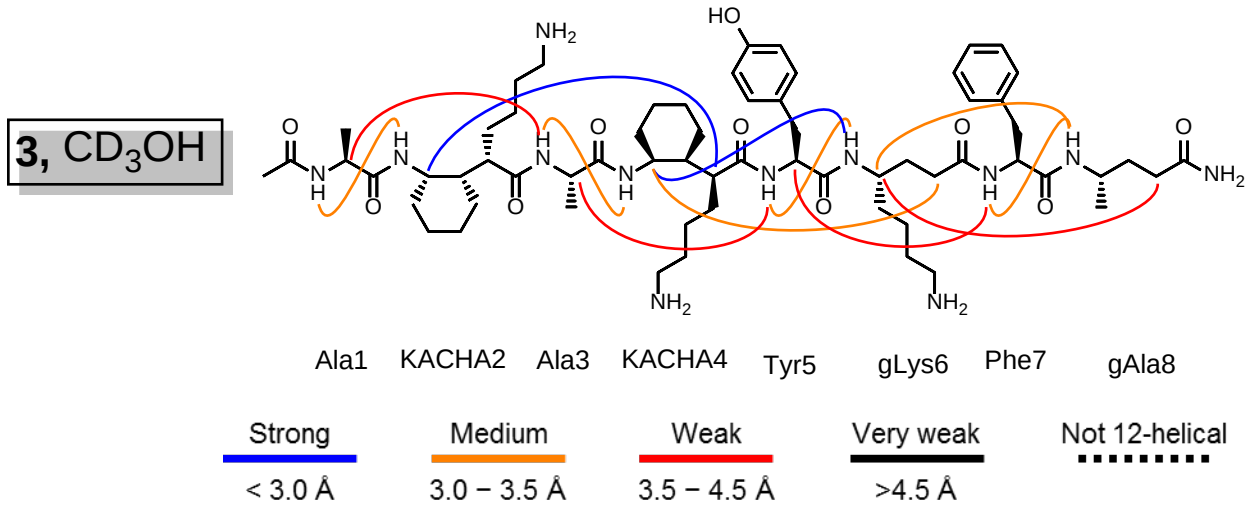

Atom 1	Atom 2	"Distance"	Designation
Reference distance			
Tyr5(Hδ)	(Hε)	2.80	
Sequential NOEs			
KACHA2(HN)	Ala1(Hα)	3.0	Strong
Ala3(HN)	KACHA2(Hα)	2.5	Strong
Ala1(HN)	KACHA2(HN)	3.3	Medium
Ala3(Hα)	KACHA4(HN)	4.2	Weak
KACHA4(HN)	Ala3(HN)	3.4	Medium
Tyr5(HN)	KACHA4(Hα)	2.6	Strong
gLys6(HN)	Tyr5(Hβ1)	4.0	Weak
Tyr5(Hβ2)	gLys6(HN)	4.2	Weak
gLys6(HN)	Tyr5(HN)	3.1	Medium
Phe7(HN)	gLys6(Hα)	3.0	Medium

gLys6(Hγ)	Phe7(HN)	3.8	Weak
gAla8(HN)	Phe7(Hα)	3.3	Medium
gAla8(HN)	Phe7(HN)	3.1	Medium
Long-range NOEs			
Ala1(Hα)	Ala3(HN)	3.7	Weak
Tyr5(HN)	Ala3(Hα)	3.8	Weak
KACHA2(Hγ)	KACHA4(Hα)	2.6	Strong
gLys6(HN)	KACHA4(Hγ)	2.8	Strong
Tyr5(Hα)	Phe7(HN)	4.2	Weak
KACHA4(Hγ)	gLys6(Hα)	3.3	Medium
gAla8(HN)	gLys6(Hγ)	3.4	Medium
gLys6(Hγ)	gAla8(Hα)	4.2	Weak

Table S22. ROESY crosspeaks detected for **3** in H_2O.

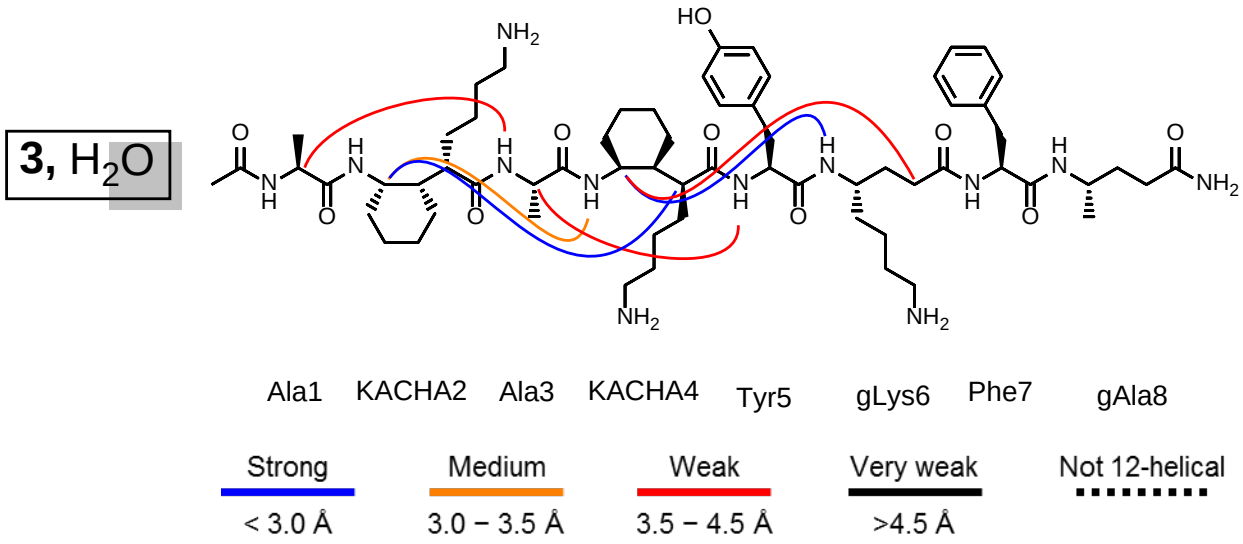

Atom 1	Atom 2	"Distance"	Designation
Reference distance			
Tyr5(Hδ)	(Hε)	2.80	
Sequential NOEs			
KACHA2(HN)	Ala1(Hα)	3.1	Medium
Ala3(HN)	KACHA2(Hα)	2.6	Strong
Ala1(HN)	KACHA2(HN)	3.4	Medium
KACHA4(HN)	Ala3(Hα)	2.8	Strong
KACHA4(Hα)	Tyr5(HN)	2.7	Strong
Ala3(HN)	KACHA4(Hγ)	4.2	Weak
Tyr5(HN)	KACHA4(Hγ)	3.6	Weak
gLys6(HN)	Tyr5(Hα)	3.1	Medium
Phe7(HN)	gLys6(Hα)	3.3	Medium

gLys6(Hγ)	Phe7(HN)	4.2	Weak
gAla8(HN)	Phe7(Hα)	2.8	Strong
gAla8(HN)	Phe7(Hδ)	4.4	Weak
gAla8(HN)	Phe7(HN)	3.3	Medium
Long-range NOEs			
Ala1(Hα)	Ala3(HN)	3.9	Weak
KACHA4(HN)	KACHA2(Hγ)	3.2	Medium
Ala3(Hα)	Tyr5(HN)	4.0	Weak
KACHA2(Hγ)	KACHA4(Hα)	2.8	Strong
gLys6(HN)	KACHA4(Hγ)	3.0	Strong
KACHA4(Hγ)	gLys6(Hα)	3.6	Weak

Table S23. ROESY crosspeaks detected for **4** in CD_3OH.

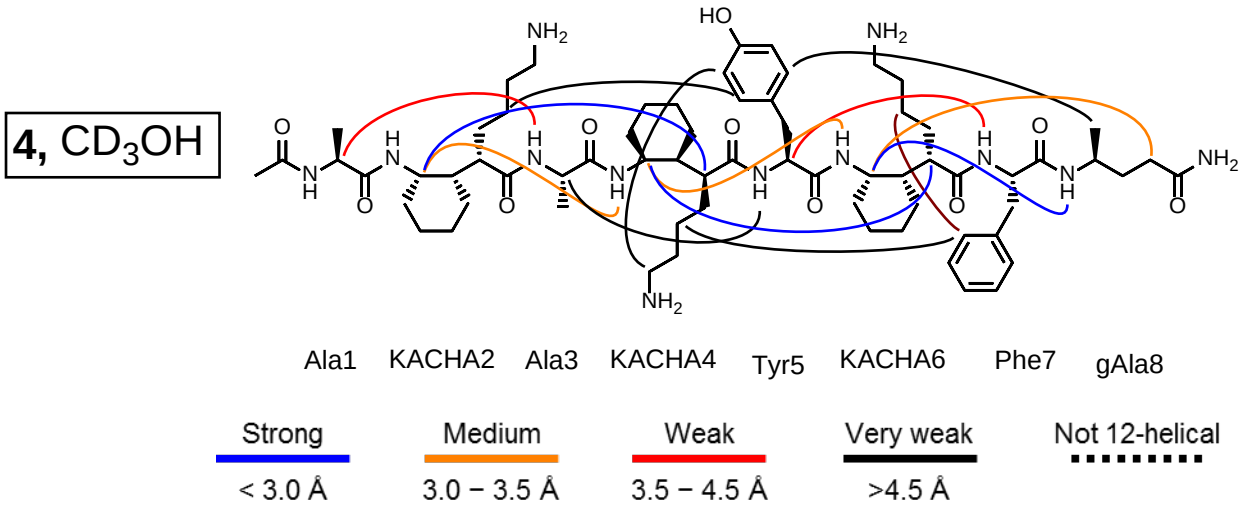

Atom 1	Atom 2	"Distance"	Designation
Reference distance			
Tyr5(Hδ)	(Hε)	2.80	
Sequential NOEs			
KACHA2(HN)	Ala1(Hα)	3.3	Medium
Ala3(HN)	KACHA2(Hα)	2.6	Strong
KACHA2(Hγ)	Ala3(HN)	3.9	Weak
Ala1(HN)	KACHA2(HN)	3.2	Medium
KACHA4(HN)	Ala3(HN)	3.4	Medium
Tyr5(HN)	KACHA4(Hα)	2.6	Strong
KACHA4(Hγ')	Tyr5(Hδ)	5.1	Very weak
KACHA4(Hγ')	Tyr5(HN)	4.3	Weak
KACHA4(Hγ)	Tyr5(HN)	3.8	Weak
KACHA6(HN)	Tyr5(Hβ)	3.5	Medium
KACHA6(HN)	Tyr5(HN)	3.5	Medium

Phe7(HN)	KACHA6(Hα)	2.6	Strong
Phe7(Hβ1)	gAla8(HN)	4.0	Weak
gAla8(HN)	Phe7(HN)	3.2	Medium
KACHA4(Hε')	Tyr5(Hε)	5.0	Very weak
KACHA6(Hγ')	Phe7(Hδ)	5.0	Very weak
Long-range NOEs			
Ala1(Hα)	Ala3(HN)	3.8	Weak
Ala3(Hα)	Tyr5(HN)	4.5	Very weak
KACHA2(Hγ)	KACHA4(Hα)	2.9	Strong
KACHA6(HN)	KACHA4(Hγ)	3.0	Medium
Phe7(HN)	Tyr5(Hα)	3.6	Weak
KACHA4(Hγ)	KACHA6(Hα)	2.9	Strong
gAla8(HN)	KACHA6(Hγ)	2.6	Strong
KACHA6(Hγ)	gAla8(Hα)	3.1	Medium
KACHA2(Hγ')	Tyr5(Hδ)	5.0	Very weak
KACHA4(Hγ')	Phe7(Hδ)	5.0	Very weak
Tyr5(Hδ)	gAla8(Hβ')	5.0	Very weak

Table S24. ROESY crosspeaks detected for **4** in H_2O.

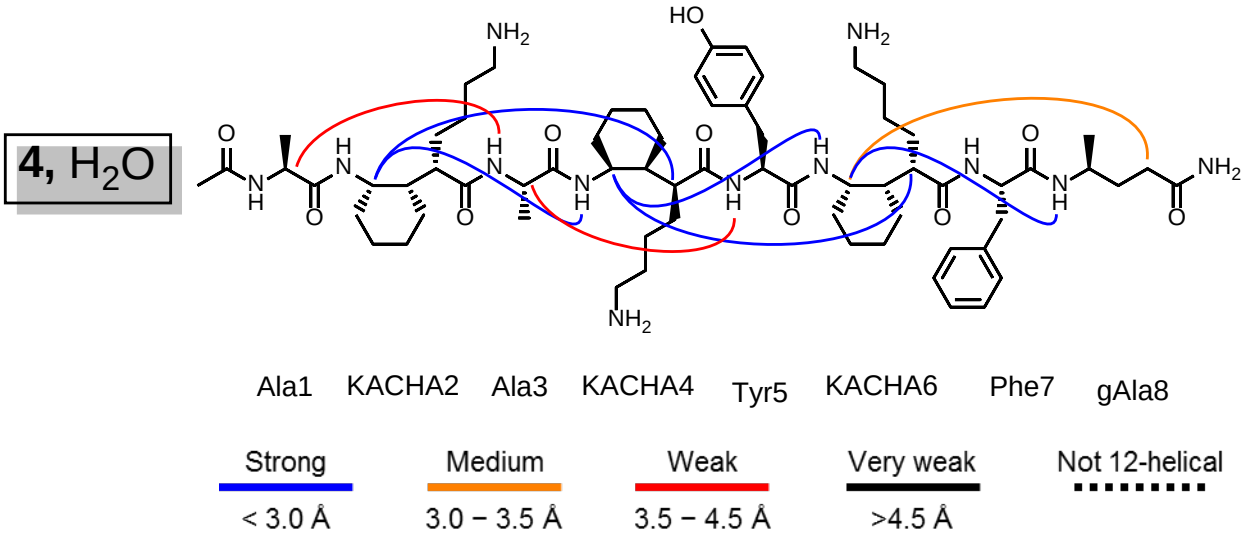

Atom 1	Atom 2	"Distance"	Designation
Reference distance			
Tyr5(Hδ)	(Hε)	2.80	
Sequential NOEs			
KACHA2(HN)	Ala1(Hα)	3.1	Medium
Ala3(HN)	KACHA2(Hα)	2.6	Strong
Ala1(HN)	KACHA2(HN)	3.4	Medium
KACHA4(HN)	Ala3(Hα)	2.8	Strong

KACHA4(Hα)	Tyr5(HN)	2.7	Strong
Ala3(HN)	KACHA4(Hγ)	4.2	Weak
Tyr5(HN)	KACHA4(Hγ)	3.6	Weak
gLys6(HN)	Tyr5(Hα)	3.1	Medium
Phe7(HN)	gLys6(Hα)	3.3	Medium
gLys6(Hγ)	Phe7(HN)	4.2	Weak
gAla8(HN)	Phe7(Hα)	2.8	Strong
gAla8(HN)	Phe7(Hδ)	4.4	Weak
gAla8(HN)	Phe7(HN)	3.3	Medium
Long-range NOEs			
Ala1(Hα)	Ala3(HN)	3.9	Weak
KACHA4(HN)	KACHA2(Hγ)	3.2	Medium
Ala3(Hα)	Tyr5(HN)	4.0	Weak
KACHA2(Hγ)	KACHA4(Hα)	2.8	Strong
gLys6(HN)	KACHA4(Hγ)	3.0	Strong
KACHA4(Hγ)	gLys6(Hα)	3.6	Weak

G. ROESY Crosspeak Charts

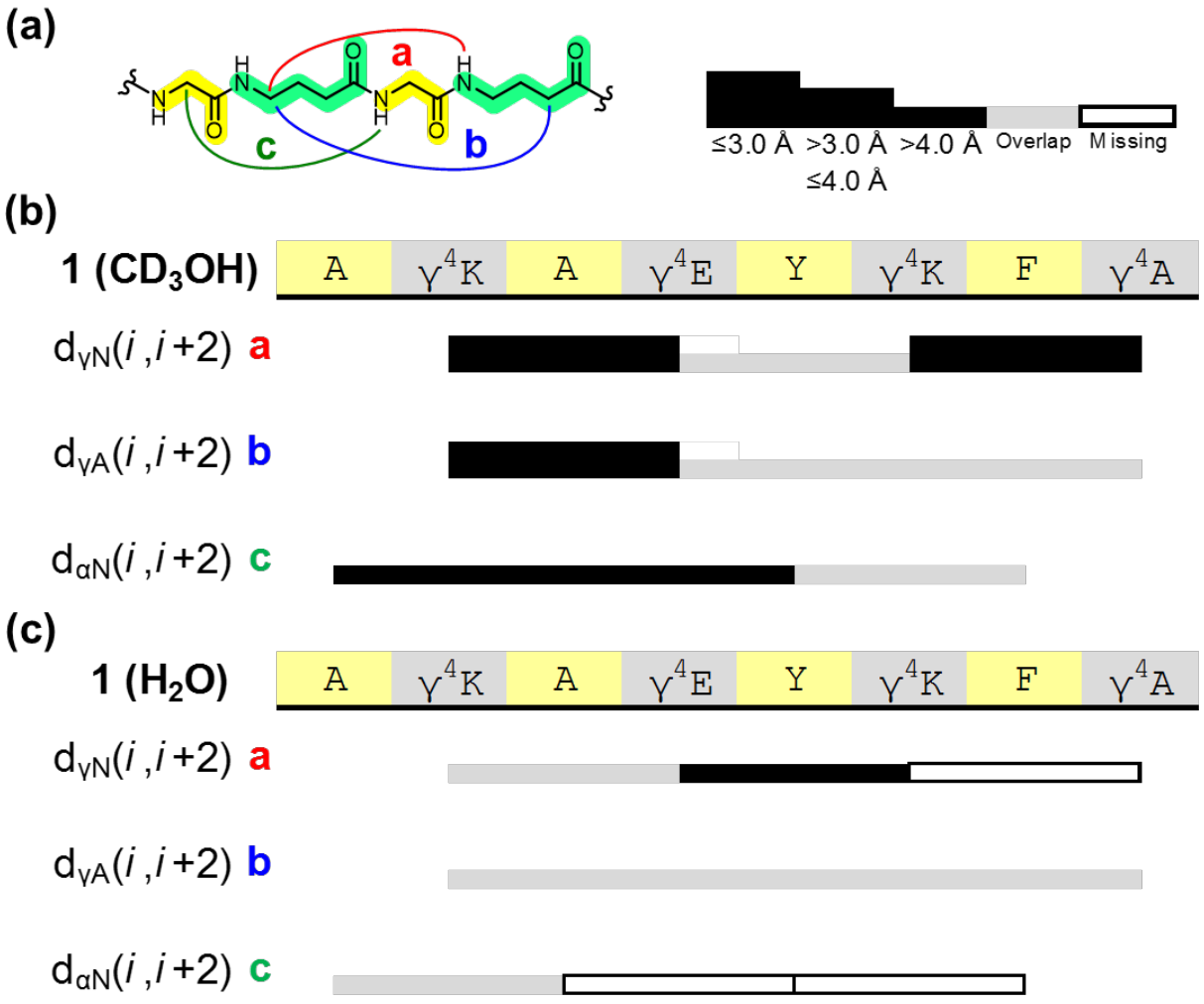

Figure S23. Crosspeak chart for peptide **1**.

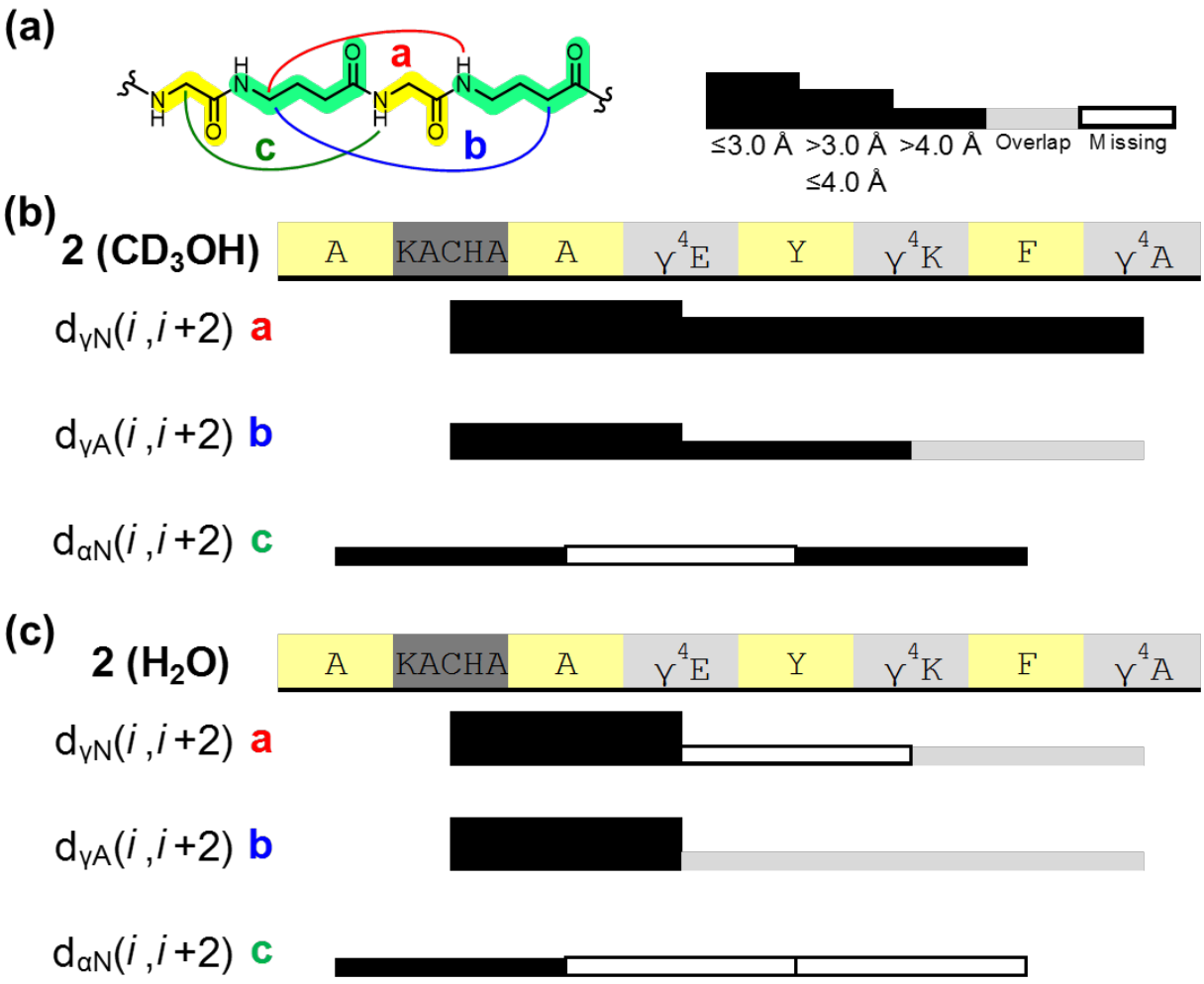

Figure S24. Crosspeak chart for peptide **2**.

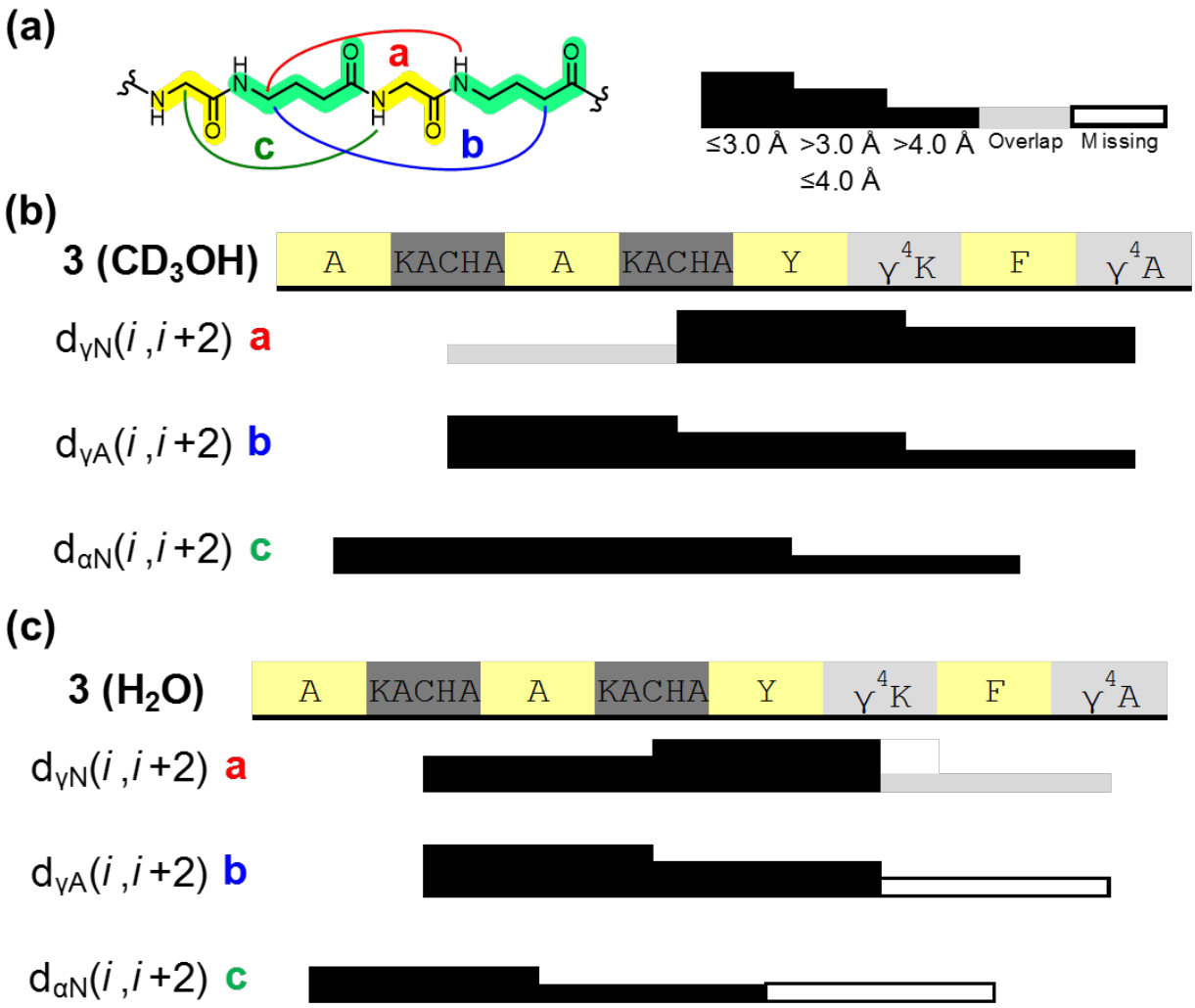

Figure S25. Crosspeak chart for peptide **3**.

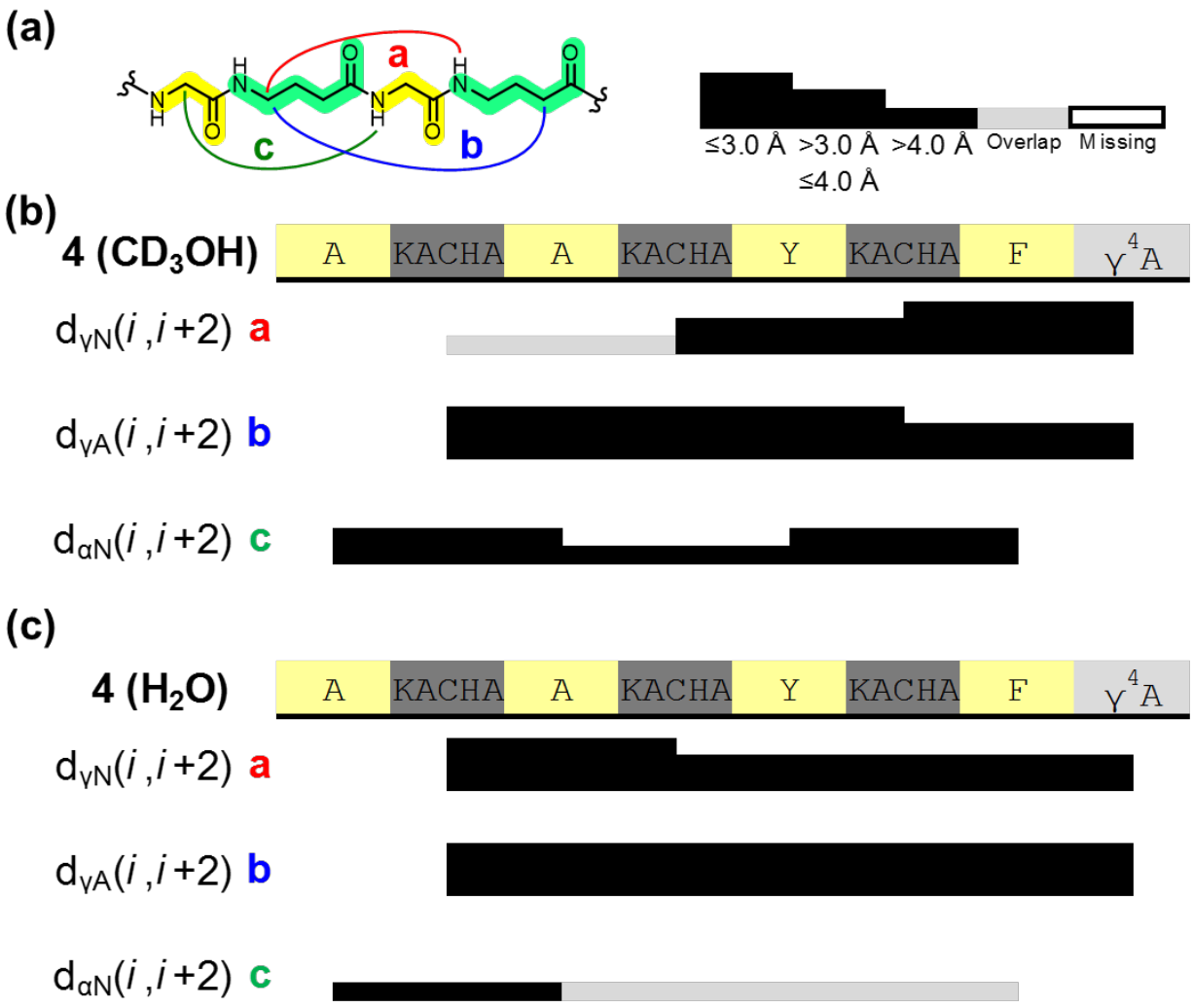

Figure S26. Crosspeak chart for peptide **4**.

H. NMR Structure Calculations

NMR calculation parameters

NMR structural ensembles were obtained with simulated annealing calculations using the Crystallography and NMR System (CNS v1.3) software package.[S36] Molecular topologies, linkage definitions, and parameters for the non-natural residues were built manually. Molecular topology files (.mtf) were generated from the primary sequence using the generate-seq.inp input file included in the CNS software package. The molecular topology files were used as the input to construct extended structures (.pdb) using the generate-ext.inp input file. The .mtf file, the extended .pdb file, the distance restraint table, and a $^{3}J_{HN-H\alpha}$ restraint table (for the methanol experiments; *vide infra*) were the input data in the simulated annealing calculations using anneal.inp as the input file for 100 trial structures. The hot stage was run at 10,000 K for 15 ps in 1000 torsion steps, using 0.1 Van der Waals scale factor, and 150 NOE scale factor. The 1st cooling stage was run from 10,000 K to 0 K in 1000 torsion steps and a 50 K temperature step, using 0.1→1.0 Van der Waals scale factor and 150 NOE scale factor. The 2nd cooling stage was

run from 400 K to 0 K for 15 ps in 3000 Cartesian steps with a 25 K temperature step, using 1.0 →4.0 Van der Waals scale factor and 150 NOE scale factor. A final minimization stage with 10 cycles of 200-step minimization with a 75 NOE scale factor. The 10 structures of the 100 trial structures with the lowest overall energy were selected with the accept.inp input file.

Refinement in explicit water was performed using the re_h2o script[S37] adapted to CNS v1.3, available from the EMBL-EBI Protein Data Bank Europe at https://www.ebi.ac.uk/pdbe/recalculated-nmr-data, to perform a final stage of water refinement. The water refinement input structures were the 10 accepted output structures from NOE distance-restrained (but not J-coupling restrained) CNS v1.3 simulated annealing calculations using identical parameters as for the CD_3OH ROESY distance-restrained calculations. Briefly, for each re_h2o input structure, a 7.0 Å shell of TIP3P water is generated about the molecule then energy-minimized. The system is heated slowly in 1000 steps at 3 fs per step from 100 K to 500 K in 100 K temperature steps. Refinement at 500 K was performed for 2000 steps of 4 fs. The system was cooled from 500 K to 25 K over 4000 steps of 4 fs at 25 K temperature steps. Finally, minimization was performed at 25 K for 200 steps of 4 fs. Precise details of the force field parameters are available in the original publication.

Accepted structures were visualized using PyMOL v1.7.0.3.[S38]

NMR restraint/refinement Selection

For NOE distance restraints used in structure calculations, all intraresidue crosspeak distances were rejected. Nuclei within close rotatable covalent connectivities are particularly prone to over-restraining; the large structural space capable of generating NOE enhancement between intraresidue nuclei results in these restraints not meaningfully causing representation of a mean structure.

Harmonic $^3J_{HN-H\alpha}$ restraints were employed in some calculations. A 1 $kcal \cdot s^2 \cdot mol^{-1}$ harmonic potential about the experimental $^3J_{HN-H\alpha}$ for the α residues was used. Softening the potential to a soft-square potential well of 0.5 Hz, 1.0 Hz, or 2.0 Hz had little impact on the overall structures obtained.

For the CD_3OH simulated annealing calculations, calculations including $^3J_{HN-H\alpha}$ restraints for the α residues were evaluated against calculations without them. The criterion used to evaluate which calculations yielded structural ensembles better approximated the “true” solution conformational ensemble was backbone RMSD: higher backbone RMSD without violating the experimental restraints is interpreted as providing a better conceptual simulation of the backbone flexibility. We found that including J-coupling restraints increased backbone RMSD for most of the peptides, thus we preferred the simulations using them.

For the H_2O calculations, the explicit water-refined structures compared favorably with the *in vacuo* simulated annealing calculations. Overall, the geometries of the final structures were slightly poorer as judged by the deviation from ideal geometry, although the magnitudes remained small and were unlikely to influence the trajectories in a profound way. According to the maximal-RMSD criterion, the water-refined structures provided a superior qualitative depiction of the structural heterogeneity necessarily neglected by NMR conformational determination of molecules, particularly of short peptides. Thus, the water-refined structures were selected for depiction in the body of this paper.

Table S25. Statistics for simulated annealing calculations restrained by NOE distances/J-coupling in CD_3OH

NMR Simulated Annealing	$\mathbf{1}_{MeOH,noJ}$	$\mathbf{2}_{MeOH,noJ}$	$\mathbf{3}_{MeOH,noJ}$	$\mathbf{4}_{MeOH,noJ}$	$\mathbf{1}_{MeOH,J}$	$\mathbf{2}_{MeOH,J}$	$\mathbf{3}_{MeOH,J}$	$\mathbf{4}_{MeOH,J}$
Trial structures	100	100	100	100	100	100	100	100
Distance restraints								
Total NOE	28	20	21	27	28	20	21	27
Intra-residue	0	0	0	0	0	0	0	0
Inter-residue	28	20	21	27	28	20	21	27
Sequential	18	13	13	16	18	13	13	16
Long-range	10	7	8	11	10	7	8	11
$^3J_{HN-H\alpha}$ restraints	0	0	0	0	4	4	4	4
Restraint violations								
Distance restraint violations > 0.5 Å	0.00 ± 0.00	0.00 ± 0.00	0.00 ± 0.00	0.00 ± 0.00	0.00 ± 0.00	0.00 ± 0.00	0.00 ± 0.00	0.00 ± 0.00
J-coupling violations > 1 Hz	–	–	–	–	0.50 ± 0.53	1.70 ± 0.48	1.60 ± 0.52	2.00 ± 0.00
Deviations from idealized geometry								
Bond lengths (Å)	0.038 ± 0.008	0.007 ± 0.000	0.009 ± 0.000	0.010 ± 0.000	0.005 ± 0.000	0.008 ± 0.000	0.009 ± 0.000	0.011 ± 0.000
Bond angles (°)	0.489 ± 0.017	0.560 ± 0.024	0.607 ± 0.018	0.688 ± 0.006	0.534 ± 0.019	0.603 ± 0.014	0.662 ± 0.018	0.764 ± 0.004
Impropers (°)	0.650 ± 0.029	0.701 ± 0.019	0.806 ± 0.005	0.925 ± 0.020	0.657 ± 0.026	0.719 ± 0.007	0.826 ± 0.007	0.931 ± 0.004
Average pairwise RMSD of 10 lowest-energy structures (Å)								
Backbone	0.64 ± 0.19	0.73 ± 0.23	0.30 ± 0.18	0.28 ± 0.09	0.95 ± 0.30	0.85 ± 0.44	0.46 ± 0.14	0.26 ± 0.09
Heavy atom	1.73 ± 0.36	1.92 ± 0.54	1.23 ± 0.34	0.94 ± 0.40	2.32 ± 1.03	2.35 ± 0.76	1.10 ± 0.25	0.69 ± 0.27

Table S26. Statistics for simulated annealing calculations restrained by NOE distances in H_2O and explicit water refinement

NMR Simulated Annealing	$\mathbf{1}_{H2O}$	$\mathbf{2}_{H2O}$	$\mathbf{3}_{H2O}$	$\mathbf{4}_{H2O}$	$\mathbf{1}_{reh2o}$	$\mathbf{2}_{reh2o}$	$\mathbf{3}_{reh2o}$	$\mathbf{4}_{reh2o}$
Trial structures	100	100	100	100	10	10	10	10
Distance restraints								
Total NOE	31	17	19	13	31	17	19	13
Intra-residue	0	0	0	0	0	0	0	0
Inter-residue	31	17	19	13	31	17	19	13
Sequential	26	12	13	7	26	12	13	7
Long-range	5	5	6	6	5	5	6	6
$^3J_{HN-H\alpha}$ restraints	0	0	0	0	0	0	0	0
Restraint violations								
Distance restraint violations > 0.5 Å	0.00 ± 0.00	0.00 ± 0.00	0.00 ± 0.00	0.00 ± 0.00	0.00 ± 0.00	0.00 ± 0.00	0.00 ± 0.00	0.00 ± 0.00
Deviations from idealized geometry								
Bond lengths (Å)	0.006 ± 0.001	0.007 ± 0.000	0.009 ± 0.000	0.010 ± 0.001	0.009 ± 0.001	0.010 ± 0.001	0.011 ± 0.001	0.009 ± 0.000
Bond angles (°)	0.562 ± 0.025	0.5623 ± 0.011	0.643 ± 0.027	0.680 ± 0.018	1.43 ± 0.20	1.32 ± 0.12	1.40 ± 0.10	1.13 ± 0.09
Impropers (°)	0.702 ± 0.025	0.689 ± 0.012	0.885 ± 0.003	0.872 ± 0.010	1.35 ± 0.33	1.21 ± 0.13	1.77 ± 0.30	1.49 ± 0.26
Average pairwise RMSD of 10 lowest-energy structures (Å)								
Backbone	1.83 ± 0.30	1.90 ± 0.41	1.07 ± 0.59	0.23 ± 0.10	2.12 ± 0.30	1.84 ± 0.63	1.79 ± 0.48	0.81 ± 0.10
Heavy atom	4.35 ± 1.40	4.53 ± 1.36	2.93 ± 1.15	1.32 ± 0.31	4.30 ± 0.87	4.04 ± 1.16	3.99 ± 1.18	2.03 ± 0.43

IV. Circular Dichroism

A. Circular Dichroism Experimental

Circular dichroism spectra were acquired on an Aviv Biomedical Model 420 circular dichroism spectrometer at 5°C. Wavelength scans were collected from 260 to 190 nm with a 1 nm bandwidth, 1 nm wavelength step, and an averaging time of 9 sec per step. Solvent blanks were subtracted from the raw spectra prior to normalization to mean residue molar ellipticity (8 residues). Dynode voltage between 190 and 200 nm was >500 V for all samples discussed below, and data in this spectral range are therefore of questionable accuracy; above 200 nm the dynode voltage was at acceptable levels.[S39]

Concentration of each peptide was 400 μM for CD measurements. Each solution for CD analysis was prepared from lyophilized powder that had been dispensed from an aqueous stock solution for which concentration was measured by UV-vis absorbance at 280 nm, based on tyrosine extinction coefficient of 1280 M^{-1} cm^{-1}.[S40] The concentration of each CD sample was rechecked immediately after CD measurements by UV-vis to confirm accuracy.

Peptide solutions in methanol were prepared using spectrophotometric grade methanol from Sigma-Aldrich. Aqueous peptide solutions were prepared with 10 mM acetate buffer, pH 3.8. Buffer absorbance was not excessive above 200 nm.

B. Circular Dichroism Analysis

The spectra in methanol shown in **Figure S27** reveal distinct CD signatures for α/γ-peptides **1** and **2** relative to **3** and **4**; spectra of the latter two are nearly identical to one another and resemble the CD signatures of a set of Aib/γ^4-peptides in methanol reported by Balaram and coworkers.[S41] The methanolic spectrum of **1** has a minimum at 203 nm and a broad positive Cotton effect with a maximum centered at around 222 nm. Introduction of a single cyclic γ-residue changes the spectrum considerably. The positive Cotton effect is almost entirely removed from the CD spectrum of **2**, with only a very weak maximum centered at about 230 nm. The minimum signal red-shifts somewhat to about 208 nm and is less intense. As the second cyclic γ-residue is incorporated to form **3**, the CD minimum continues to move to higher wavelengths, reaching 210 nm, and becomes more intense. The CD maximum that had been observed for **1** and to a lesser extent for **2** is now undiscernible. A maximum appears at around 200 nm for **3**, although the PMT dynode voltage exceeds 500 V at this wavelength; therefore, precision of this measurement is poor. The slope of the curve appears to shift subtly at about 220 nm, suggesting that the negative band between 210-220 nm might have multiple components. Introduction of the third cyclic γ-residue to generate **4** causes no alteration in the CD signature relative to **3**. The CD signature trends across **1**-**4**, in conjunction with the NMR analysis presented in the main text, suggests that minimum between 210-220 nm that is prominent in the spectra for **3** and **4**, but absent in the spectra of **1** and **2**, might be associated with the α/γ-peptide 12-helix secondary structure. We speculate that the positive band observed for **1** may reflect population of a secondary structure that features 9-membered α(*i*) → α(*i+2*) H-bonds across γ residues, interactions which have often been detected in preliminary unrestrained molecular dynamics simulations (in progress).

The aqueous CD spectra, for the most part, resemble the methanolic spectra, but the intensities of features are reduced in aqueous solution (**Figure S28**). The spectrum of **1** nearly flattens to zero > 210 nm; below this wavelength the CD signal becomes increasingly negative, but high dynode voltage was observed in this region. Peptide **2** only has very weak negative intensity around 210-220 nm, but no well-defined minimum. The CD spectra of **3** and **4** align nearly perfectly with one another, as they did in methanol. In aqueous solution, the minimum observed for **3** and for **4** shifts to about 214 nm. The shape of the aqueous CD spectra for **3** and **4** in this region are not as suggestive of multiple minima as were the CD spectra for **3** and **4** in methanol.

The circular dichroism spectra of α/γ-peptides **1**-**4** do not provide unambiguous insight concerning the secondary structure(s) or conformational stabilities of these foldamers. The spectra offer clues that a right-handed α/γ-peptide 12-helix may give rise to a CD signature that features a maximum near 200 nm and a minimum near 210-214 nm. We observe this signature only for the octamers in which at least half the γ residues are cyclically constrained. Comparisons with NMR data, however, suggest that the intensity of this CD signature may not be directly related to 12-helix population. A greater number of long-range NOEs is detected in **4** relative to **3**, which suggests that the helical state of **4** is more highly populated than the helical state of **3**. This inference is supported also by the simulated annealing calculations. Yet, the CD spectra are indistinguishable in methanol and in water. The unique signature of the CD spectrum of **1** in methanol is particularly strange, since NMR data suggests that it adopts conformations similar to those adopted by **2**-**4** in this solvent.

Others have pointed out that the relationship between the structural ensemble of a partially ordered chiral molecule and its circular dichroism spectrum is different from the ensemble's relationship to its NOEs.[S42] It is therefore not necessary that CD and NMR support the same set of structural conclusions. In general, NMR tends to be considerably more informative than CD in terms of conformational analysis of peptides with unnatural backbones. Other authors have noted that CD is not necessarily a useful technique in evaluating hybrid foldamer secondary structure.[S43]

C. Circular Dichroism Spectra

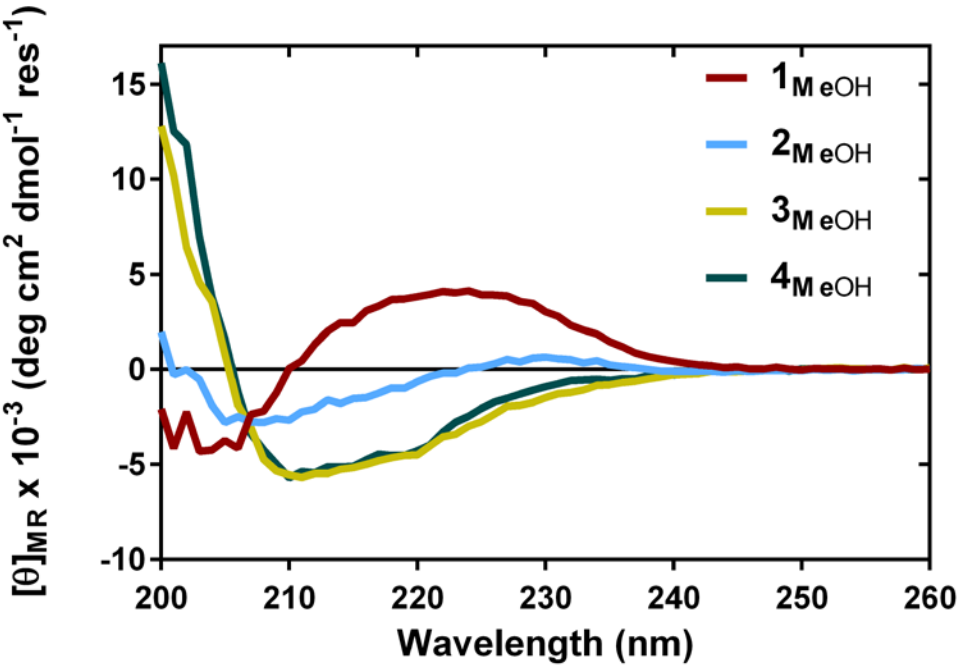

Figure S27. Circular dichroism spectra of peptides **1-4** at 400 μM at 5°C in methanol.

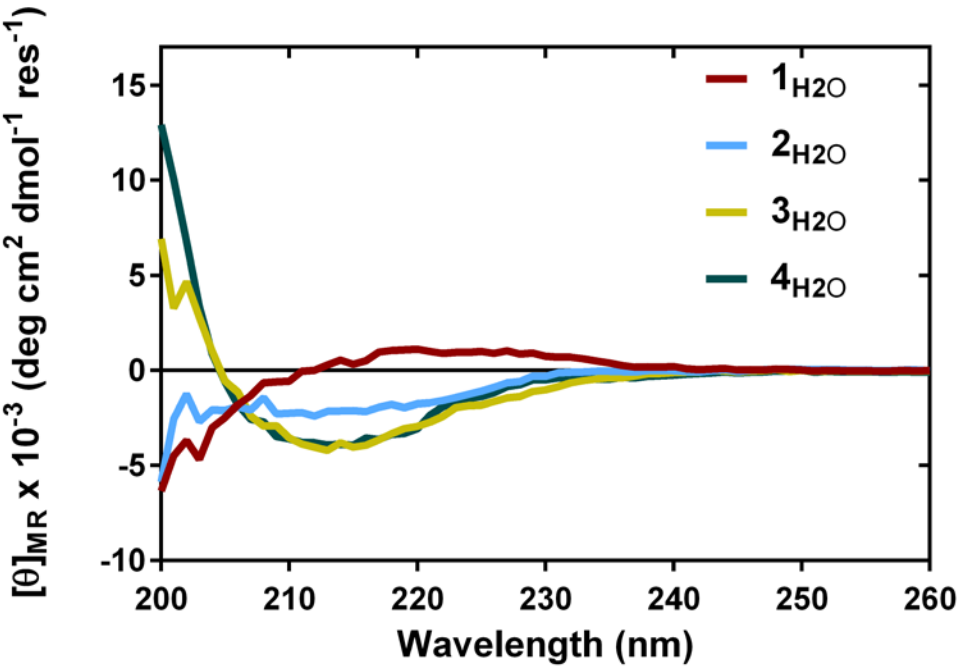

Figure S28. Circular dichroism spectra of peptides **1-4** at 400 μM at 5°C in 10 mM acetate, pH 3.8.

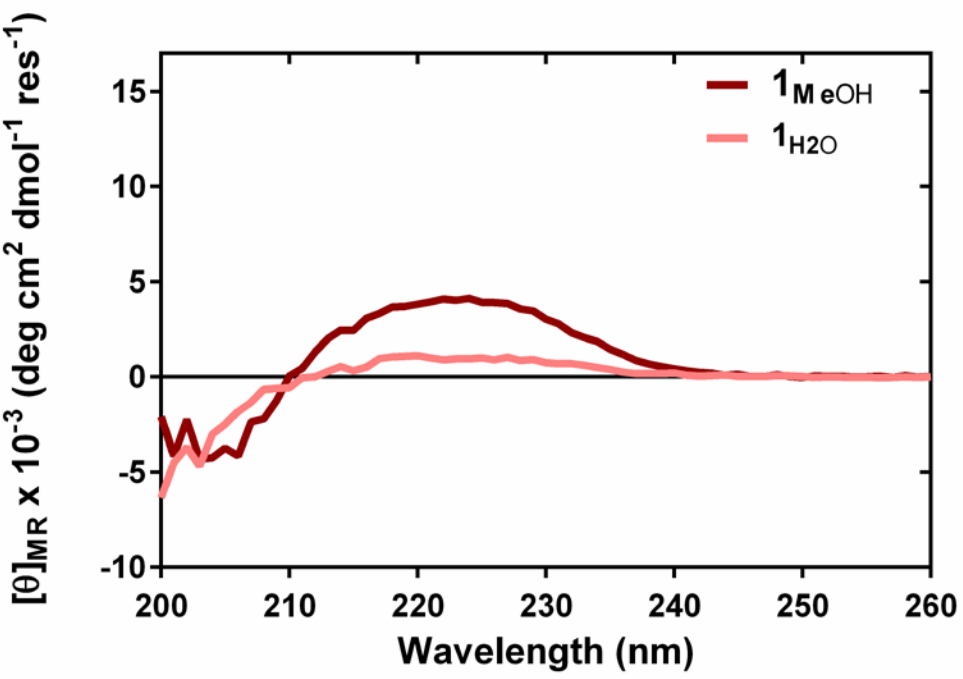

Figure S29. Comparison of CD spectra of peptide **1** in methanol and in 10 mM pH 3.8 acetate buffer (400 µM, 5°C).

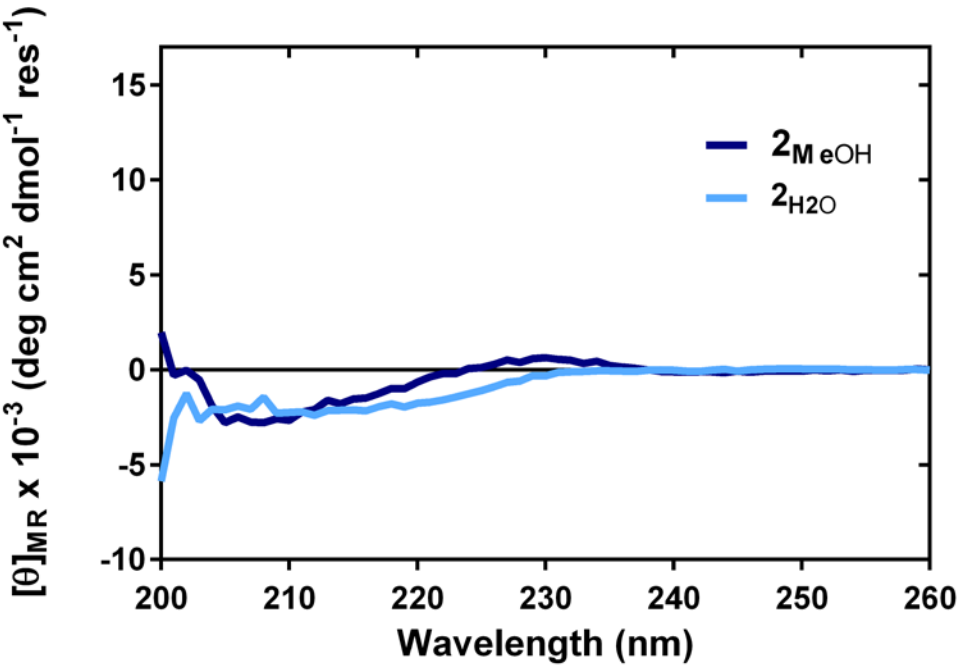

Figure S30. Comparison of CD spectra of peptide **2** in methanol and in 10 mM pH 3.8 acetate buffer (400µM, 5°C).

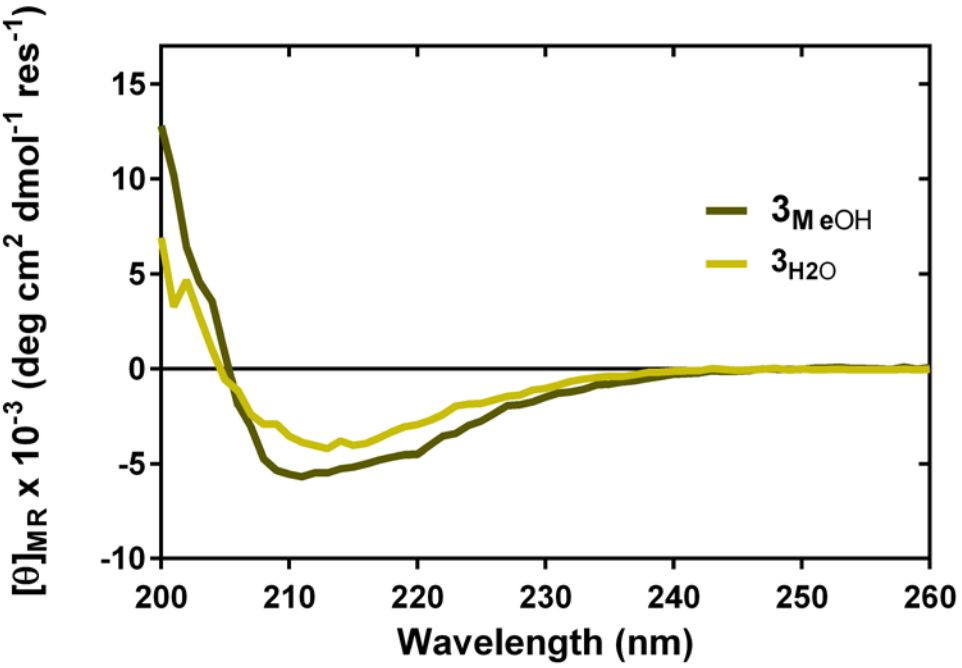

Figure S31. Comparison of CD spectra of peptide **3** in methanol and in 10 mM pH 3.8 acetate buffer (400µM, 5°C).

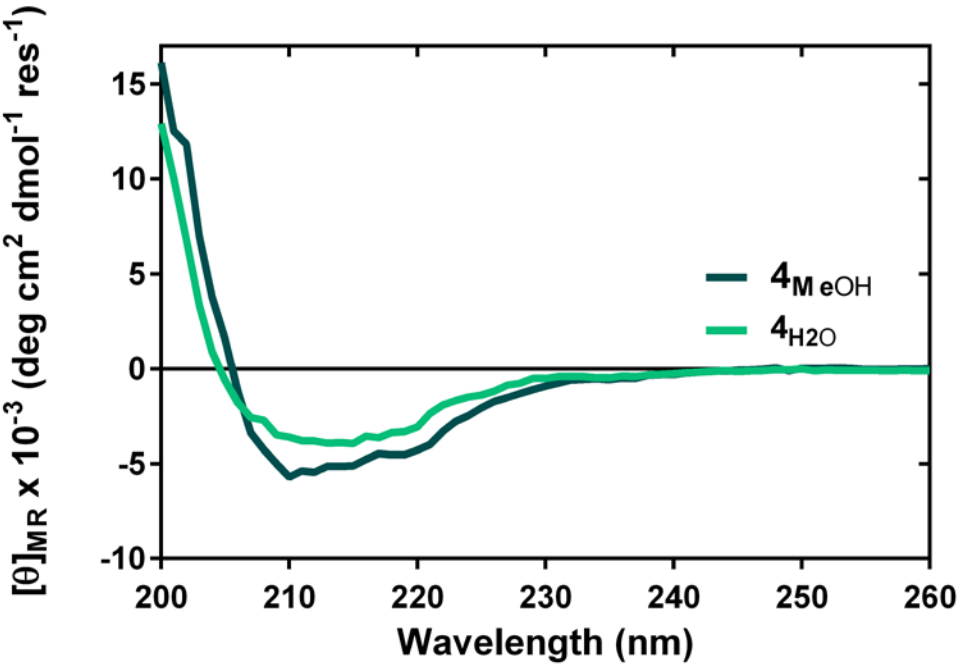

Figure S32. Comparison of CD spectra of peptide **4** in methanol and in 10 mM pH 3.8 acetate buffer (400µM, 5°C).

V. Crystallographic Comparisons

The wealth of crystallographic data for helical foldamers containing acyclic or cyclic γ residues enables a detailed analysis of their residue-level helix parameters: backbone torsions and H-bond geometries. Although there are many foldamer crystal structures containing different kinds of γ residues reported in the literature, this analysis is focused only on the residues matching the backbone substitutions of the residues employed in the main text: acyclic γ^4 residues[S44] and cyclic EtACHA (**Et**hyl **A**mino **C**yclo**H**exane carboxylic **A**cid; **I** in the main text, but we use "EtACHA", used in its seminal publication, to better distinguish it from other typographical marks).[S44j, 45]

A. Torsion Analysis

Comparison of helical torsions: 12-helix vs. 14-helix

"Helical torsions" here is taken to mean more specifically the torsions of all γ^4 or EtACHA residues enclosed within a hydrogen-bonded pseudocycle in the crystallographic structure of an oligopeptide which forms more than one intramolecular hydrogen bond of N→C terminal polarity. This definition does not distinguish among the diverse residue patternings (αγ, ααγ, βγ, etc.), nor does it distinguish among the different hydrogen bonding patterns observed ($i \rightarrow i+2$, $i \rightarrow i+3$, etc.). "H12" torsions are those in γ residues meeting the above criteria and within α/γ-peptide 12-helices with a 1:1 alternating backbone pattern. "H14" torsions are those in γ residues meeting those criteria except within γ-peptide 14-helices. Analysis of helix type is restricted to these two since other helix types have much fewer crystal structures.

The "Ideal H12" torsions used for the γ^4 residues are the torsions for the most stable α/γ-peptide 12-helix identified by Hofmann and coworkers in their computational exploration of the torsional space of unsubstituted α/γ-peptide helices (H_{12}^{I} in their paper).[S46] The "Ideal H14" torsions used for the γ^4 residues are the torsions for the most stable γ-peptide 14-helix in their analogous work with γ-peptide helices (H_{14}^{I}).[S47]

The "Ideal H12" torsions used for EtACHA, on the other hand, were obtained from a geometry-optimized structure of Ac-[Ala][EtACHA][Ala][EtACHA][Ala][EtACHA][Ala][γ^4Ala]-NH_2 (a simplified surrogate for **4** in the main text) at the B3LYP/6-31G(d) level of theory using Gaussian 09.[S48] For the "Ideal H14" torsions for EtACHA, analogous methods were used to obtain the optimized structure of Ac-[EtACHA]$_6$-$NHCH_3$.

Figure S33 compares the torsions of the two different helix types for the two different residue types. The distinguishing torsional change in the conversion from the 12-helical conformation to the 14-helical conformation differs between each residue type. For γ^4, the difference between the mean torsion values of ϕ, θ, and ζ between the helix types were less than 7.0°, while the mean 12-helical ψ value was 22.4° greater than the mean ψ for the 14-helical conformations.

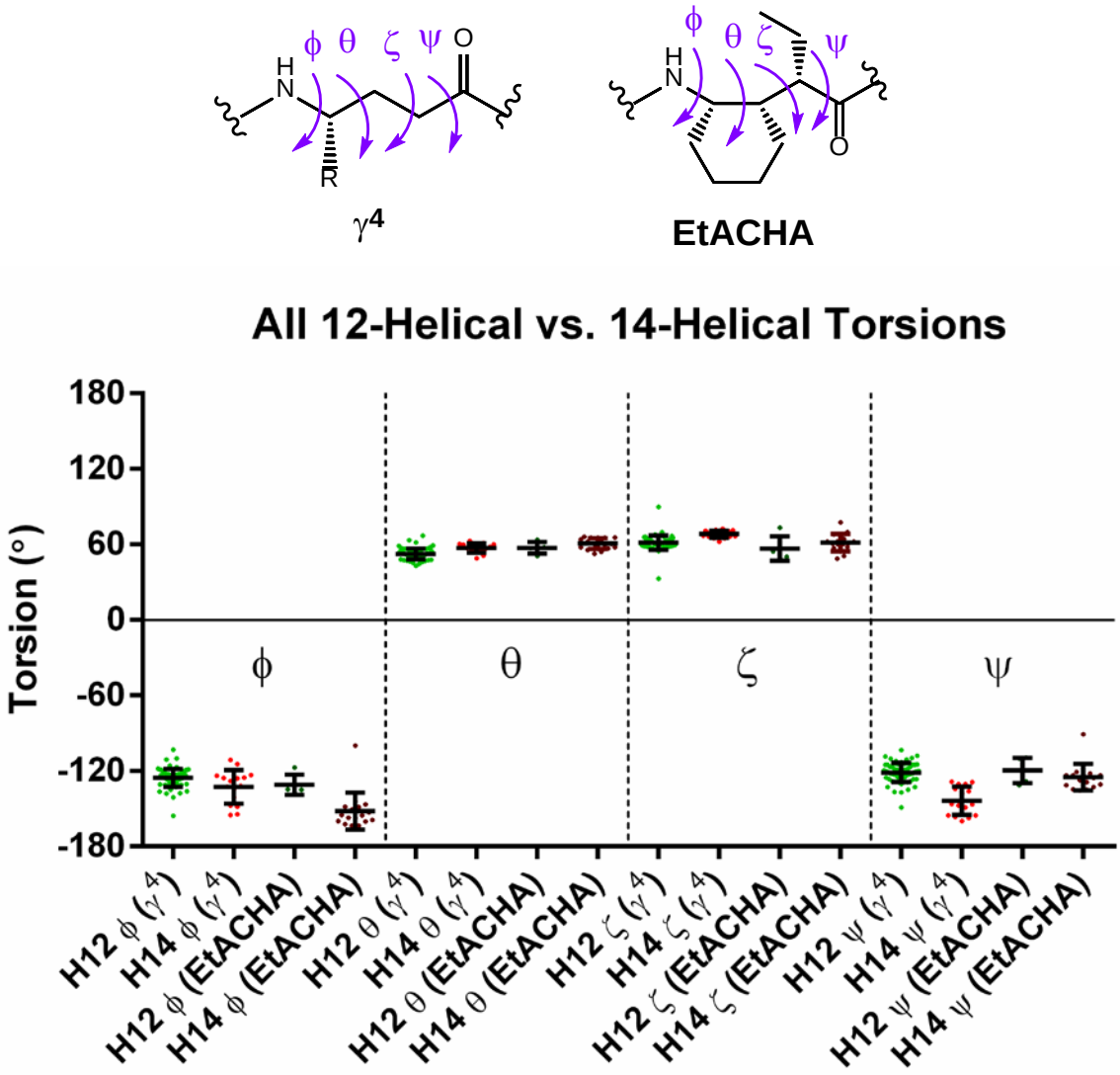

Figure S33: Comparison of the torsion angles of γ^4 and EtACHA residues in different helical forms within the published crystallographic structural data. Definitions of the torsions are given in the structures above. H12: α/γ-peptide 12-helix. H14: γ-peptide 14-helix. Both are characterized by $i \rightarrow i+3$ hydrogen bonds. To facilitate comparison, the torsion values for some residues are inverted to match the chirality of **KACHA** employed in peptides **2**-**4** of the main text.

In contrast, the torsion most controlling the conversion between the 12-helical and 14-helical conformers for EtACHA is ϕ. Although the mean values of θ, ζ, and ψ differ by no more than 5.3° between the two helical forms, the mean of torsion ϕ for the 12-helix is 21.0° greater than the mean ϕ value for the 14-helical form.

Comparison of helical torsions: All helix vs. 12-helix

Figure S34 below offers a broader view of how the helical torsions of the two γ residue types generally differ from those of their respective ideal 12-helices. Each helical torsion of γ^4 and EtACHA are significantly different ($p < 0.05$). The only large difference between them, however, is for ϕ. Torsion ϕ for EtACHA is about 22° more negative than that of γ^4 (γ^4: ϕ =

−126.6 ± 0.7, *n* = 122; EtACHA: ϕ = −144.2 ± 2.1, *n* = 39). This can be explained by the greater number of EtACHA residues available in 14-helical γ-peptide crystal structures (*n* = 17) than 12-helical α/γ-peptide crystal structures (*n* = 5). In contrast, the available crystallographic data for helical γ^4 residues is biased toward α/γ-peptide 12-helices (*n* = 73) and away from the γ-peptide 14-helix (*n* = 16).

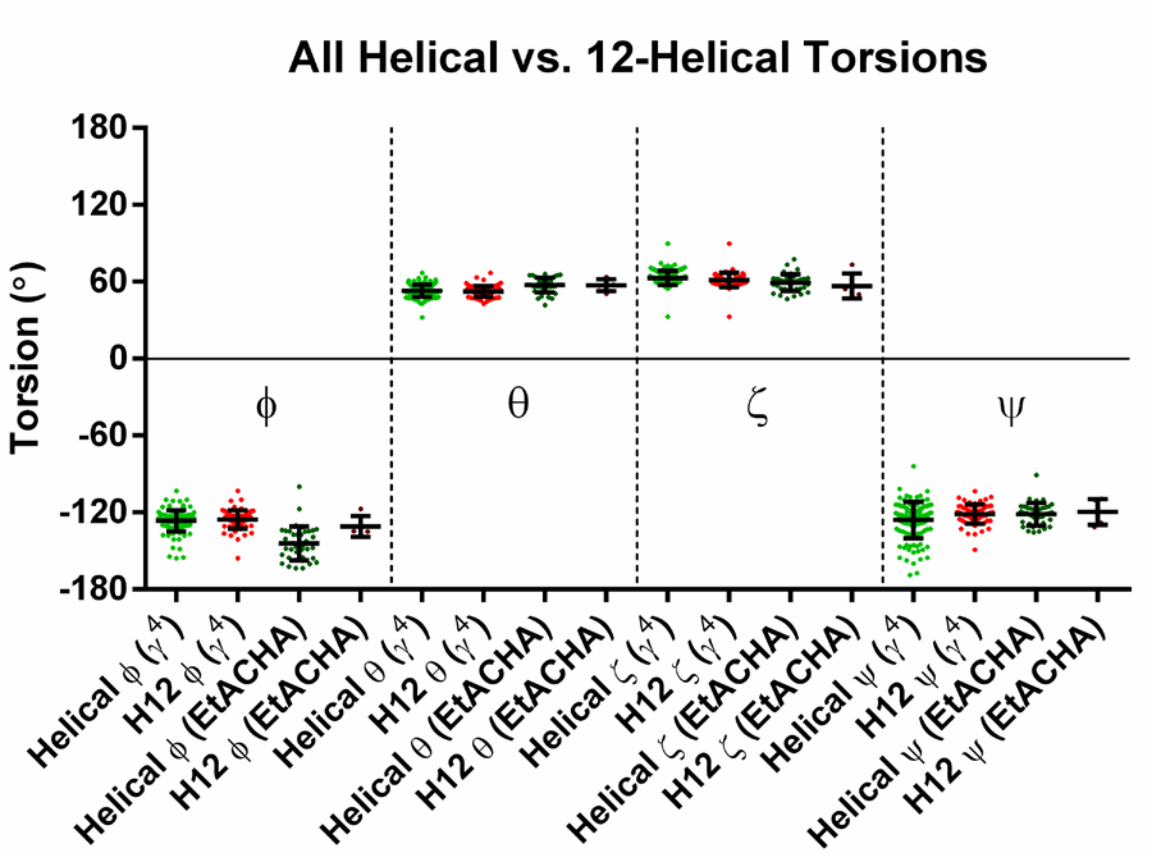

Figure S34: Comparison of all helical torsions (see text for definition) with their 12-helical (H12) values in the published crystallographic structural data for γ^4 residues and EtACHA. To facilitate comparison, the torsion values for some residues are inverted to match the chirality of **KACHA** employed in peptides **2-4** of the main text.

Comparison of helical torsions: Observed vs. ideal

The torsions adopted by helical γ residues in the crystalline state closely resemble their ideal values (**Figures S35** and **S36**). This observation supports the use of computational approaches to predict foldamer helical parameters and aid novel residue design.

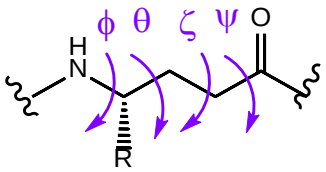

γ4

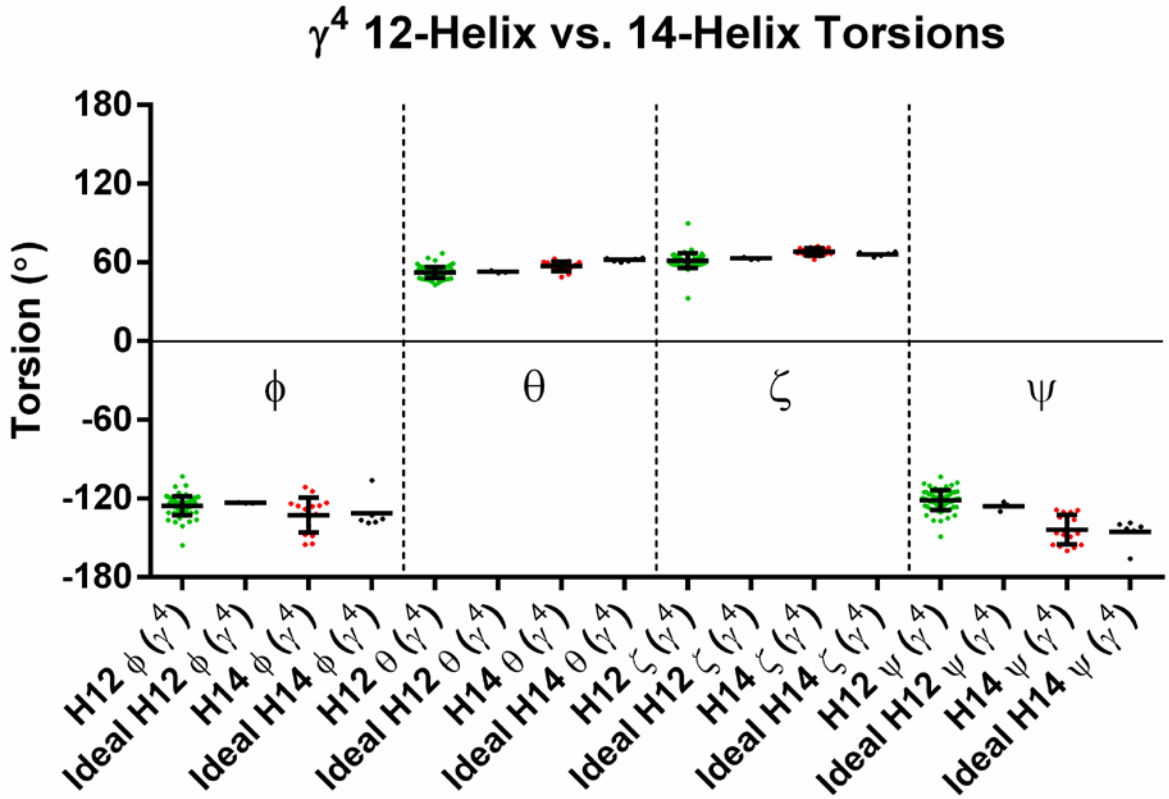

Figure S35: Comparison of 12- and 14-helical torsions within the published crystallographic data for γ^4 residues with their ideal values (see text for definition).

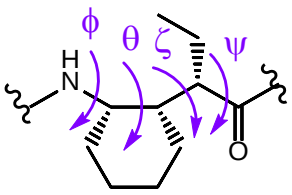

EtACHA

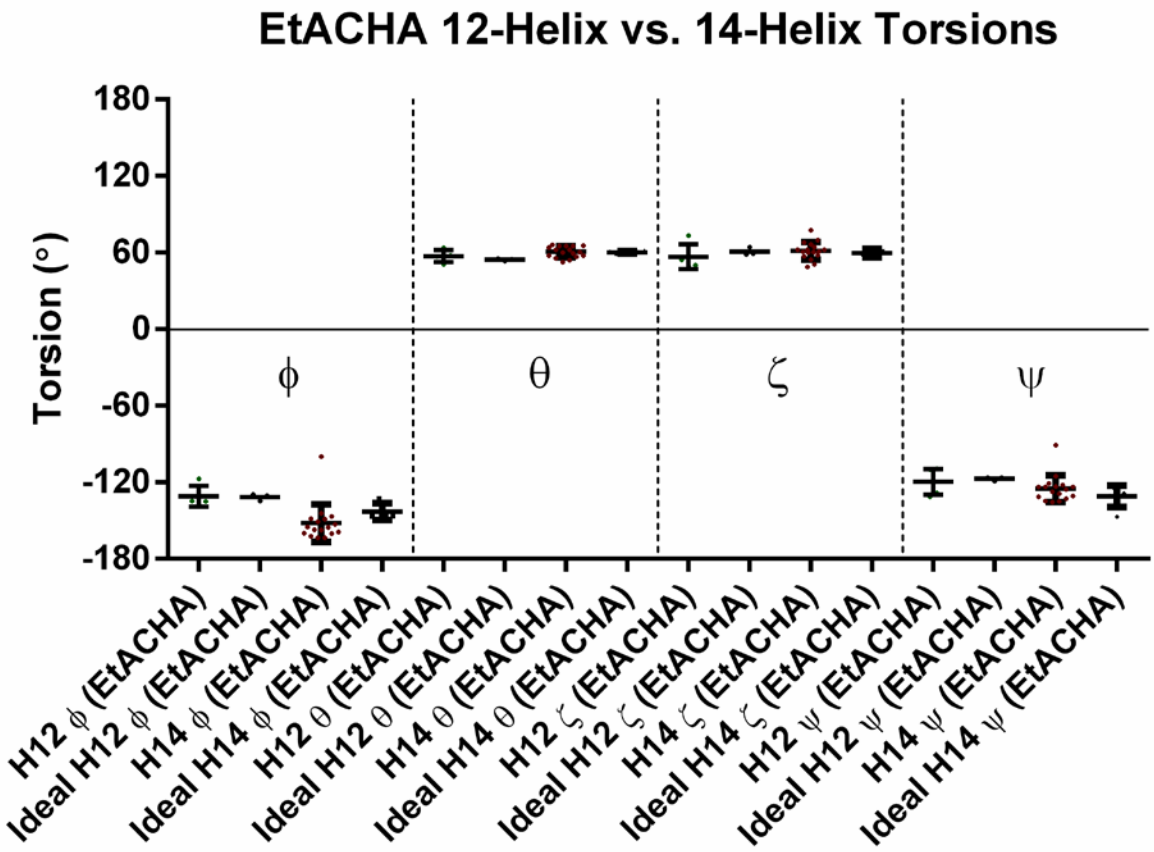

Figure S36: Comparison of 12- and 14-helical torsions within the published crystallographic data for EtACHA residues with their ideal values (see text for definition). To facilitate comparison, the torsion values for some residues are inverted to match the chirality of the **KACHA** residues employed in peptides **2**-**4** of the main text.

Perhaps most revealing of the conformational "personality" of γ^4 residues and EtACHA are the torsions adopted by the residues outside the context of a hydrogen-bonded helix. These residues are either in oligomers too short to adopt intramolecular hydrogen bonds, within irregularly hydrogen-bonded structures, or at the C-termini of more typical hydrogen-bonded helices.

Comparison of helical torsions: Helical vs. non-helical

Figure S37 (and data in tabular form in **Table S27**) below compares the torsions of γ^4 residues that are *not* enclosed within an intramolecular hydrogen bond, i.e. non-helical residues, with the torsions adopted within the α/γ^4-peptide 12-helix and the γ^4-peptide 14-helix. The values of ϕ and

θ for the non-helical residues closely resembles those of the helical torsions, although the means of the two populations of each torsion are significantly different ($p < 0.0001$ for ϕ; $p = 0.0295$ for θ). Both helical and non-helical ϕ and θ tend to prefer $-ac$ ($-90° > \theta > -150°$; see **Figure S38**) and $+sc$ ($30° < \theta < 90°$) values, respectively. Two of 28 non-helical ϕ torsions deviate from the $-ac$ definition into the *ap* definition, compared to 3 of 122 for the helical backbone torsions. Only one non-helical θ torsion is not $+sc$, and there are no non-$+sc$ torsions for the helical γ^4 residues.

Table S27. Comparison of backbone torsion angles in γ^4-residues within helices and not within helices.

Torsion	*n*	Mean torsion (°)	Median torsion (°)	*P* Value (Helix vs. Non-Helix)	% *ap*[a]
ϕ (γ^4 non-helical)	28	−118.0 ± 2.8	−114.4	< 0.0001	7%
Helical ϕ (γ^4)	122	−126.6 ± 0.7	−126.0	*	3%
θ (γ^4 non-helical)	28	59.8 ± 6.4	61.1	0.0295	4%
Helical θ (γ^4)	122	52.8 ± 0.4	52.6	*	0%
ζ (γ^4non-helical)	28	119.4 ± 18.0	166.4	< 0.0001	68%
Helical ζ (γ^4)	122	62.9 ± 0.5	62.5	*	0%
ψ (γ^4non-helical)	27	38.9 ± 26.7	106.3	< 0.0001	52%
Helical ψ (γ^4)	122	−126.0 ± 1.3	−123.2	*	7%

[a]Percent of torsions which are antiperiplanar.

In contrast, the non-helical ζ and ψ backbone torsions tend to adopt *antiperiplanar* torsions instead of the helical $+sc$ and $-ac$, respectively. Both torsions are significantly different between the helical and non-helical populations ($p < 0.0001$). The non-helical ζ torsions are mostly *ap*, with 19 of 28 being *ap* instead of $+sc$. The helical ζ torsions are uniformly $+sc$. For the non-helical ψ, 14 of 27 are *ap* instead of $-ac$ (there are fewer non-helical ψ torsions because multiple conformers about the C_α–C bond in one structure[S44b] precluded assignment of a single ψ). Only 9 of 122 helical ψ adopt *ap* instead of $-ac$ torsions.

Collectively, the torsional data suggest a conformation-constraining role for the sidechain at C_γ, although the solution-phase structural data show that it does not result in an obligatory 12-helical γ residue.

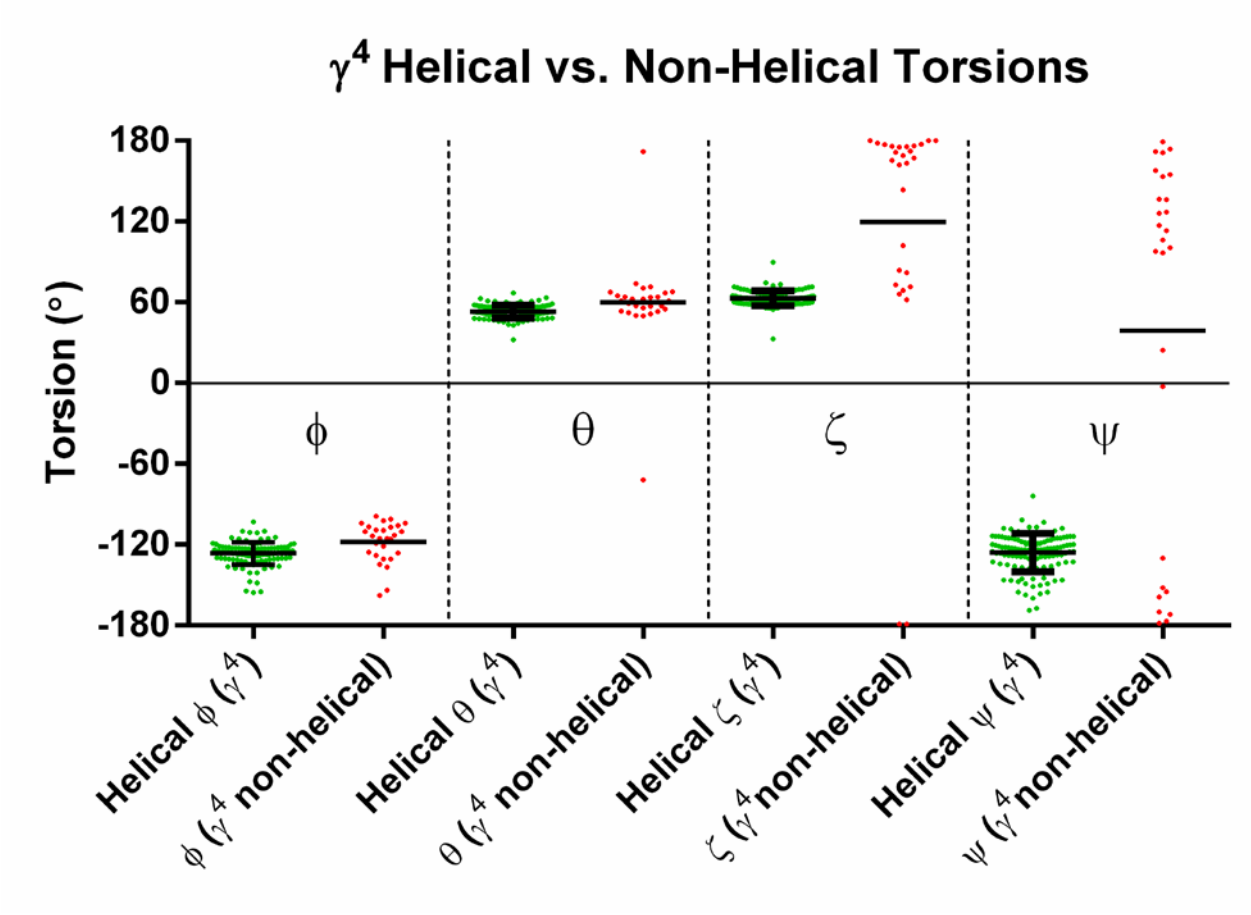

Figure S37: Comparison of helical and non-helical torsions of γ^4 residues within the available crystallographic structural data.

Completing the picture, much less backbone torsional variance is observed for EtACHA between its helical and non-helical forms (**Figure S39** and **Table S28**). The means of only one backbone torsion, ψ, differs significantly between its helical and non-helical form (p = 0.0018). Due to the more negative value of ϕ observed in the over-represented 14-helix, the ϕ torsions prefer values very close to the nominal barrier between *–ac* and *ap*, with 13 of 39 helical ϕ and 2 of 11 non-helical ϕ classified as *ap*. The ring constraining θ ensures no exit from the *+sc* category no matter the helical context. Torsion ζ, which is not ring-constrained, nevertheless appears to be constrained to the *+sc* category independent of context. Torsion ψ as well appears well constrained by the nearby ethyl group to adopt *–ac* torsions, although a single non-helical ψ barely makes it into the *ap* bin (1 of 11; $\psi = -150.3$). The mean helical ψ is greater than the mean non-helical ψ by about 11.5°. The non-helical ψ thus lies nearer the optimal γ-peptide 14-helix value than the α/γ-peptide 12-helix value.

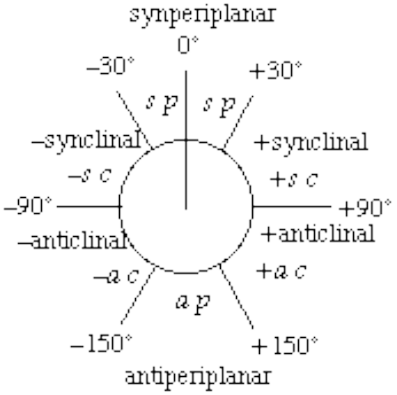

Figure S38. Definitions of torsion angle classes used here. From *http://www.chem.qmul.ac.uk/iupac/stereo/TZ.html*

Table S28. Comparison of backbone torsion angles in EtACHA-residues within helices and not within helices.

Torsion	*n*	Mean torsion (°)	Median torsion (°)	*P* Value (Helix vs. Non-Helix)	% *ap*[a]
ϕ (EtACHA non-helical)	11	−137.1 ± 5.6	−138.6	0.1593	18%
Helical ϕ (EtACHA)	39	−144.2 ± 2.1	−145.8		33%
θ (EtACHA non-helical)	11	56.0 ± 0.7	55.6	0.4075	0%
Helical θ (EtACHA)	39	57.4 ± 0.9	57.8		0%
ζ (EtACHA non-helical)	11	55.1 ± 2.4	55.8	0.0769	0%
Helical ζ (EtACHA)	39	59.3 ± 1.1	60.2		0%
ψ (EtACHA non-helical)	11	−132.9 ± 4.3	−140.5	0.0018	9%
Helical ψ (EtACHA)	39	−121.5 ± 1.4	−120.8	*	0%

[a]Percent of torsions which are antiperiplanar.

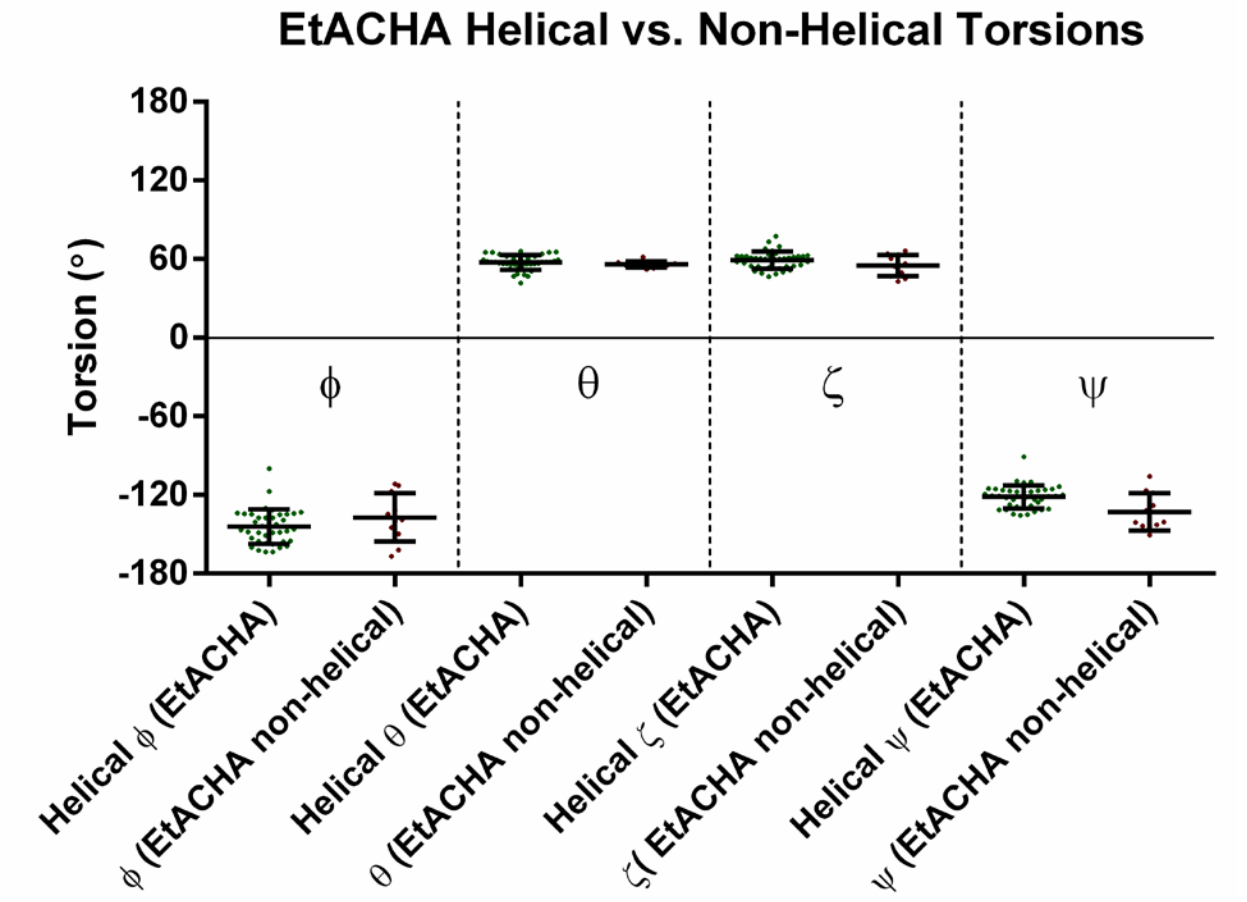

Figure S39: Comparison of helical and non-helical torsions of EtACHA residues within the available crystallographic structural data. To facilitate comparison, the torsion values for some residues are inverted to match the chirality of the **KACHA** residues employed in peptides **2-4** of the main text.

B. Hydrogen Bond Parameter Analysis

γ^4 vs. EtACHA Hydrogen Bond Parameters

Finally, we can analyze hydrogen bonding geometries in the crystallographic data for α/γ-peptide 12-helices to search for hints of conformational fragility in either γ^4 residues or EtACHA residues. The large crystallographic dataset of 12-helical α/γ^4-peptides does lend itself to some statistical analysis. The three geometric parameters we focus on are: 1) Distance of H-bond donor heavy atom (i.e., D···A, where D=amide nitrogen and A=acceptor carbonyl oxygen) to H-bond acceptor; 2) Angle C=O···H; 3) Angle O···H−N. For H-bond distance D···A, ideal values are smaller;[S49] for angle C=O···H, ideal values are about 135°;[S50] for O···H−N, ideal values are 180°.[S51]

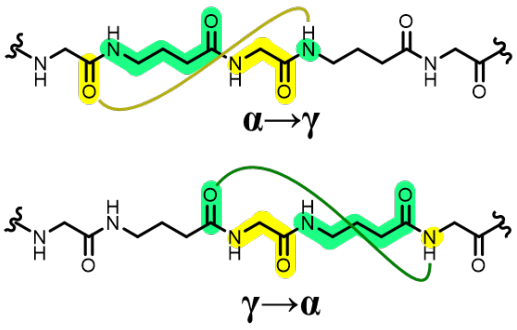

Figure S40. Hydrogen bond types within α/γ-peptide 12-helices.

The H-bonds of peptide foldamer helices with 1:1 alternating heterogeneous backbones are formed by two different donor-acceptor residue pair types. α/γ-Peptide 12-helices are defined by 12-membered C=O(α,*i*)→H−N(γ,*i*+3) alternating with 12-membered C=O(γ,*i*)→H−N(γ,*i*+3) hydrogen bonds (**Figure S40**). Although each type contains the same number of atoms is enclosed within each type of pseudocycle, the order in which the atom types are encountered as one counts along the ring differ, and the donor and acceptor groups belong to different residue types. Thus, we should expect to see some differentiation in the H-bond types.

Figure S41 compares the distribution of H-bond parameters of α/γ^4-peptides with those of α/EtACHA peptides. Unfortunately, the small number of reported 12-helical α/EtACHA peptides means that meaningful statistical analysis of their preferred H-bond geometries is not possible. Nevertheless, the available data are presented here. A clear picture of the relative strengths of H-bonds within α/γ^4-peptide and α/EtACHA-peptide helices does not emerge from the available crystallographic data. For each H-bond parameter, the means do not significantly differ between the peptides containing either residue type.

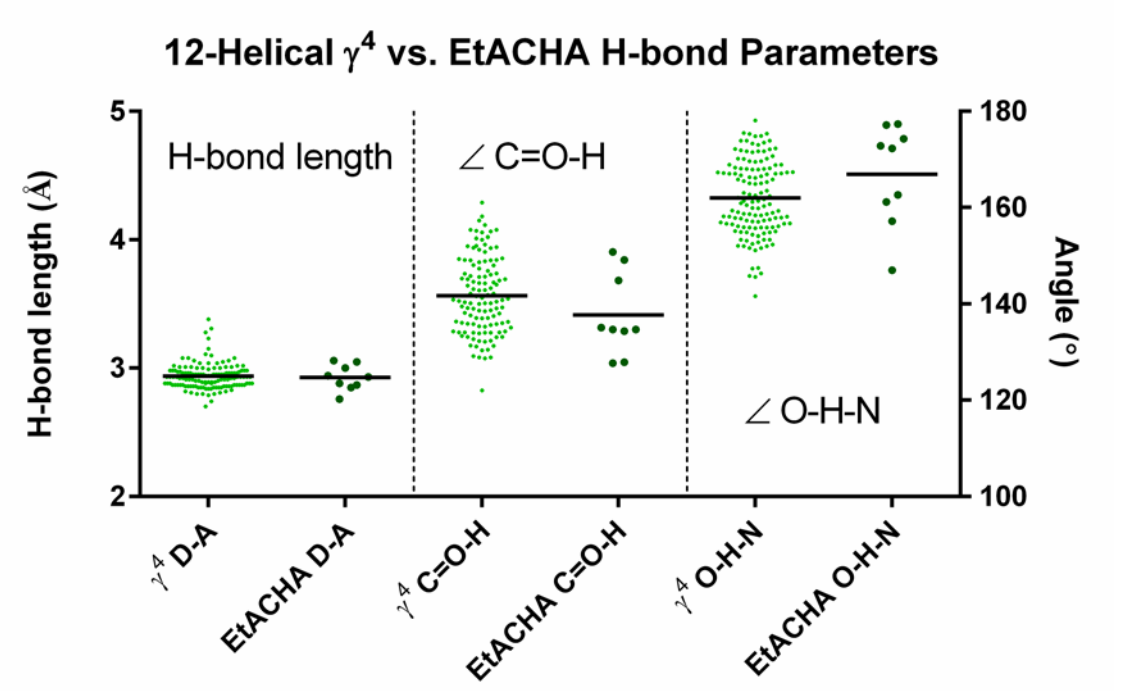

Figure S41. Comparison of hydrogen bond parameters for α/γ^4 and α/EtACHA-peptide helices. Each point marks an individual H-bond in the available crystallographic data, and horizontal bars mark mean values. From left to right: H-bond length (Å, left y-axis); angle C=O···H (°, right y-axis); angle O···H−N (°, right y-axis)

γ^4 Hydrogen Bond Parameter Analysis: α→γ^4 vs. γ^4→α

The greater number of α/γ^4-peptide crystal structures gives us the opportunity to examine the relative H-bond strengths of the two types of H-bonds (*vide supra*) inherent in helical peptide foldamers with alternating backbone types (**Figure S42**). The broad distribution of H-bond parameters observed in *all* H-bond types within α/γ^4-peptide helices can be seen to be the sum of two separate narrower, different H-bond parameter distributions for each type of parameter. The data show the different ways in which the different H-bond types form their geometries. The γ^4→α H-bond angles adopt more positive values than the γ^4→α H-bond angles. The less-constrained ψ torsion of the γ^4 residues appear to be better able to tilt the carbonyl C=O bond to be more parallel with the direction of the helix axis, leading to more linear H-bonds than the more crowded ψ torsions of the α residues are able to achieve.

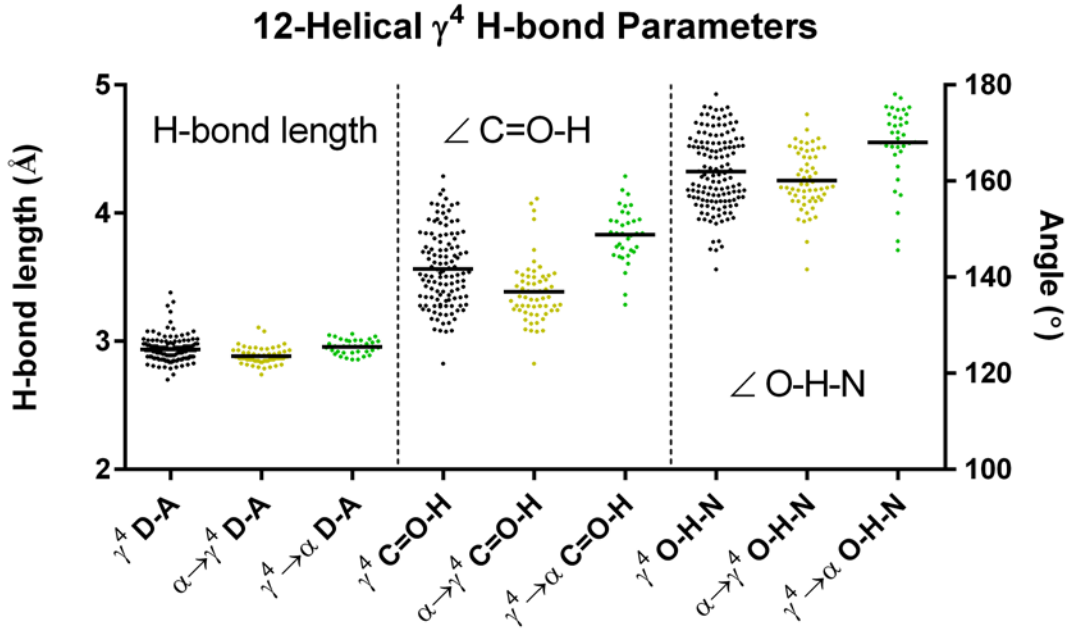

Figure S42. Comparison of hydrogen bond parameters for all α/γ-peptide 12-helix H-bond types and separated into α→γ^4 and γ^4→α H-bonds. Each point marks an individual H-bond in the available crystallographic data, and horizontal bars mark mean values. From left to right: H-bond length (Å, left y-axis); angle C=O···H (°, right y-axis); angle O···H–N (°, right y-axis)

The α→γ^4 H-bond distances are significantly shorter than the γ^4→α H-bond distances (p < 0.0001). The factors responsible for this are not entirely clear. However, given that two of the three H-bond parameters for α→γ^4 H-bonds are closer to ideal than γ^4→α H-bonds, one might speculate that this means that α→γ^4 H-bonds are the stronger of the two. In fact, other observations within the crystallographic data for α/γ-peptides lend support to this. Most strikingly, the crystal structure of one α/γ^4-peptide decamer features solvent interpolated into two if its intramolecular H-bonds, each of which is of the γ^4→α type (**Figure S43**).[S44l] Previous studies in our lab have found that consistent solvent interpolation of a particular H-bond type in peptide foldamer helices with heterogeneous backbones can reflect lesser stability of that hydrogen bond type.[S34] The authors have also found 9-membered i→i+2 hydrogen bonded rings involving the γ^4 C=O (and disrupting the γ^4→α 12-helix H-bond) appear frequently in molecular dynamics simulations of α/γ^4-peptides (unpublished). Collectively, the crystallographic and computational data encourage further study on the differences in stability of the two H-bond types.

A few caveats should be noted in the above interpretations. First, the available crystallographic data set for the two residue types is not large. Although there tends to be a significant correlation between the observed conformer distribution of a particular molecular substructure (i.e. torsion angles, hydrogen bonding geometry, etc.) and the computationally-determined energies of the torsions,[S52] the types of studies characterizing this trend draw from much larger data sets, such as the CSD or PDB. Second, these larger data sets additionally contain more diverse molecular structures which contain the molecular substructures. The γ^4 and EtACHA torsions are almost exclusively contained within relatively homogeneous helical structures. Most non-helical examples of each residue lie at helix termini, at which intermolecular interactions such as H-bonding are common within the data set. The additional torsional freedom of γ^4 residues vs. EtACHA residues could reflect only the greater flexibility of the residue at helical termini within a crystalline lattice, rather than greater flexibility generally within a polypeptide in the solution state. Given that the solution phase data, however, indicate a greater flexibility of γ^4 residues than EtACHA in solution, we are inclined to interpret the crystallographic data as reliable.

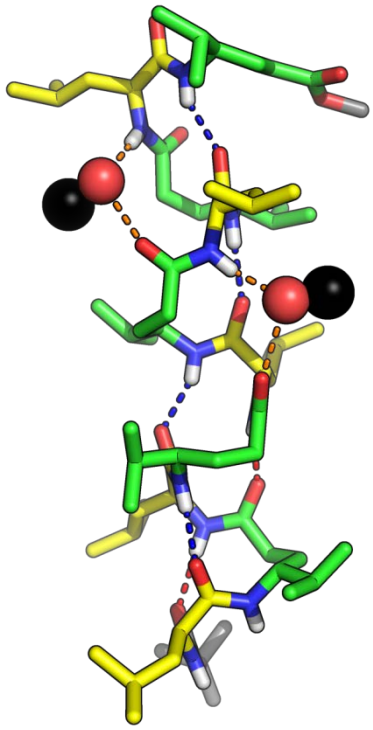

In summary, the available crystallographic data support the paper's conclusions that the EtACHA backbone is pre-organized toward forming the α/γ-peptide 12-helix, whereas γ^4 residues show clearer signs of fragility, particularly in their ζ and ψ torsions and their H-bond parameters, which prevent them from adopting 12-helical torsions as readily.

Figure S43. Crystal structure of 12-helical α/γ^4-decapeptide **1** reported by Balaram and coworkers.[S44l] CH_3OH solvent interpolation is shown as space-filling spheres.

VI. Peptide Synthesis

A. UPLC Chromatograms

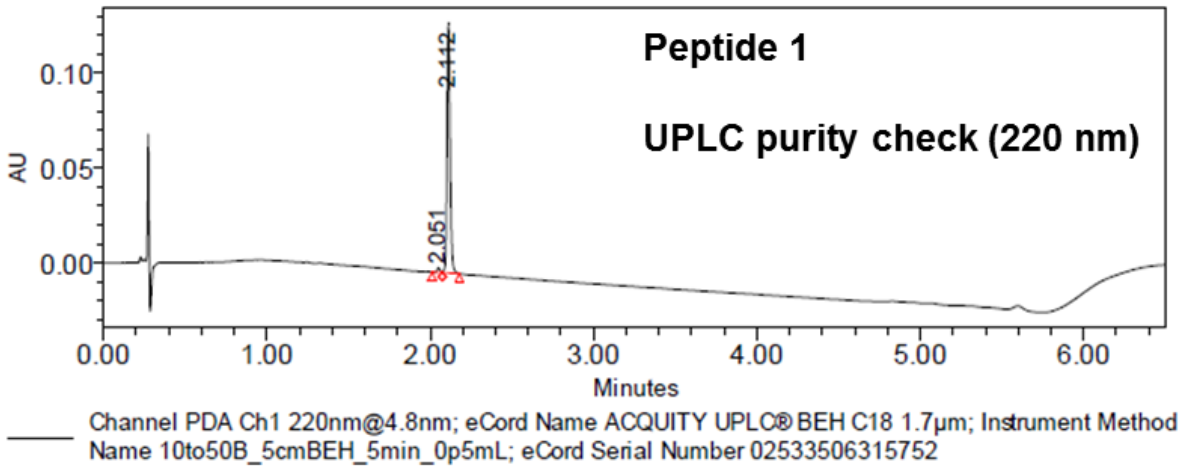

Channel PDA Ch1 220nm@4.8nm; eCord Name ACQUITY UPLC® BEH C18 1.7µm; Instrument Method Name 10to50B_5cmBEH_5min_0p5mL; eCord Serial Number 02533506315752

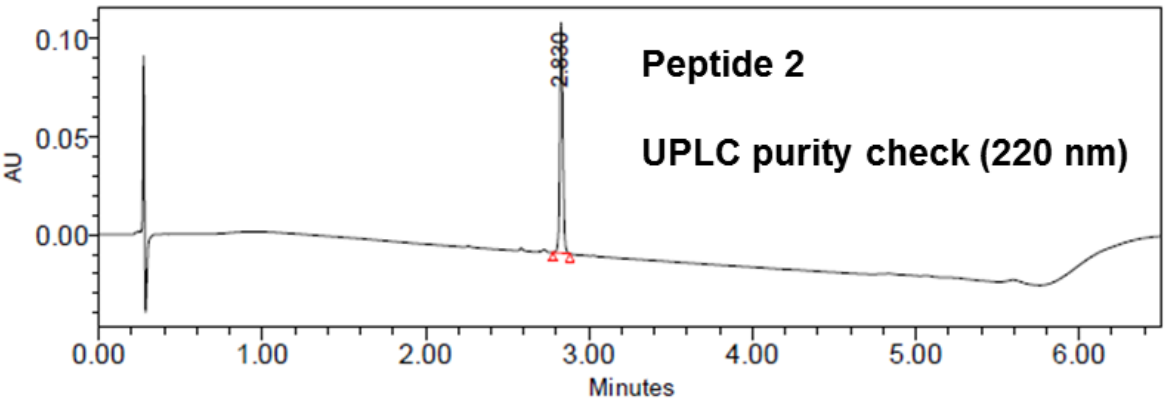

Channel PDA Ch1 220nm@4.8nm; eCord Name ACQUITY UPLC® BEH C18 1.7µm; Instrument Method Name 10to50B_5cmBEH_5min_0p5mL; eCord Serial Number 02533506315752

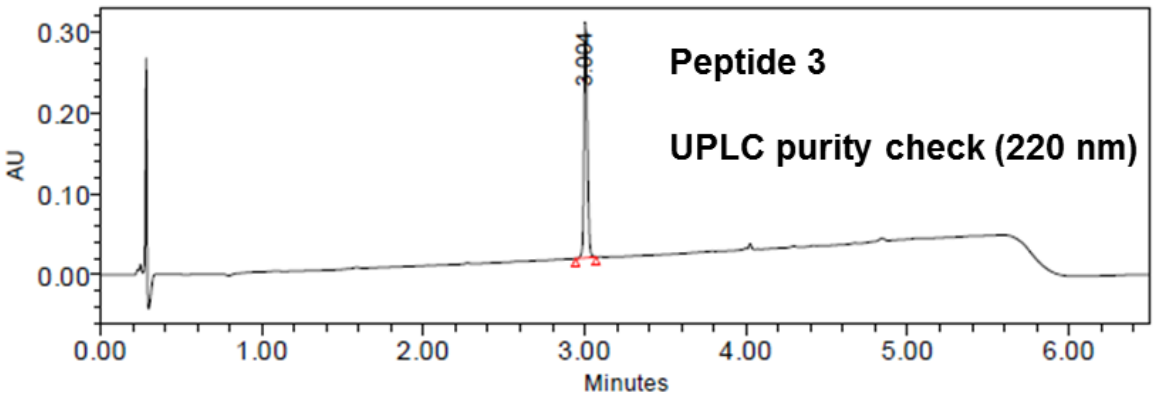

Channel PDA Ch1 220nm@4.8nm; eCord Name ACQUITY UPLC® BEH C18 1.7µm; Instrument Method Name 10to50B_5cmBEH_5min_0p5mL; eCord Serial Number 02533506315752

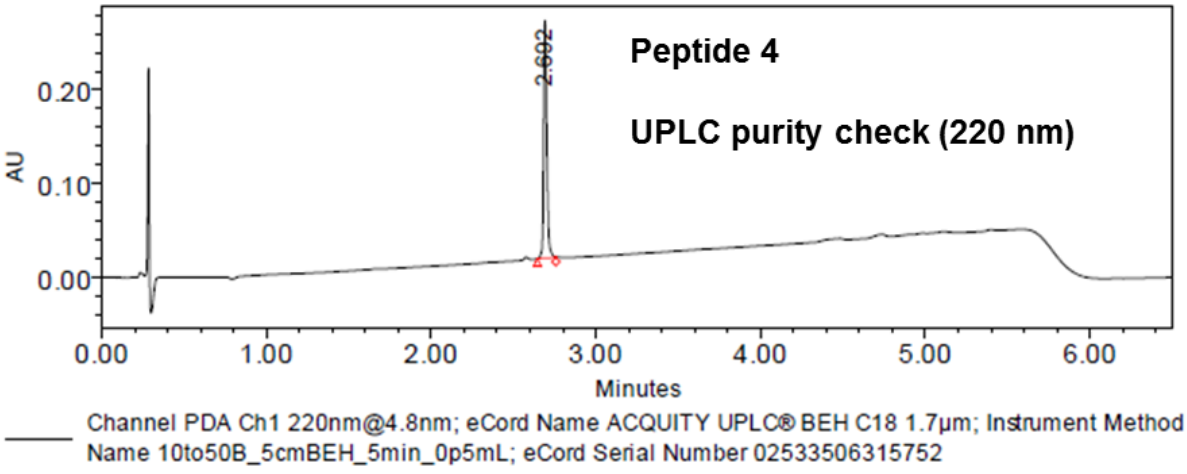

Channel PDA Ch1 220nm@4.8nm; eCord Name ACQUITY UPLC® BEH C18 1.7µm; Instrument Method Name 10to50B_5cmBEH_5min_0p5mL; eCord Serial Number 02533506315752

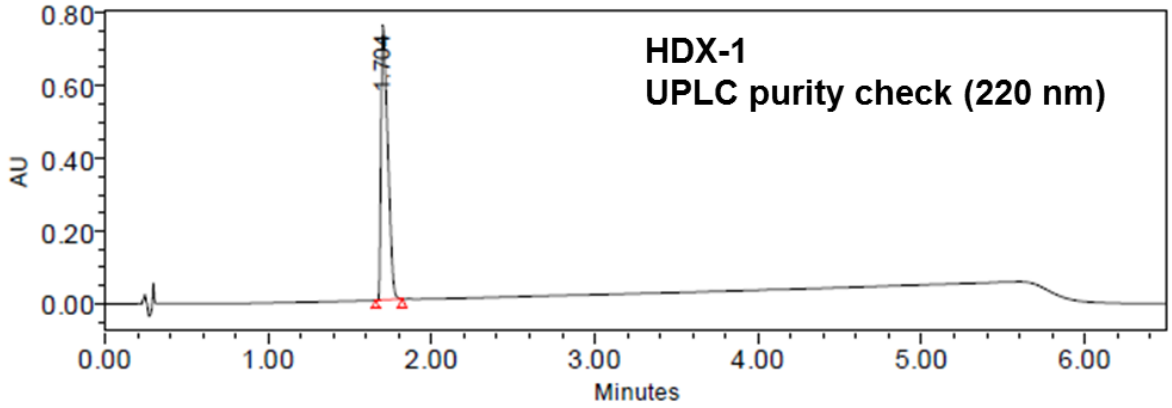

Channel PDA Ch1 220nm@4.8nm; eCord Name ACQUITY UPLC® BEH C18 1.7µm; Instrument Method Name 10to50B_5cmBEH_5min_0p5mL; eCord Serial Number 02533506315752

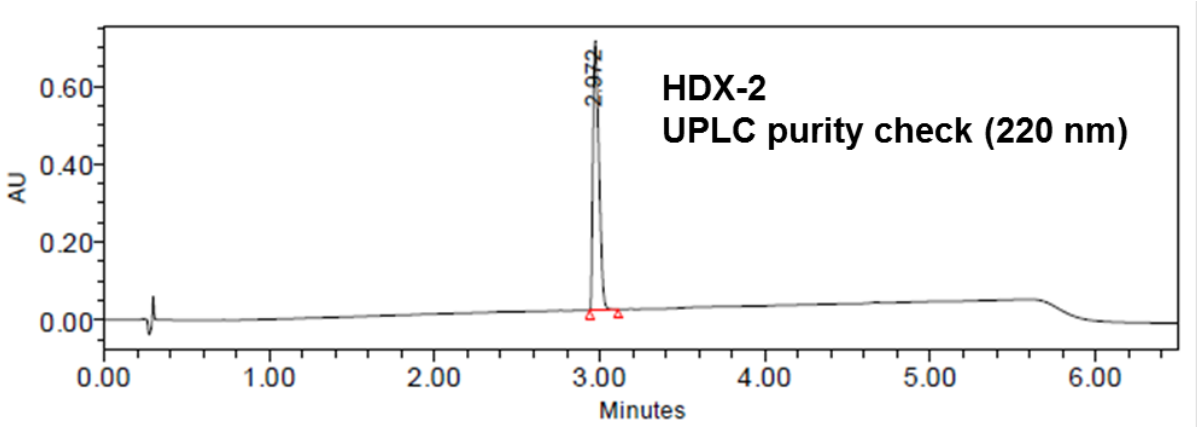

Channel PDA Ch1 220nm@4.8nm; eCord Name ACQUITY UPLC® BEH C18 1.7µm; Instrument Method Name 10to50B_5cmBEH_5min_0p5mL; eCord Serial Number 02533506315752

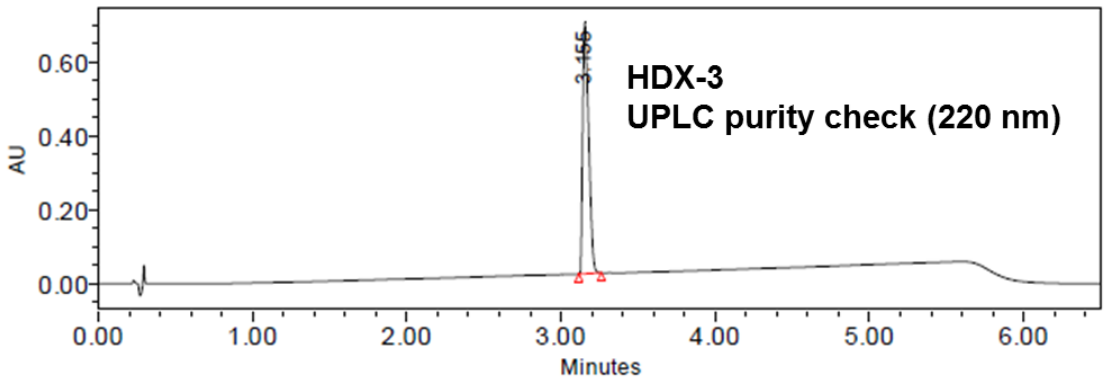

Channel PDA Ch1 220nm@4.8nm; eCord Name ACQUITY UPLC® BEH C18 1.7µm; Instrument Method Name 10to50B_5cmBEH_5min_0p5mL; eCord Serial Number 02533506315752

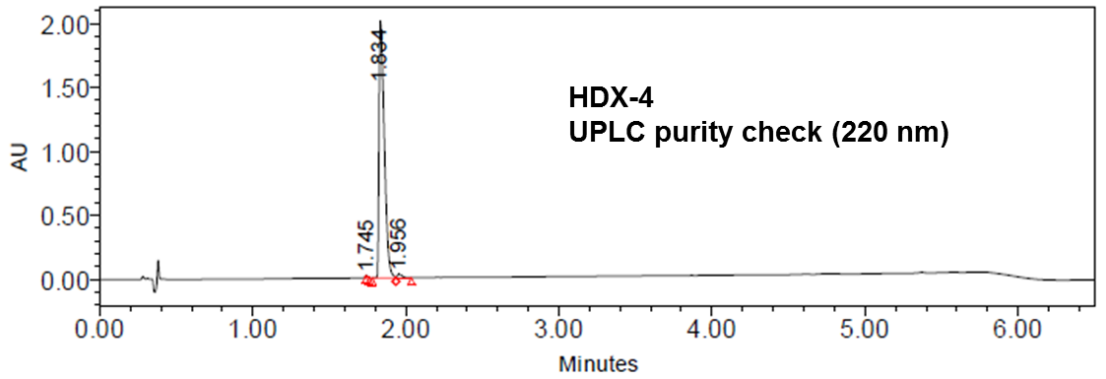

Channel PDA Ch1 220nm@4.8nm; eCord Name ACQUITY UPLC® BEH C18 1.7µm; Instrument Method Name 10to50B_5min_0p4mL; eCord Serial Number 02533506315752

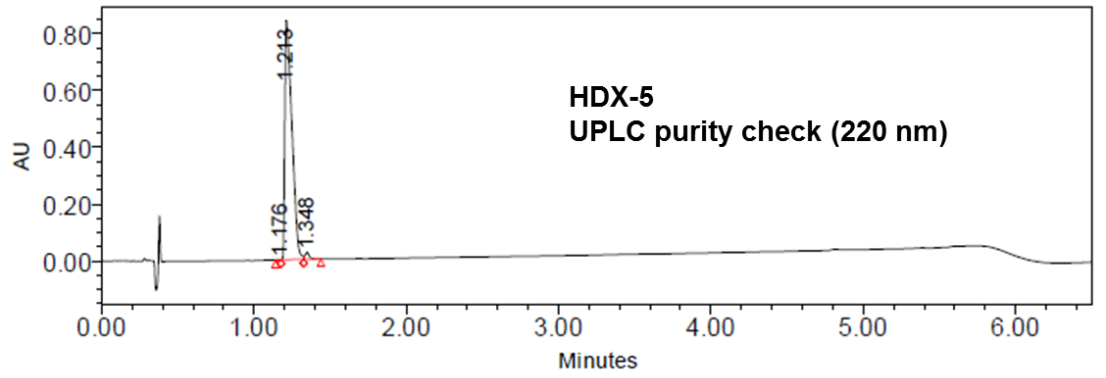

Channel PDA Ch1 220nm@4.8nm; eCord Name ACQUITY UPLC® BEH C18 1.7µm; Instrument Method Name 10to50B_5min_0p4mL; eCord Serial Number 02533506315752

B. MALDI

U:\Fisher\151031x03\0_C17\1\1SRef

Comment 1 BFF6-114B // CHCA // RP_PepMix printed: 10/31/2015 4:58:55 PM
Comment 2 150 shots, 20% (72%), 120-3640

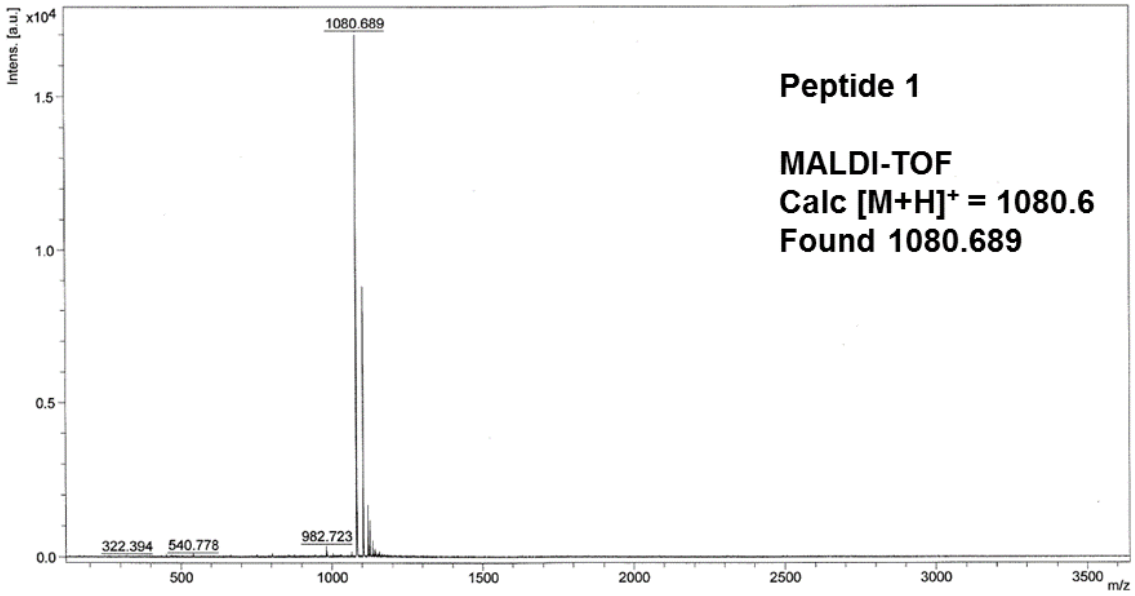

Peptide 1

MALDI-TOF
Calc $[M+H]^+$ = 1080.6
Found 1080.689

Bruker Ultraflex III, Chemical Instrumentation Center, University of Wisconsin-Madison, Cite NIH 1S10RR024601-01

U:\Fisher\151031x04\0_C18\1\1SRef

Comment 1 BFF6-114C // CHCA // RP_PepMix printed: 10/31/2015 4:59:08 PM
Comment 2 150 shots, 20% (72%), 120-3640

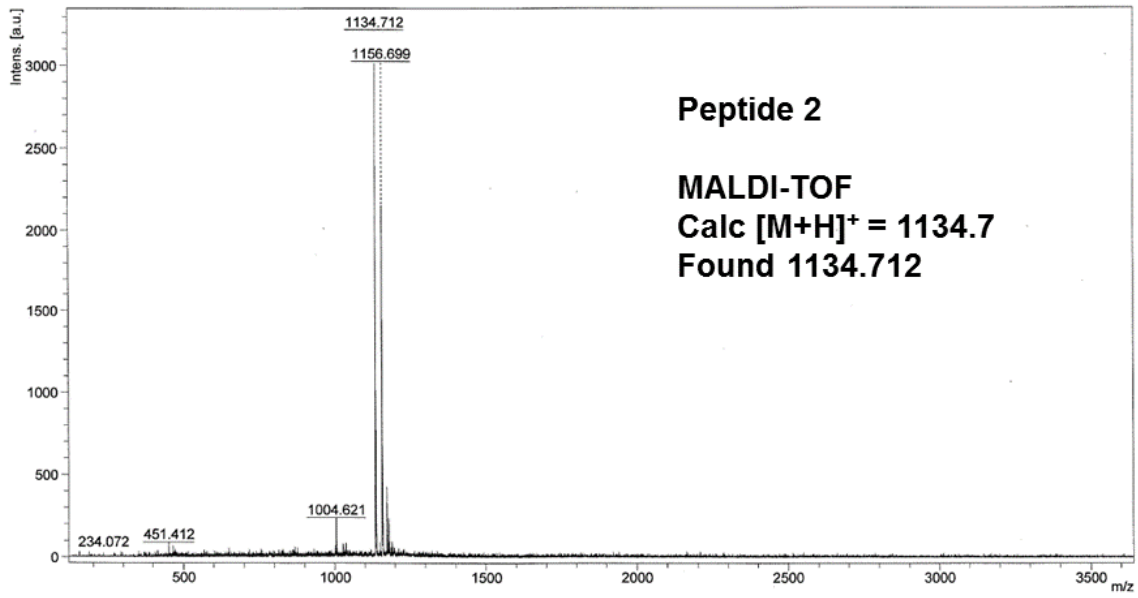

Peptide 2

MALDI-TOF
Calc $[M+H]^+$ = 1134.7
Found 1134.712

Bruker Ultraflex III, Chemical Instrumentation Center, University of Wisconsin-Madison, Cite NIH 1S10RR024601-01

D:\Data\Fisher\151214x01\0_H19\1\1SRef

Comment 1 BFF6-185 // CHCA // RP_PepMix
Comment 2 400 shots, 20% (72%), 0-5080

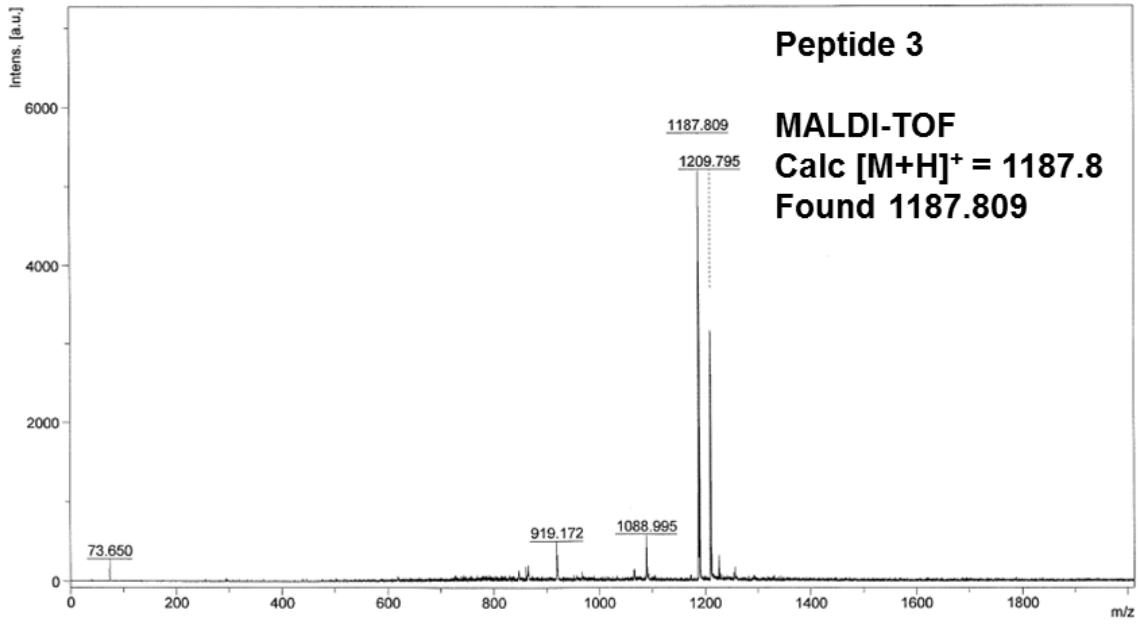

Peptide 3

MALDI-TOF
Calc [M+H]$^+$ = 1187.8
Found 1187.809

Bruker Ultraflex III, Chemical Instrumentation Center, University of Wisconsin-Madison, Cite: NIH NCRR 1S10RR024601-01 printed: 12/14/2015 10:37:04 AM

U:\Fisher\151208x02\0_H9\1\1SRef

Comment 1 BFF6-176_v8 // CHCA // RP_PepMix
Comment 2 200 shots, 50% Ip (72%), 120-3600

printed: 12/8/2015 7:19:44 PM

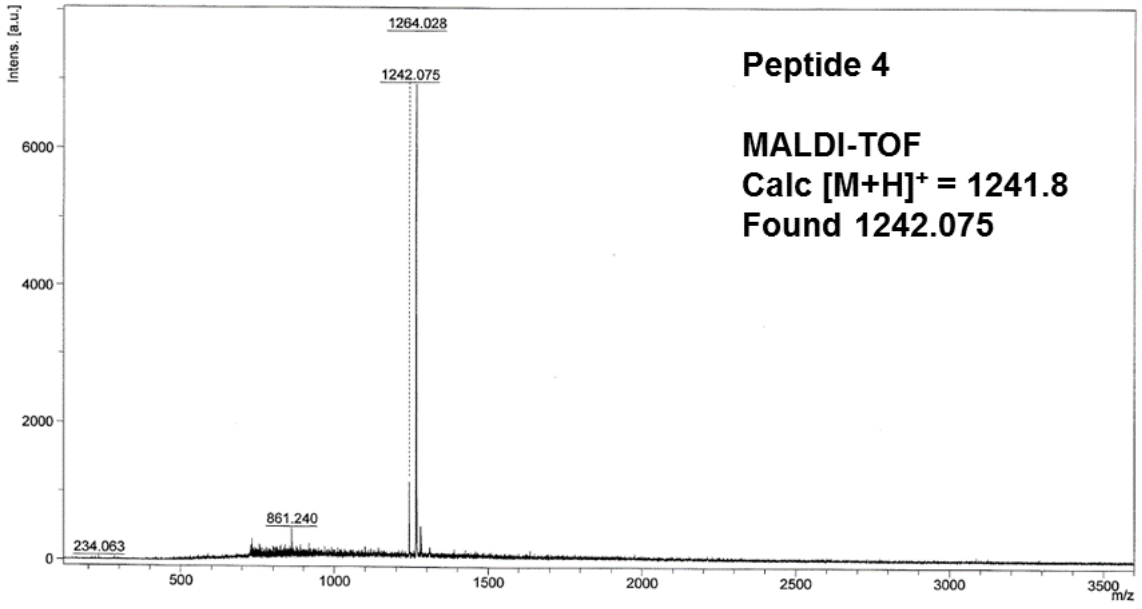

Peptide 4

MALDI-TOF
Calc [M+H]$^+$ = 1241.8
Found 1242.075

Bruker Ultraflex III, Chemical Instrumentation Center, University of Wisconsin-Madison, Cite NIH 1S10RR024601-01

VII. NMR Spectra

A. ^{1}H-NMR Spectra

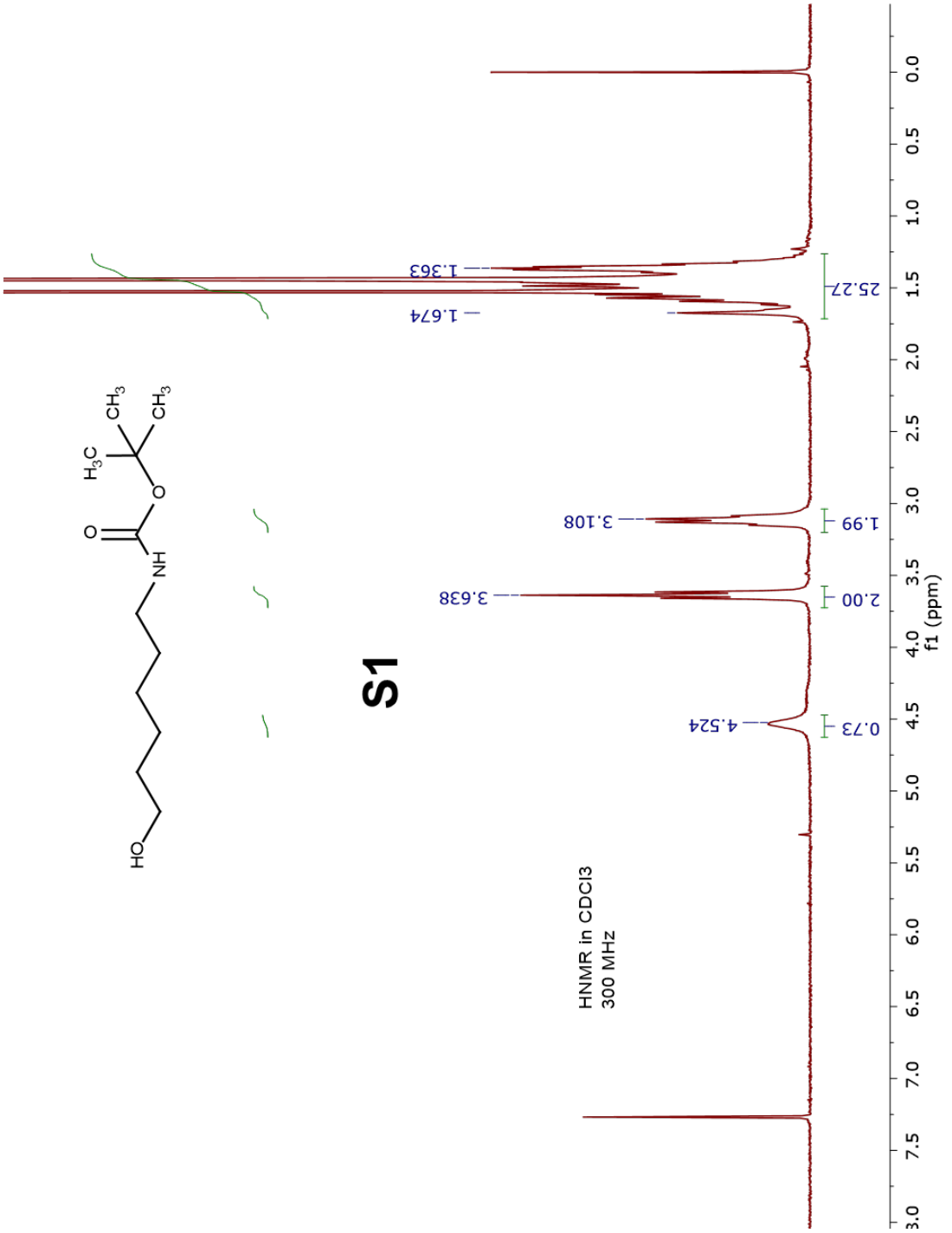

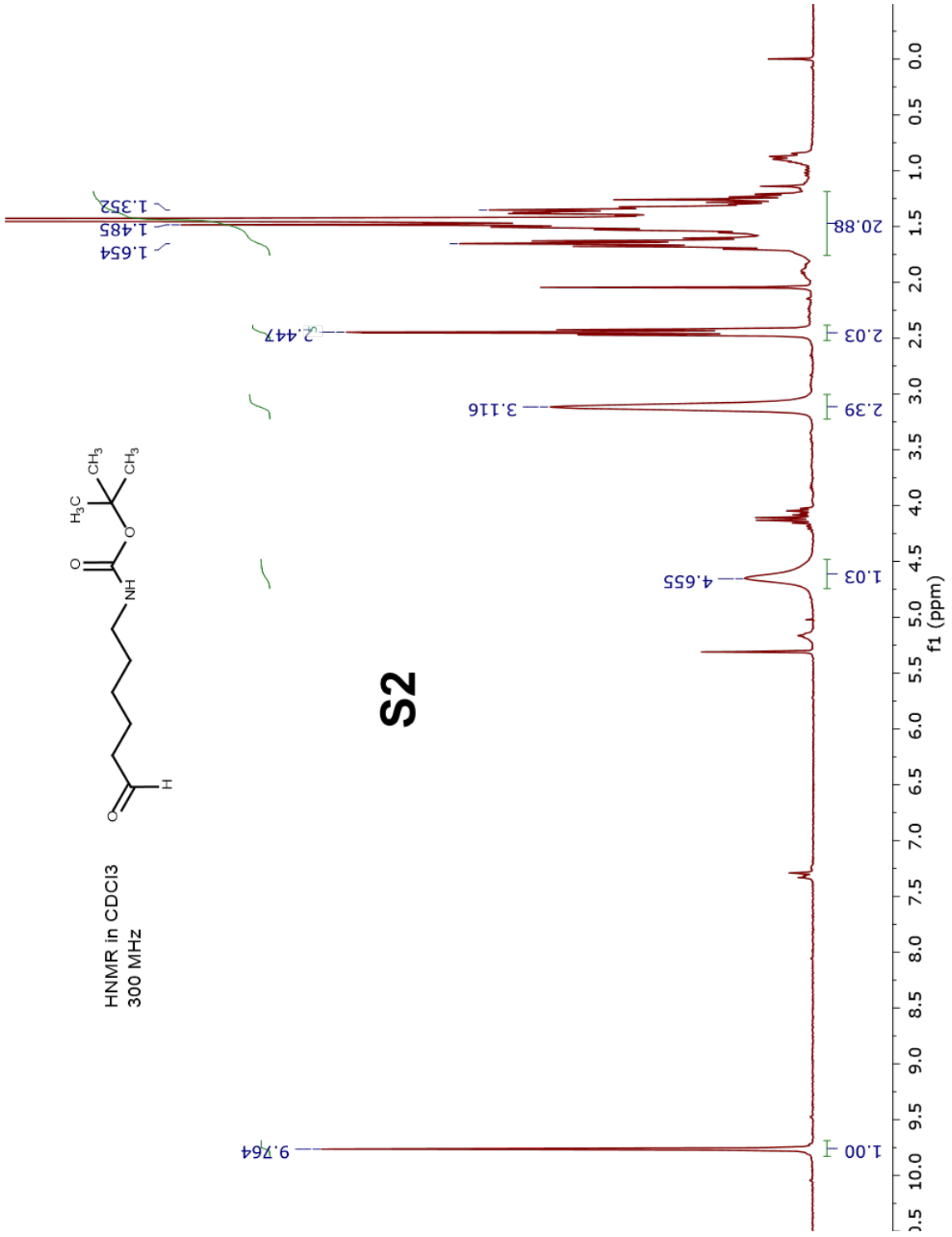
HNMR in CDCl3
300 MHz
S2
9.764
4.655
3.116
2.447
1.654
1.485
1.352
1.00
1.03
2.39
2.03
20.88
f1 (ppm)

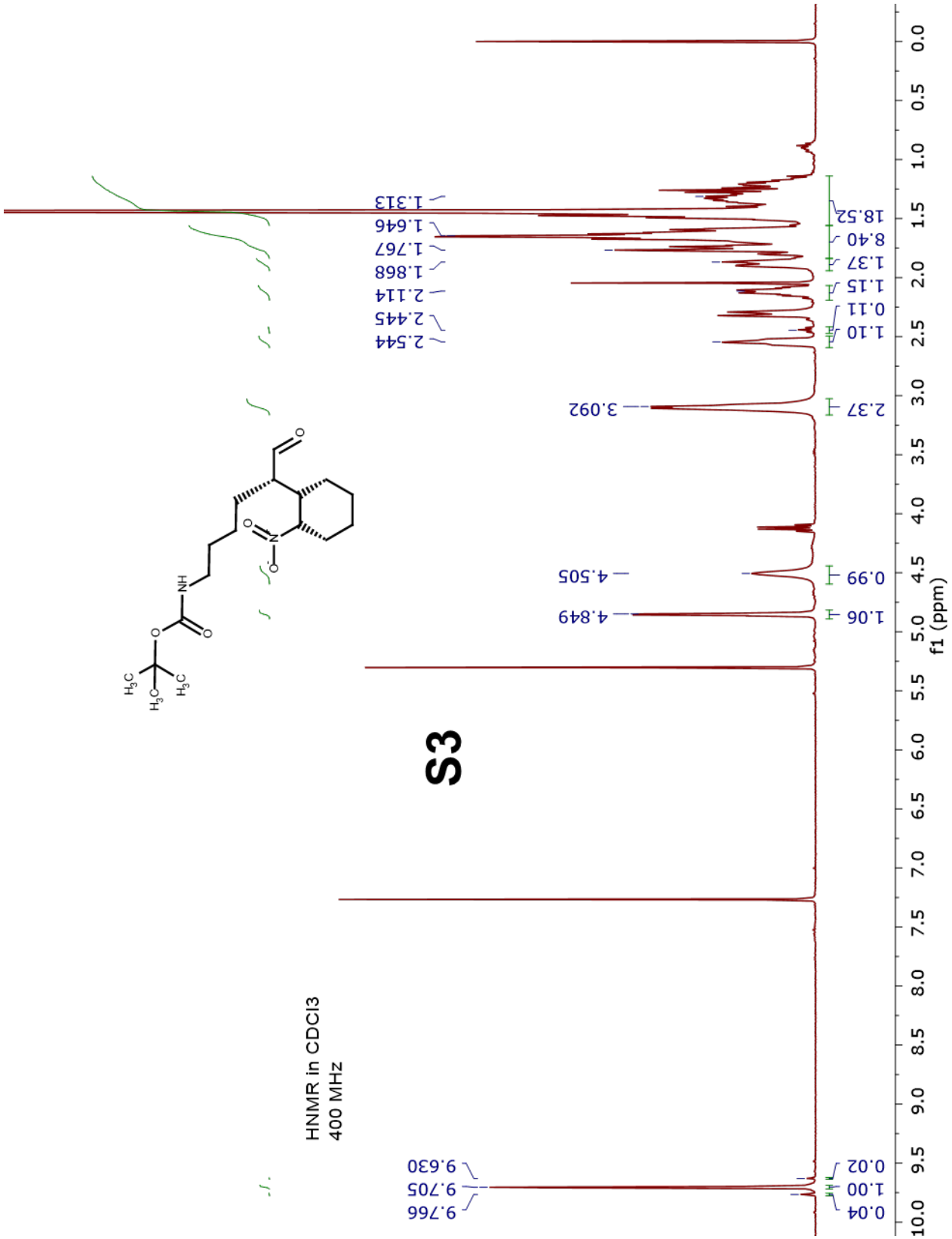
S3
HNMR in CDCl3
400 MHz
9.766
9.705
9.630
4.849
4.505
3.092
2.544
2.445
2.114
1.868
1.767
1.646
1.313
0.04
1.00
0.02
1.06
0.99
2.37
1.10
0.11
1.15
1.37
8.40
18.52
f1 (ppm)

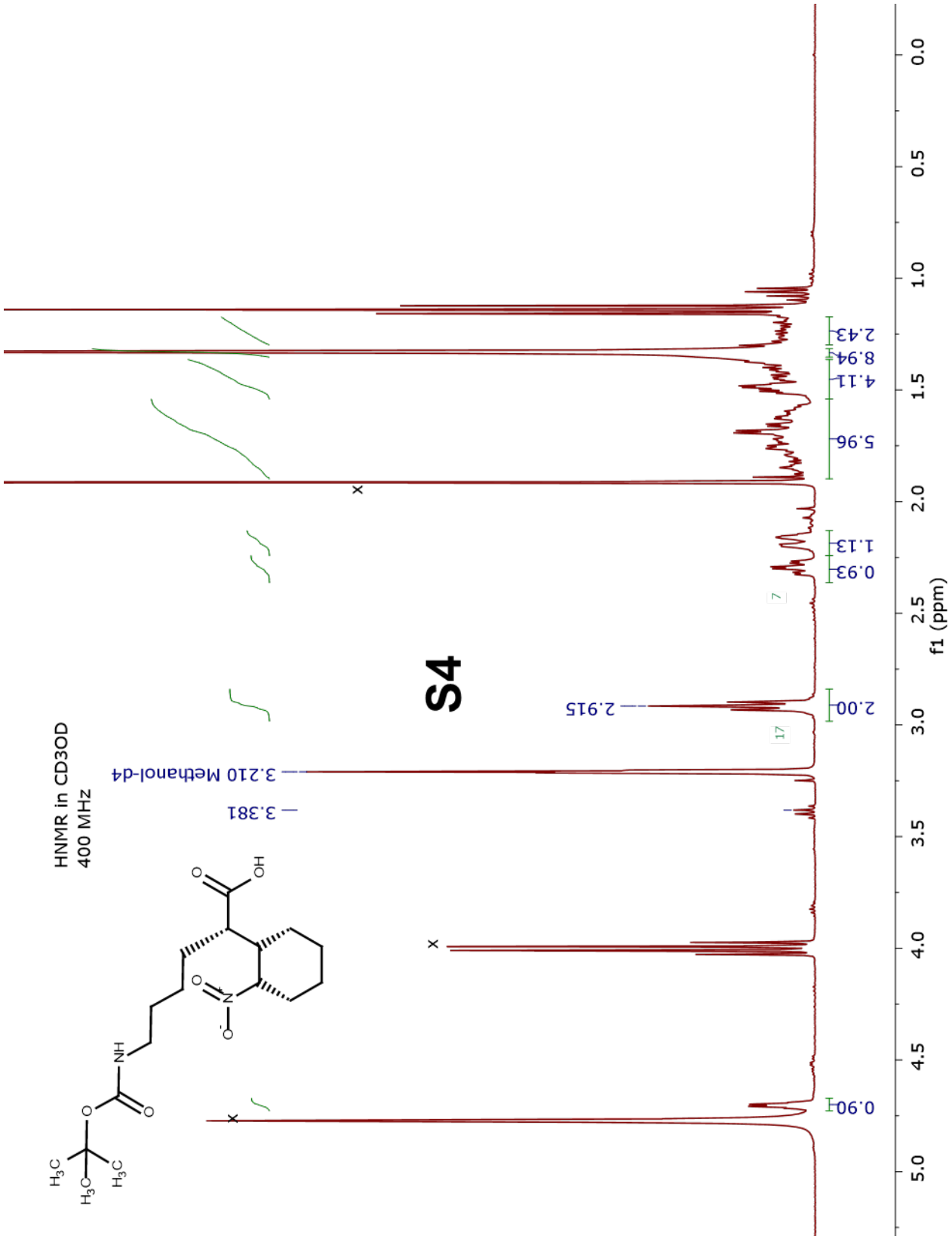
HNMR in CD3OD
400 MHz
S4
3.210 Methanol-d4
3.381
2.915
2.00
0.93
1.13
5.96
4.11
8.94
2.43
0.90
f1 (ppm)

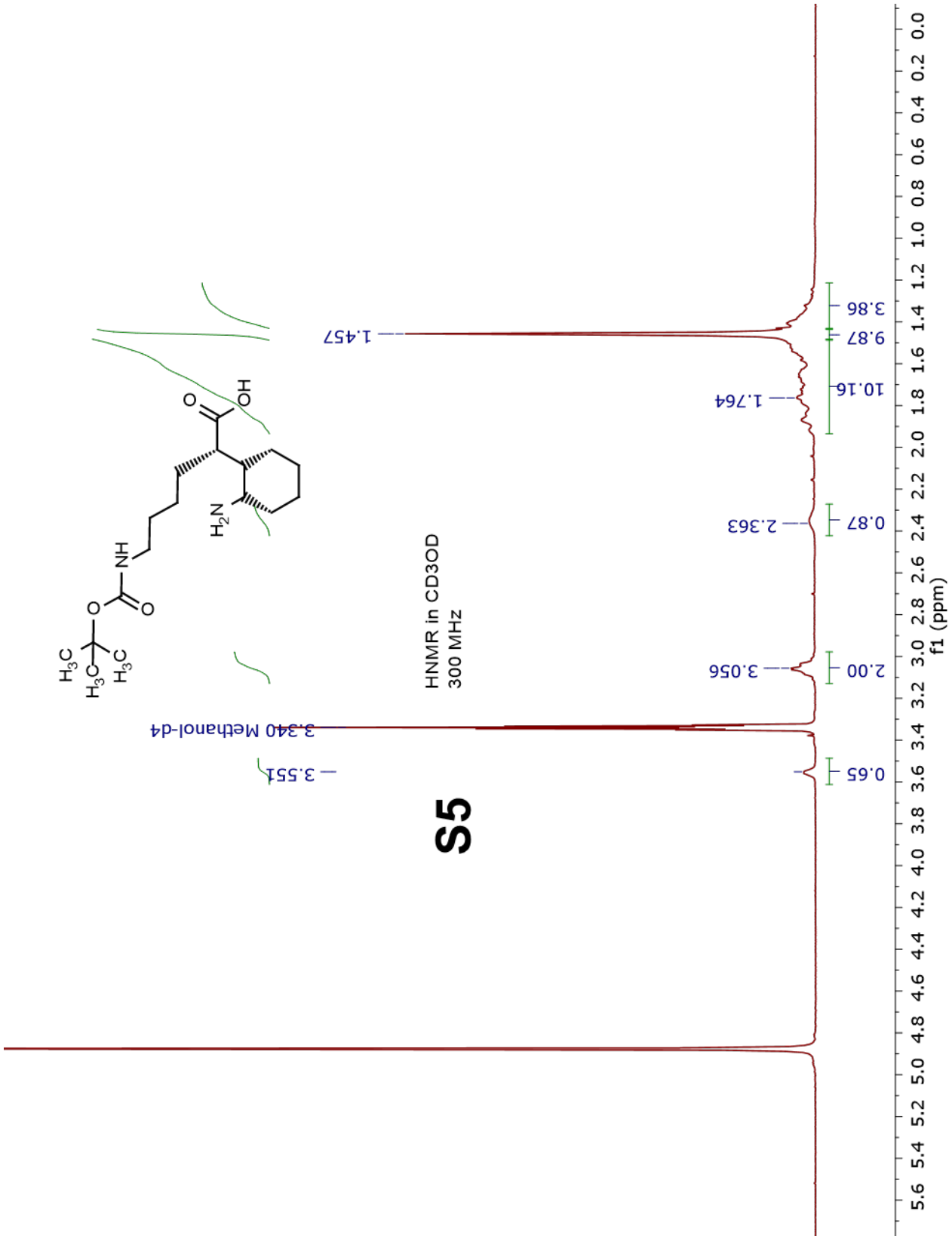
S5
HNMR in CD3OD
300 MHz
1.457
1.764
2.363
3.056
3.340 Methanol-d4
3.551
0.65
2.00
0.87
10.16
9.87
3.86
f1 (ppm)

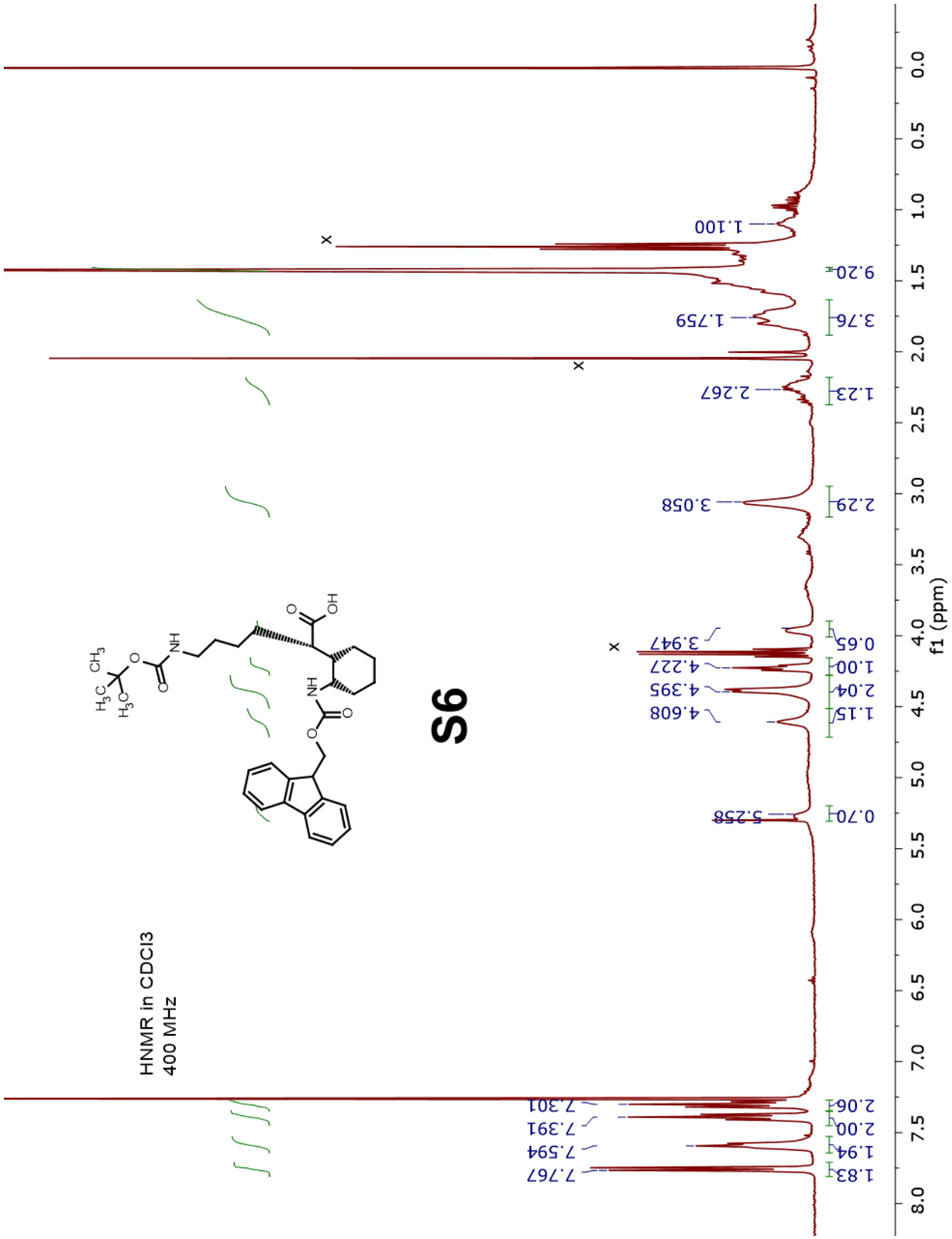
HNMR in CDCl3
400 MHz
S6
7.767
7.594
7.391
7.301
5.258
4.608
4.395
4.227
3.947
3.058
2.267
1.759
1.100
1.83
1.94
2.00
2.06
0.70
1.15
2.04
1.00
0.65
2.29
1.23
3.76
9.20
f1 (ppm)

B. ^{13}C-NMR Spectra

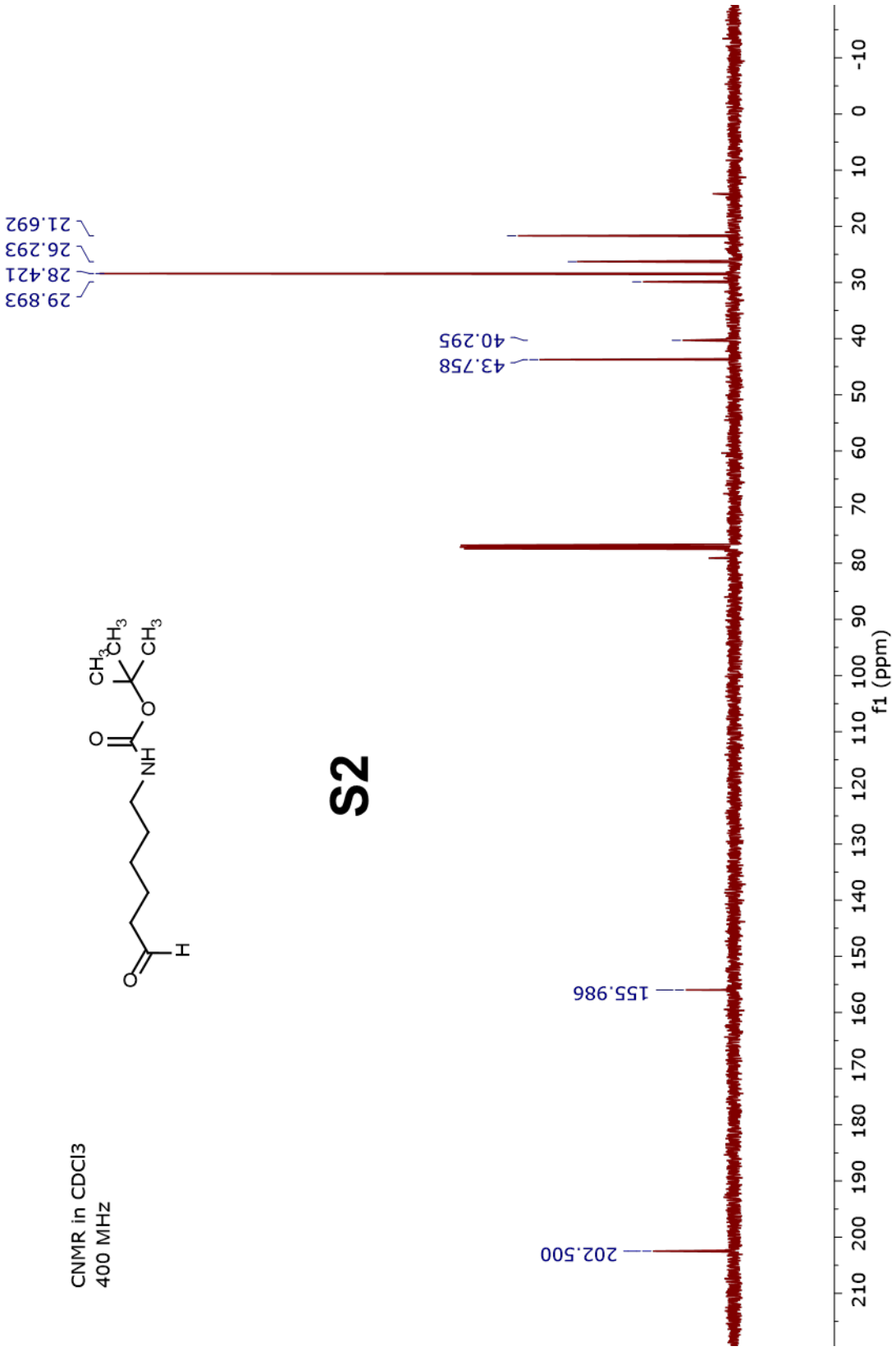

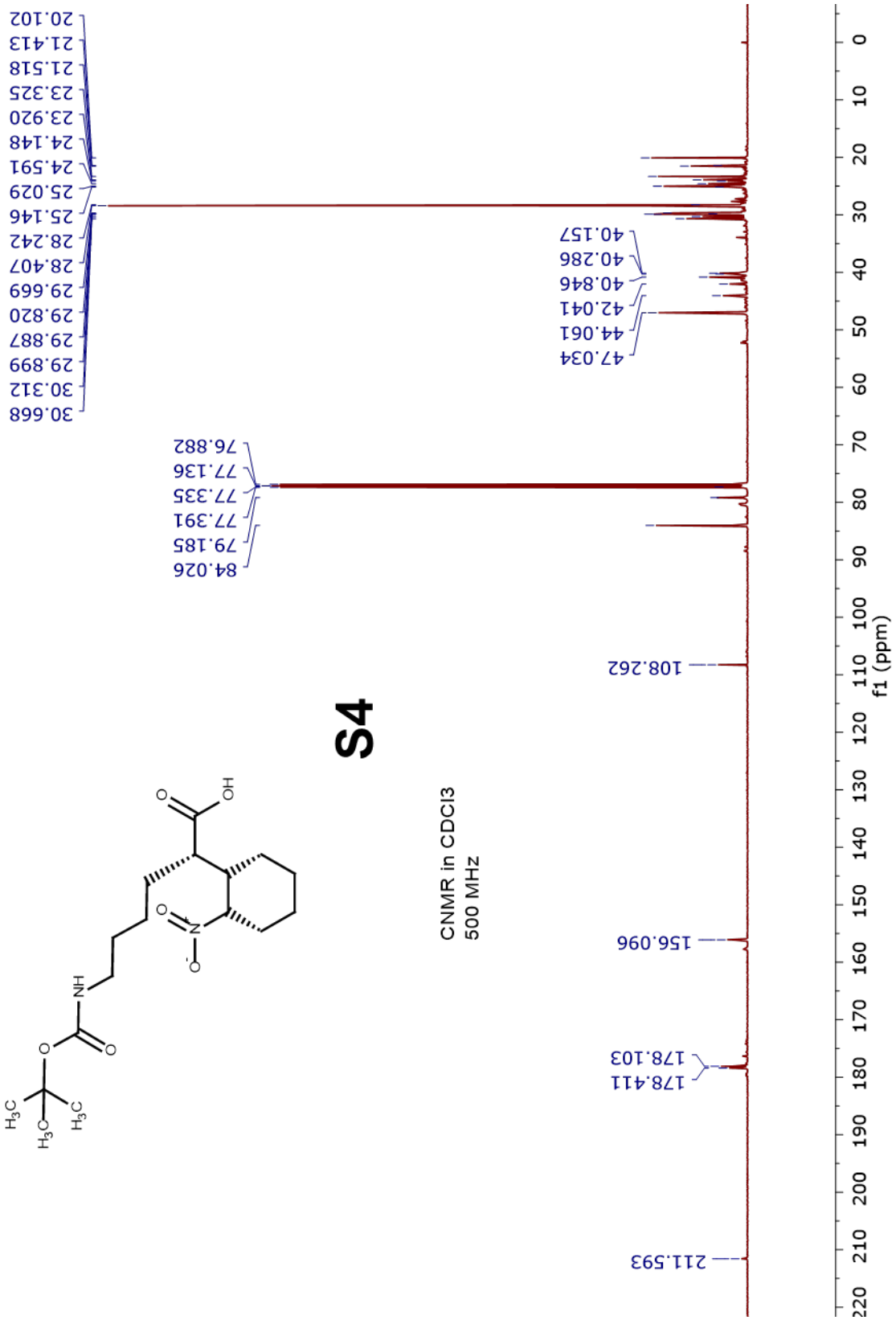
S4
CNMR in CDCl3
500 MHz
211.593
178.411
178.103
156.096
108.262
84.026
79.185
77.391
77.335
77.136
76.882
47.034
44.061
42.041
40.846
40.286
40.157
30.668
30.312
29.899
29.887
29.820
29.669
28.407
28.242
25.146
25.029
24.591
24.148
23.920
23.325
21.518
21.413
20.102
f1 (ppm)

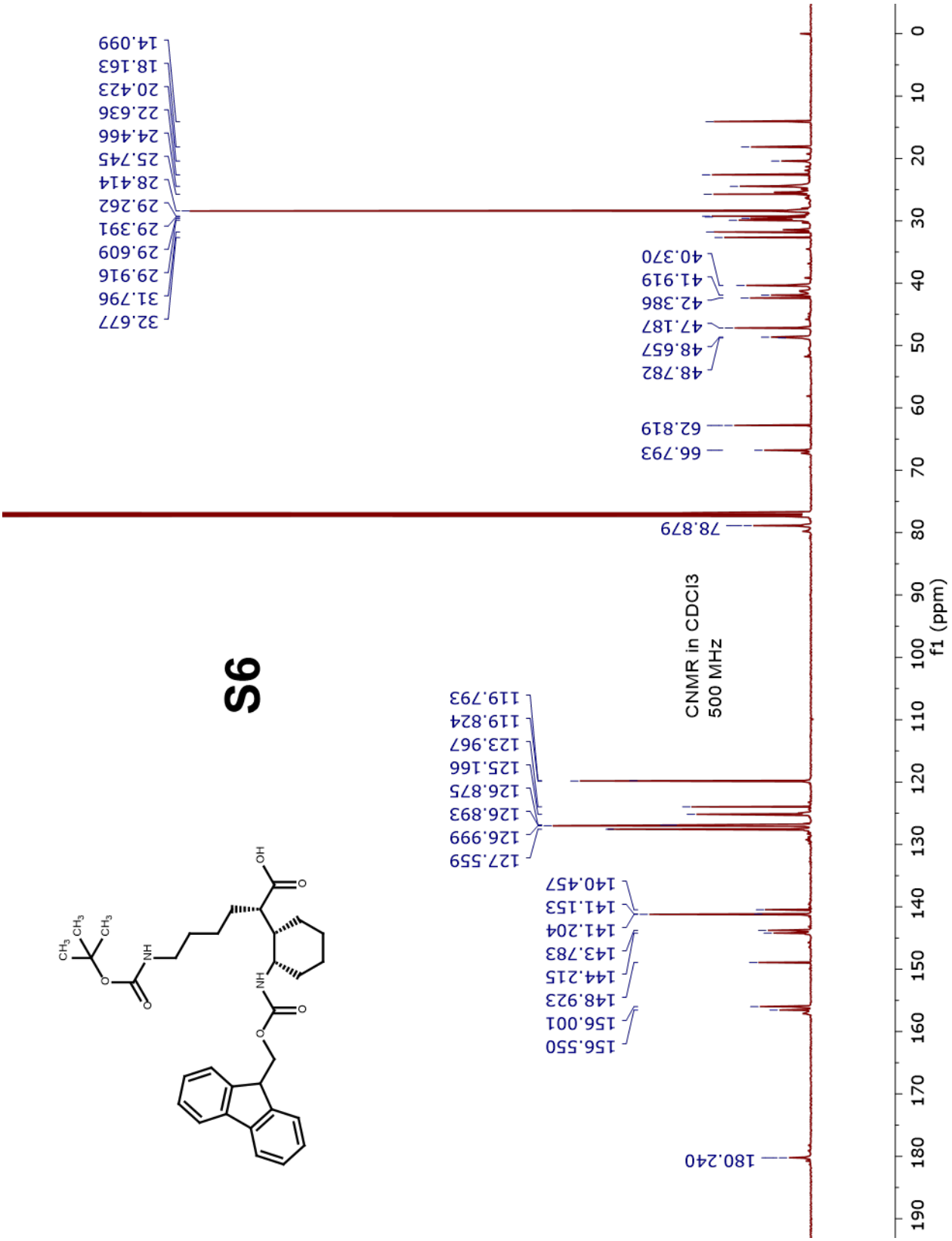
S6
CNMR in CDCl3
500 MHz
f1 (ppm)
14.099
18.163
20.423
22.636
24.466
25.745
28.414
29.262
29.391
29.609
29.916
31.796
32.677
40.370
41.919
42.386
47.187
48.657
48.782
62.819
66.793
78.879
119.793
119.824
123.967
125.166
126.875
126.893
126.999
127.559
140.457
141.153
141.204
143.783
144.215
148.923
156.001
156.550
180.240

C. VT ^{1}H-NMR Spectra

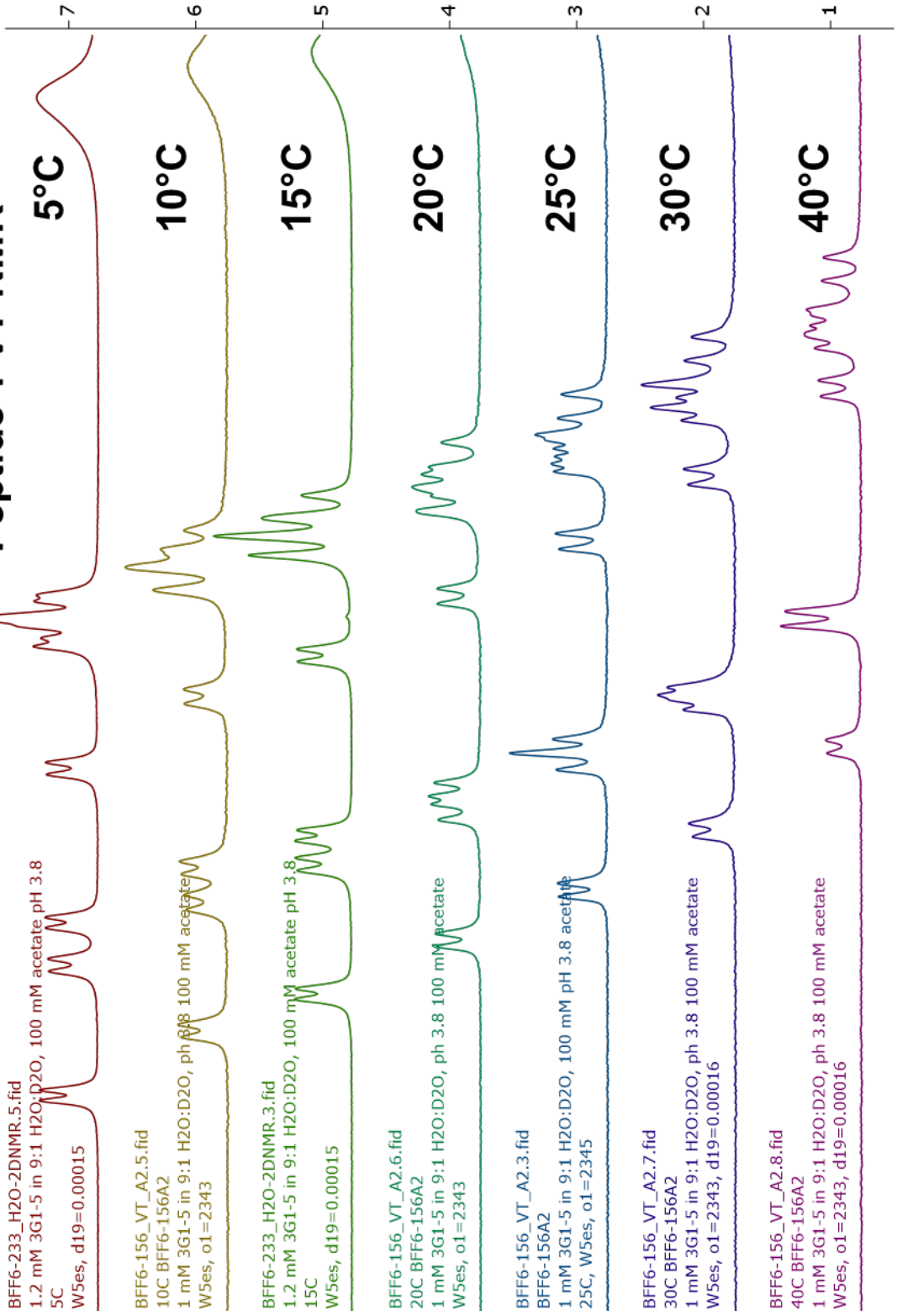

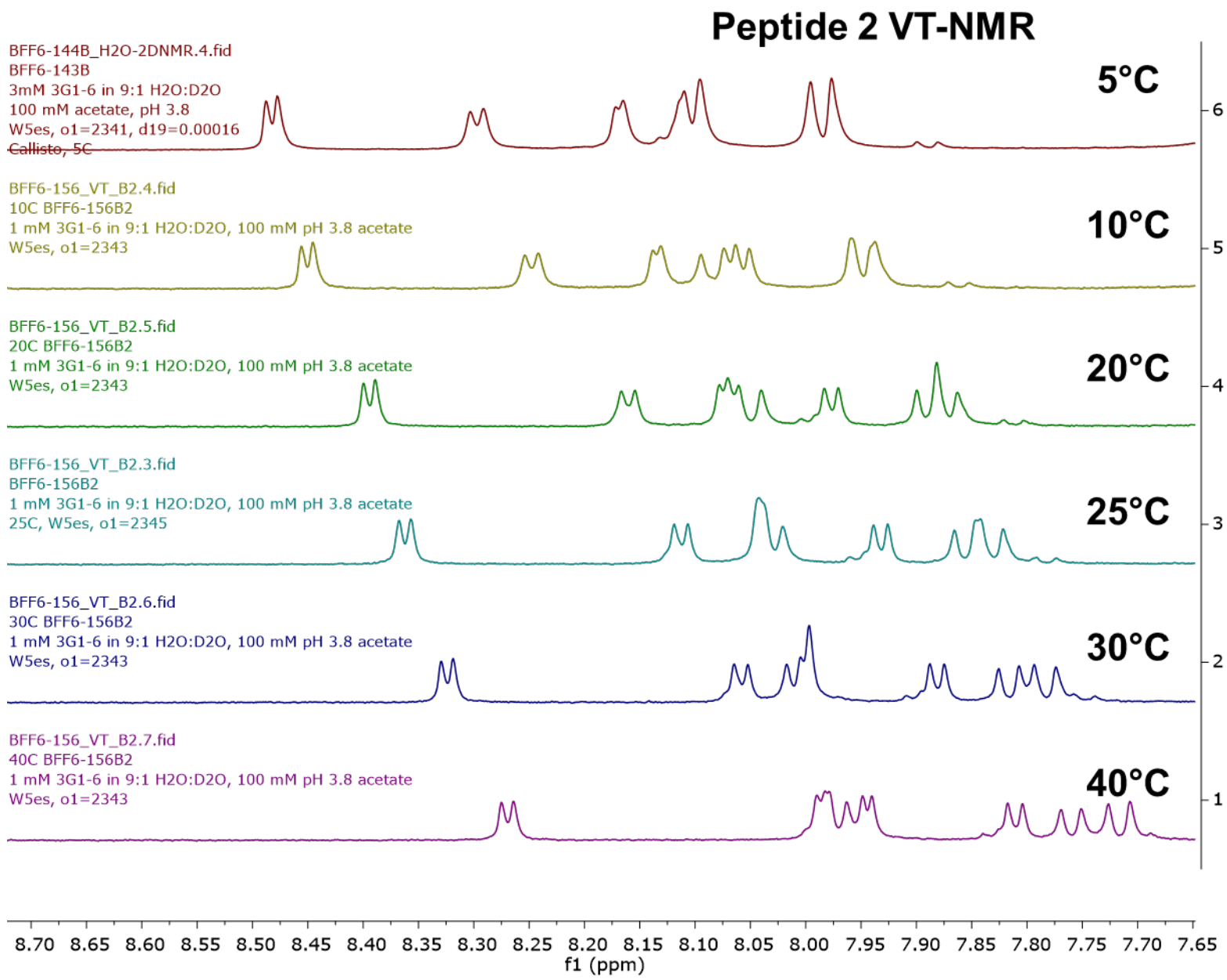
Peptide 2 VT-NMR
BFF6-144B_H2O-2DNMR.4.fid
BFF6-143B
3mM 3G1-6 in 9:1 H2O:D2O
100 mM acetate, pH 3.8
W5es, o1=2341, d19=0.00016
Callisto, 5C
5°C
BFF6-156_VT_B2.4.fid
10C BFF6-156B2
1 mM 3G1-6 in 9:1 H2O:D2O, 100 mM pH 3.8 acetate
W5es, o1=2343
10°C
BFF6-156_VT_B2.5.fid
20C BFF6-156B2
1 mM 3G1-6 in 9:1 H2O:D2O, 100 mM pH 3.8 acetate
W5es, o1=2343
20°C
BFF6-156_VT_B2.3.fid
BFF6-156B2
1 mM 3G1-6 in 9:1 H2O:D2O, 100 mM pH 3.8 acetate
25C, W5es, o1=2345
25°C
BFF6-156_VT_B2.6.fid
30C BFF6-156B2
1 mM 3G1-6 in 9:1 H2O:D2O, 100 mM pH 3.8 acetate
W5es, o1=2343
30°C
BFF6-156_VT_B2.7.fid
40C BFF6-156B2
1 mM 3G1-6 in 9:1 H2O:D2O, 100 mM pH 3.8 acetate
W5es, o1=2343
40°C
6
5
4
3
2
1
8.70 8.65 8.60 8.55 8.50 8.45 8.40 8.35 8.30 8.25 8.20 8.15 8.10 8.05 8.00 7.95 7.90 7.85 7.80 7.75 7.70 7.65
f1 (ppm)

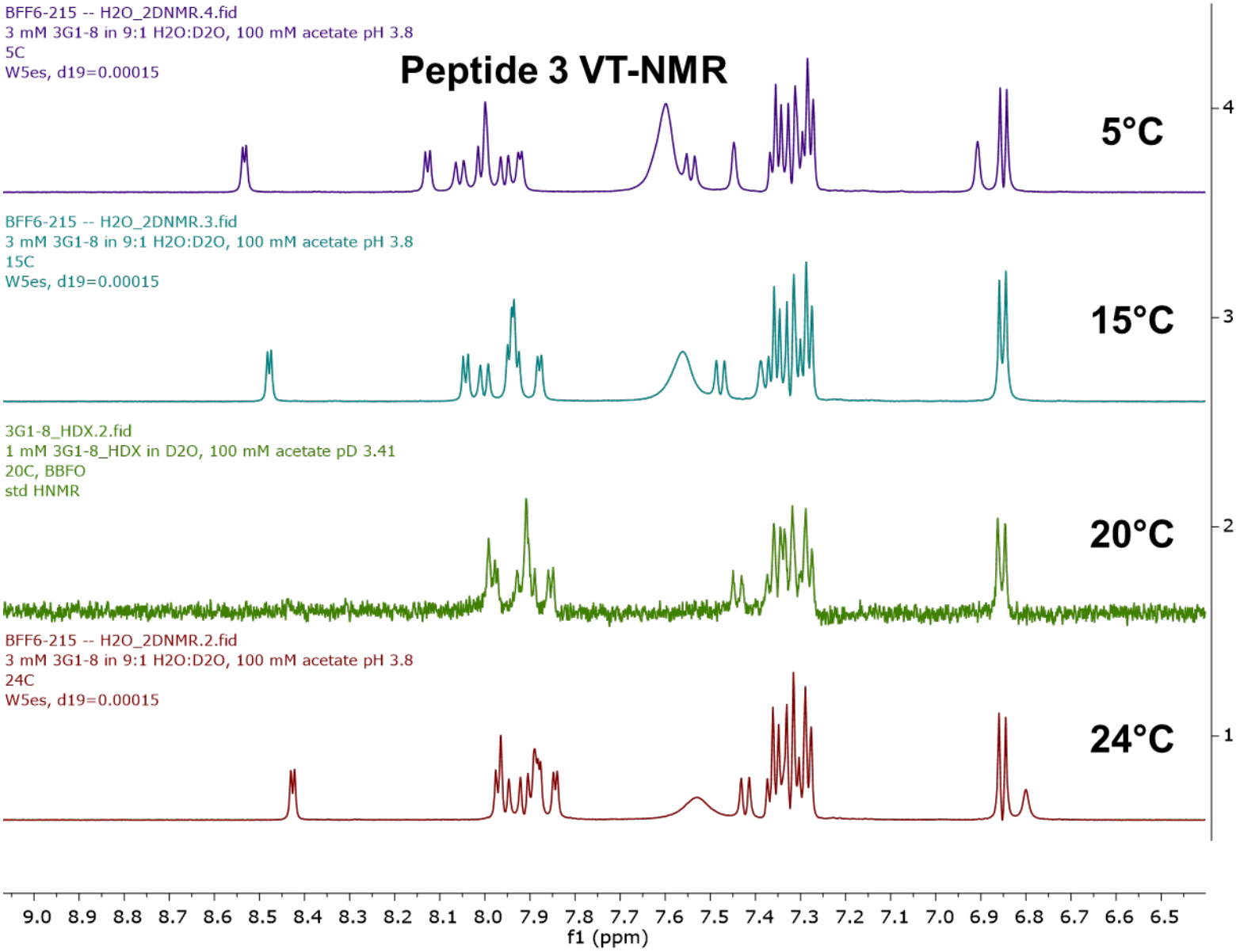
BFF6-215 -- H2O_2DNMR.4.fid
3 mM 3G1-8 in 9:1 H2O:D2O, 100 mM acetate pH 3.8
5C
W5es, d19=0.00015
Peptide 3 VT-NMR
5°C
4
BFF6-215 -- H2O_2DNMR.3.fid
3 mM 3G1-8 in 9:1 H2O:D2O, 100 mM acetate pH 3.8
15C
W5es, d19=0.00015
15°C
3
3G1-8_HDX.2.fid
1 mM 3G1-8_HDX in D2O, 100 mM acetate pD 3.41
20C, BBFO
std HNMR
20°C
2
BFF6-215 -- H2O_2DNMR.2.fid
3 mM 3G1-8 in 9:1 H2O:D2O, 100 mM acetate pH 3.8
24C
W5es, d19=0.00015
24°C
1
9.0 8.9 8.8 8.7 8.6 8.5 8.4 8.3 8.2 8.1 8.0 7.9 7.8 7.7 7.6 7.5 7.4 7.3 7.2 7.1 7.0 6.9 6.8 6.7 6.6 6.5
f1 (ppm)

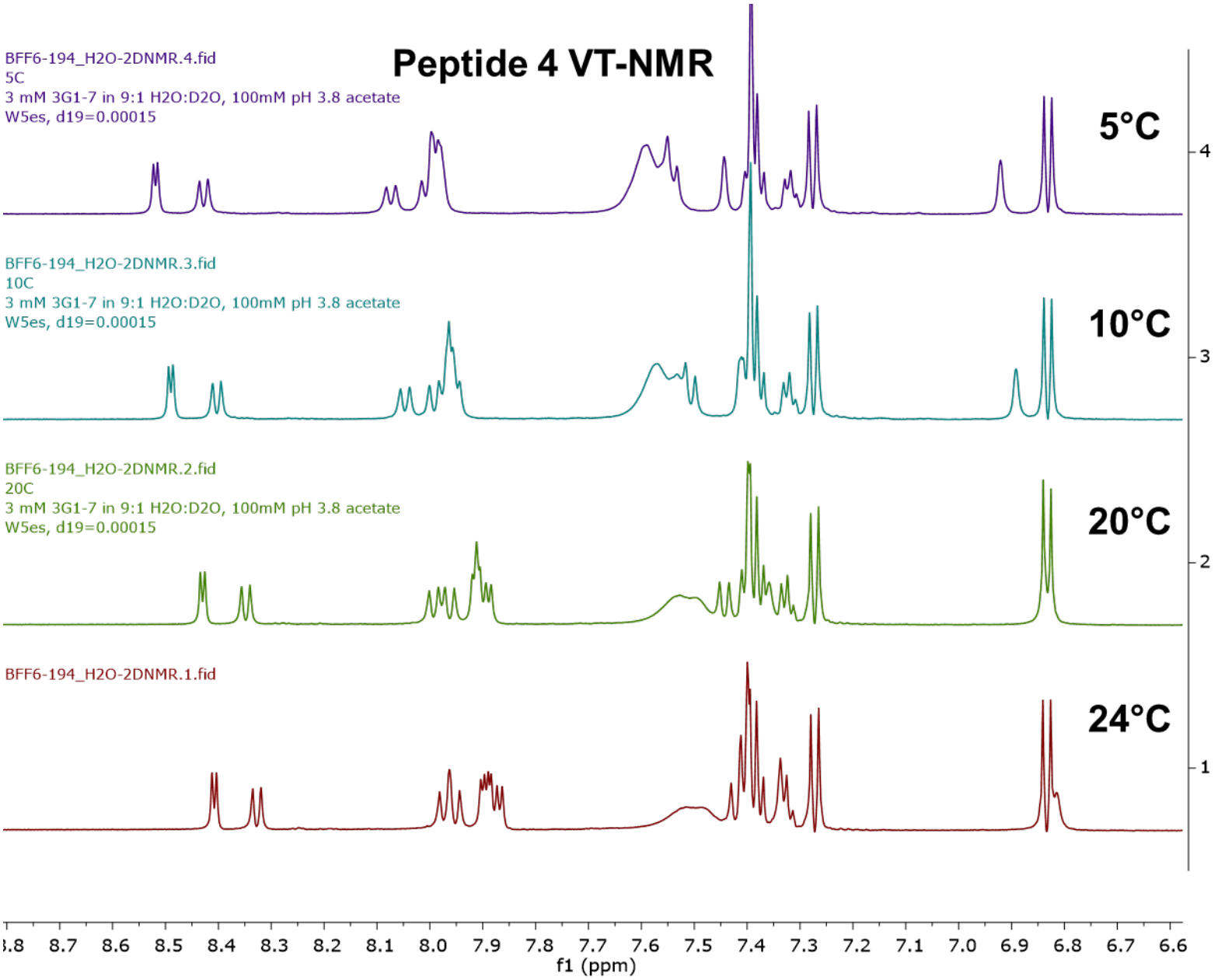
Peptide 4 VT-NMR
BFF6-194_H2O-2DNMR.4.fid
5C
3 mM 3G1-7 in 9:1 H2O:D2O, 100mM pH 3.8 acetate
W5es, d19=0.00015
5°C
BFF6-194_H2O-2DNMR.3.fid
10C
3 mM 3G1-7 in 9:1 H2O:D2O, 100mM pH 3.8 acetate
W5es, d19=0.00015
10°C
BFF6-194_H2O-2DNMR.2.fid
20C
3 mM 3G1-7 in 9:1 H2O:D2O, 100mM pH 3.8 acetate
W5es, d19=0.00015
20°C
BFF6-194_H2O-2DNMR.1.fid
24°C
4
3
2
1
8.8 8.7 8.6 8.5 8.4 8.3 8.2 8.1 8.0 7.9 7.8 7.7 7.6 7.5 7.4 7.3 7.2 7.1 7.0 6.9 6.8 6.7 6.6
f1 (ppm)

D. Hydrogen-Deuterium Exchange ^{1}H-NMR Spectra

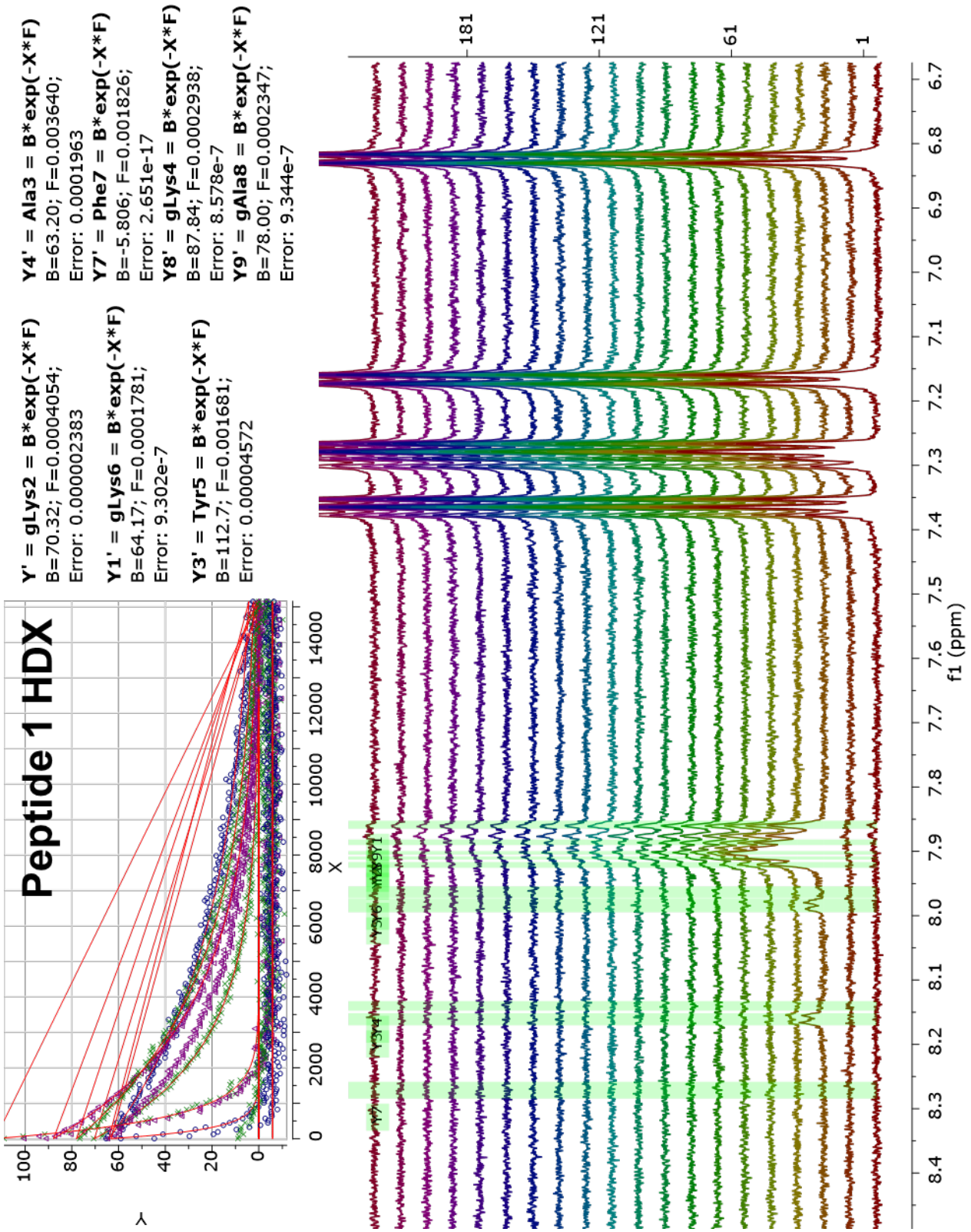

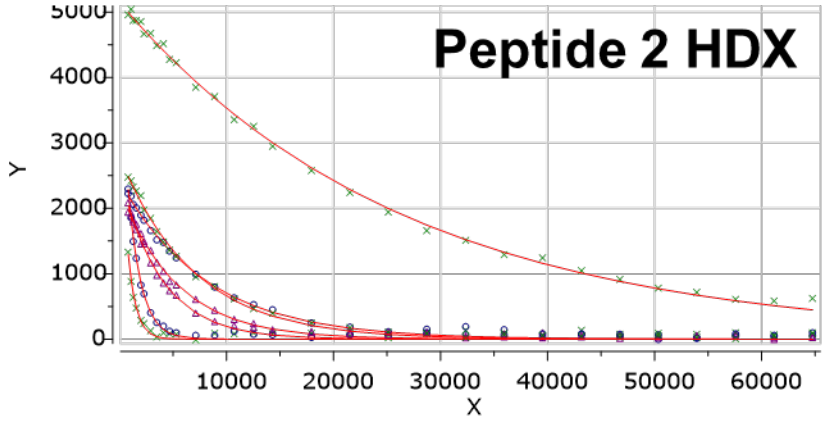

Y' = B*exp(-X*F)
B=5150; F=0.00003772;
Error: 3.125e-7

Y1' = B*exp(-X*F)
B=2432; F=0.0001243;
Error: 0.000001739

Y2' = B*exp(-X*F)
B=2307; F=0.0001889;
Error: 0.000004201

Y3' = B*exp(-X*F)
B=3840; F=0.001321;
Error: 0.00009752

Y4' = B*exp(-X*F)
B=4529; F=0.0008310;
Error: 0.00003016

Y5' = B*exp(-X*F)
B=2521; F=0.0002573;
Error: 0.000005609

Y6' = B*exp(-X*F)
B=2801; F=0.0001449;
Error: 0.000002311

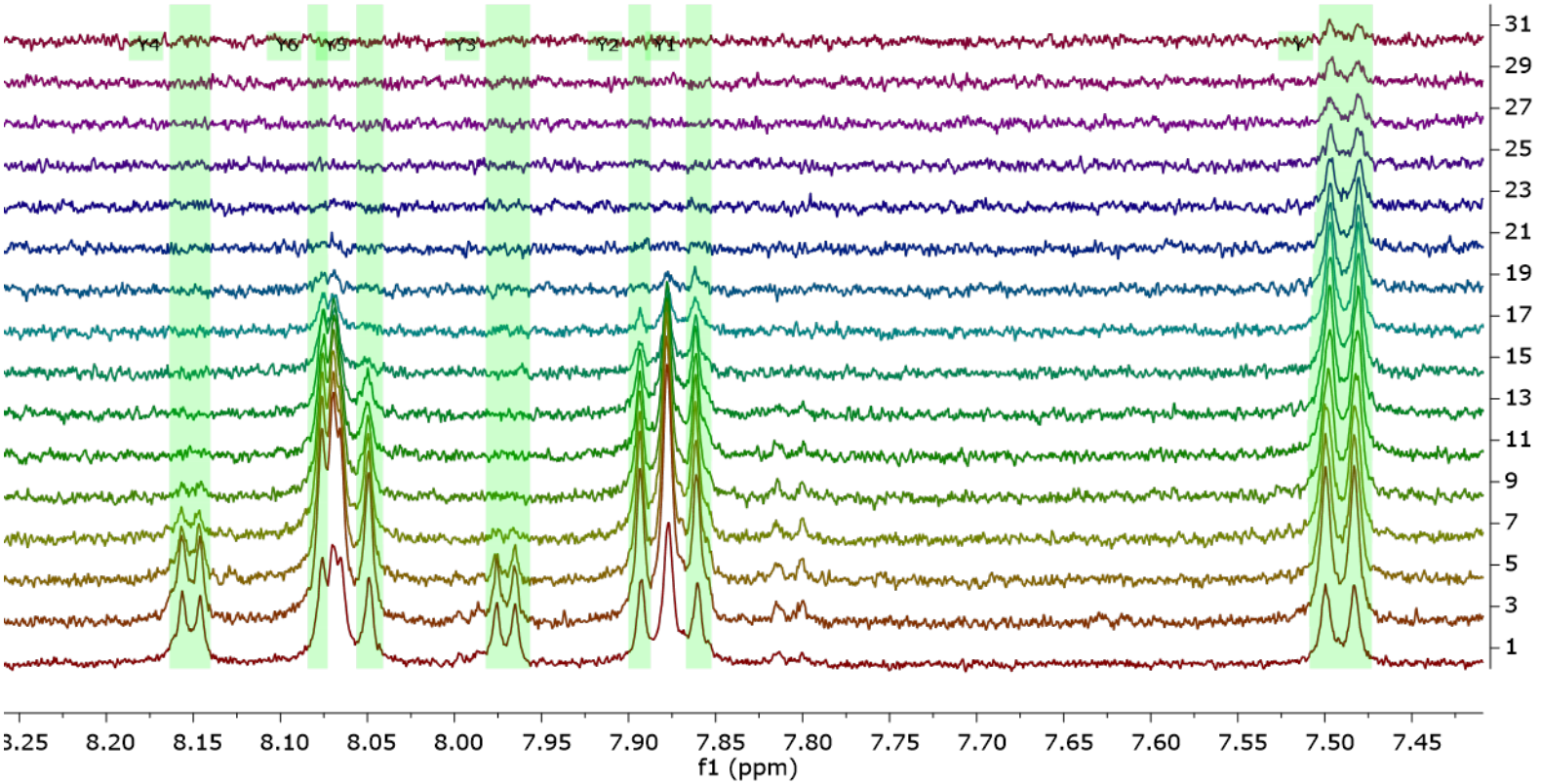

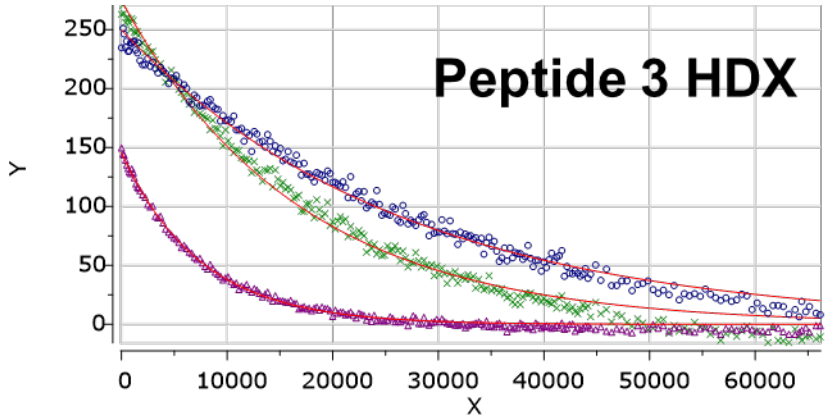

Y' = B*exp(-X*F)
B=274.6; F=0.00005986;
Error: 4.284e-7

Y1' = B*exp(-X*F)
B=249.7; F=0.00003807;
Error: 2.048e-7

Y2' = B*exp(-X*F)
B=145.5; F=0.0001340;
Error: 9.174e-7

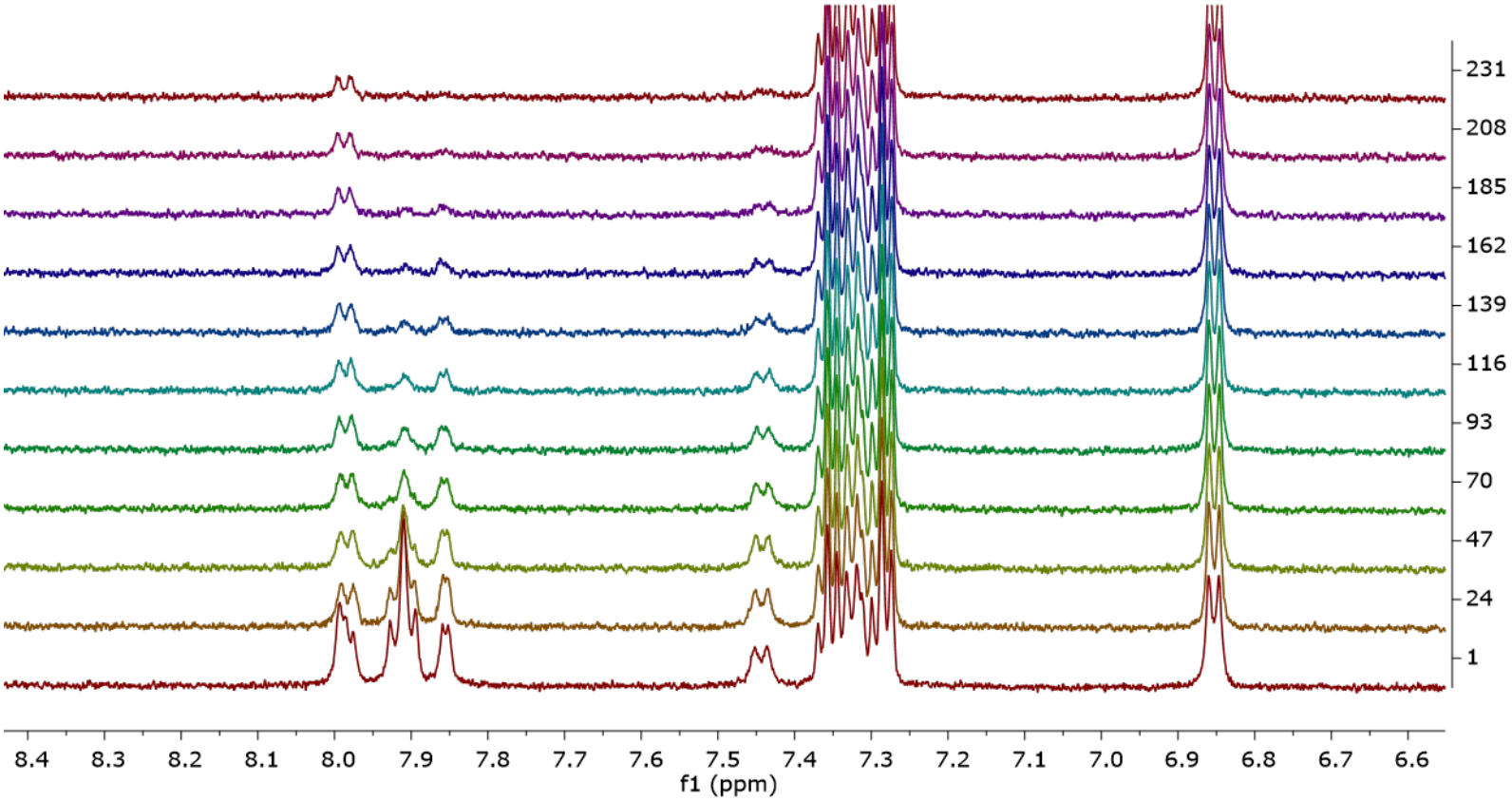

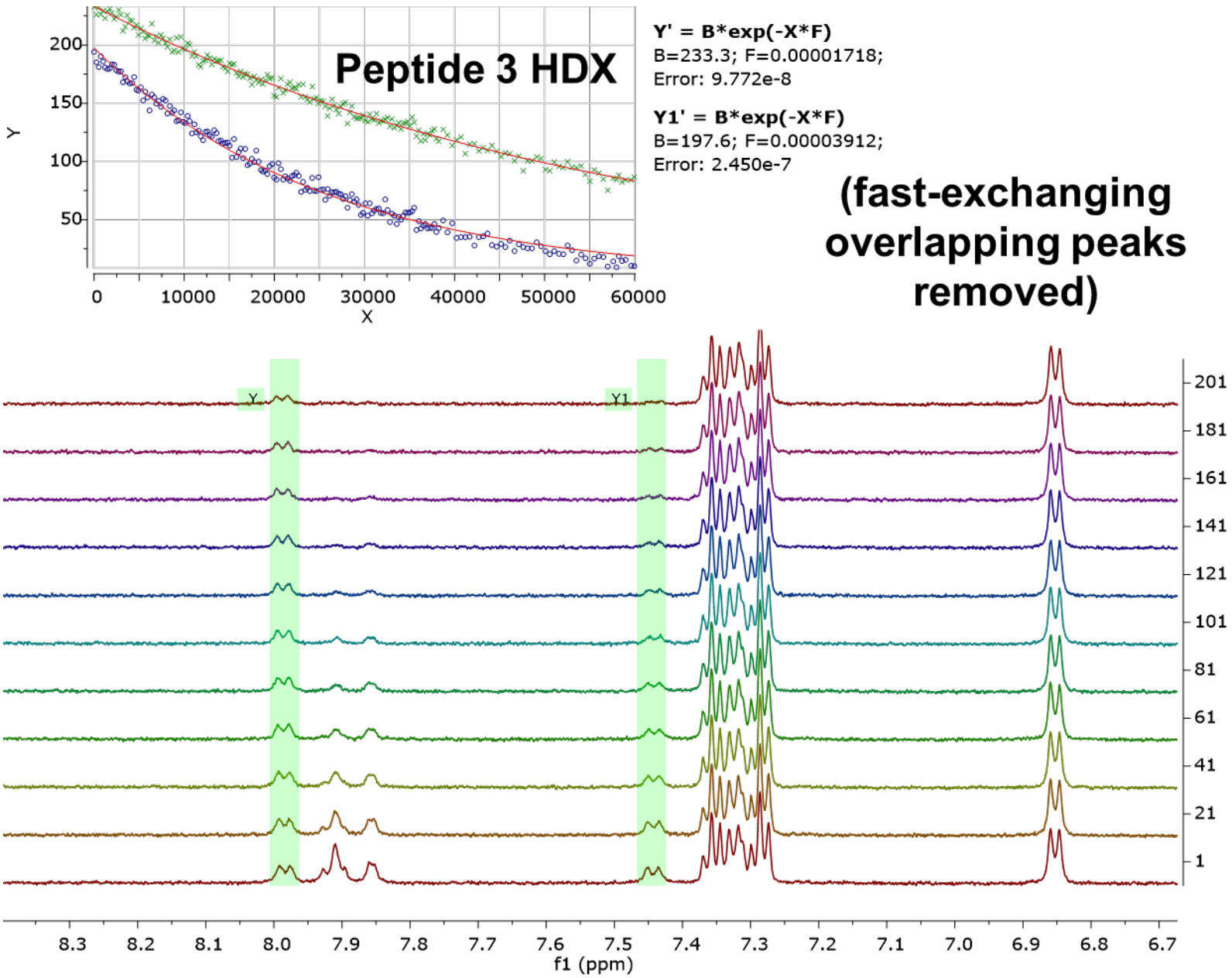
Peptide 3 HDX
Y' = B*exp(-X*F)
B=233.3; F=0.00001718;
Error: 9.772e-8
Y1' = B*exp(-X*F)
B=197.6; F=0.00003912;
Error: 2.450e-7
(fast-exchanging overlapping peaks removed)
Y
X
Y1
f1 (ppm)

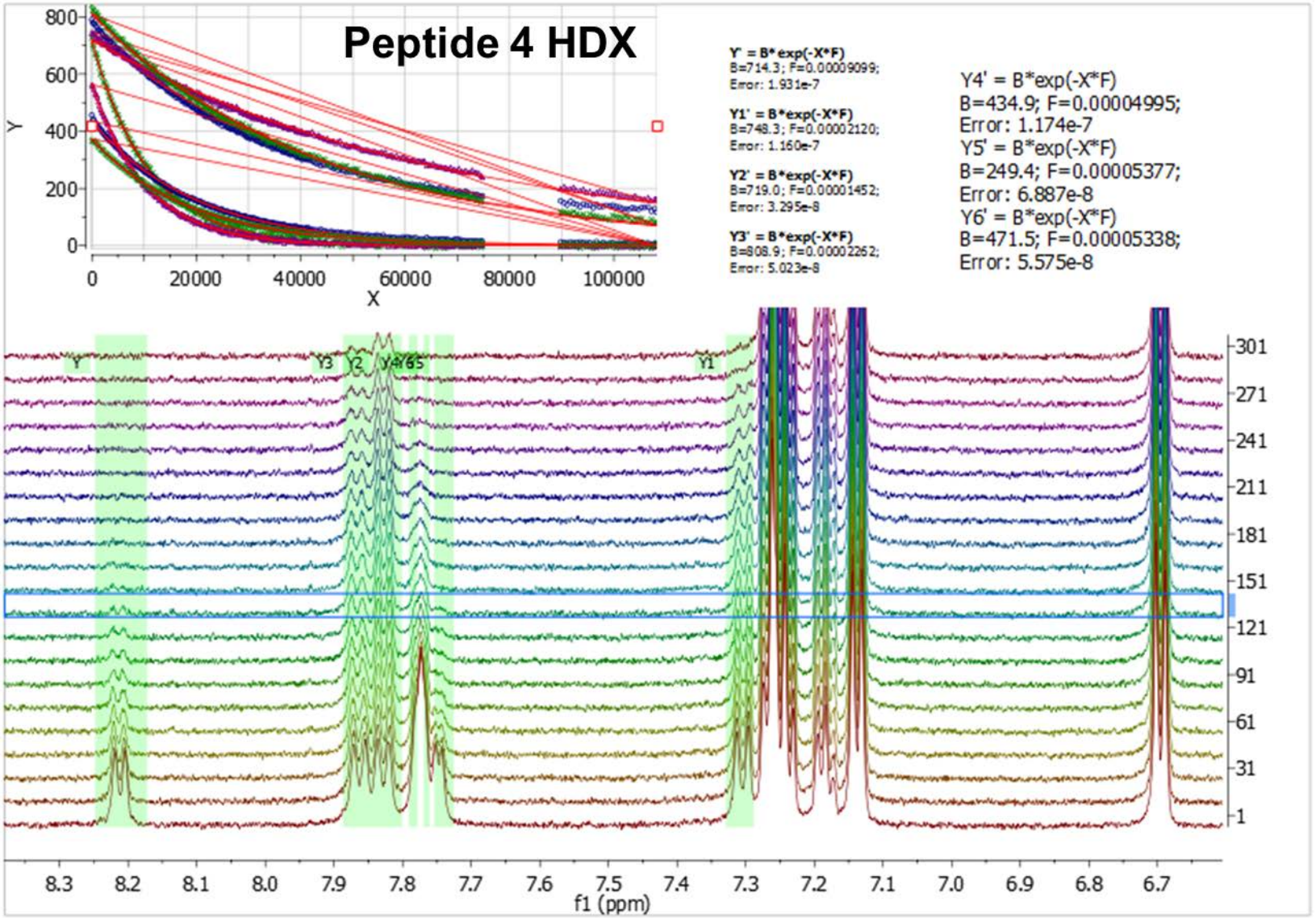
Peptide 4 HDX
Y' = B*exp(-X*F)
B=714.3; F=0.00009099;
Error: 1.931e-7
Y1' = B*exp(-X*F)
B=748.3; F=0.00002120;
Error: 1.160e-7
Y2' = B*exp(-X*F)
B=719.0; F=0.00001452;
Error: 3.295e-8
Y3' = B*exp(-X*F)
B=808.9; F=0.00002262;
Error: 5.023e-8
Y4' = B*exp(-X*F)
B=434.9; F=0.00004995;
Error: 1.174e-7
Y5' = B*exp(-X*F)
B=249.4; F=0.00005377;
Error: 6.887e-8
Y6' = B*exp(-X*F)
B=471.5; F=0.00005338;
Error: 5.575e-8
Y
X
f1 (ppm)

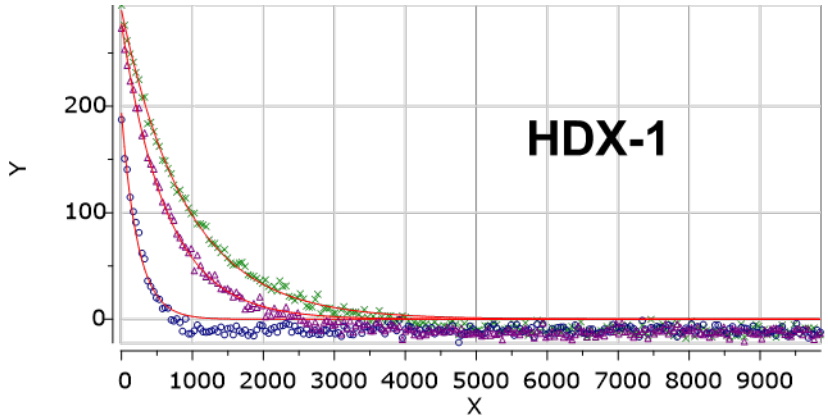

3/21/16, 3HDX-10 in 100 mM acetate, pD 3.41

Y' = Ala1 = B*exp(-X*F)
B=289.8; F=0.001091;
Error: 0.00001312

Y1' = Lys3 = B*exp(-X*F)
B=193.5; F=0.004329;
Error: 0.0001640

Y2' = Tyr2 = B*exp(-X*F)
B=277.3; F=0.001579;
Error: 0.00002843

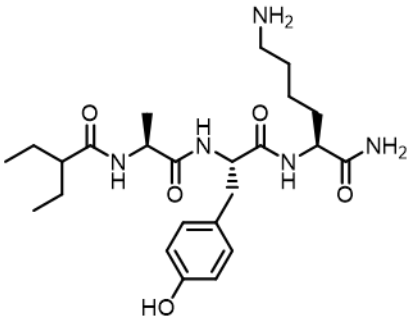

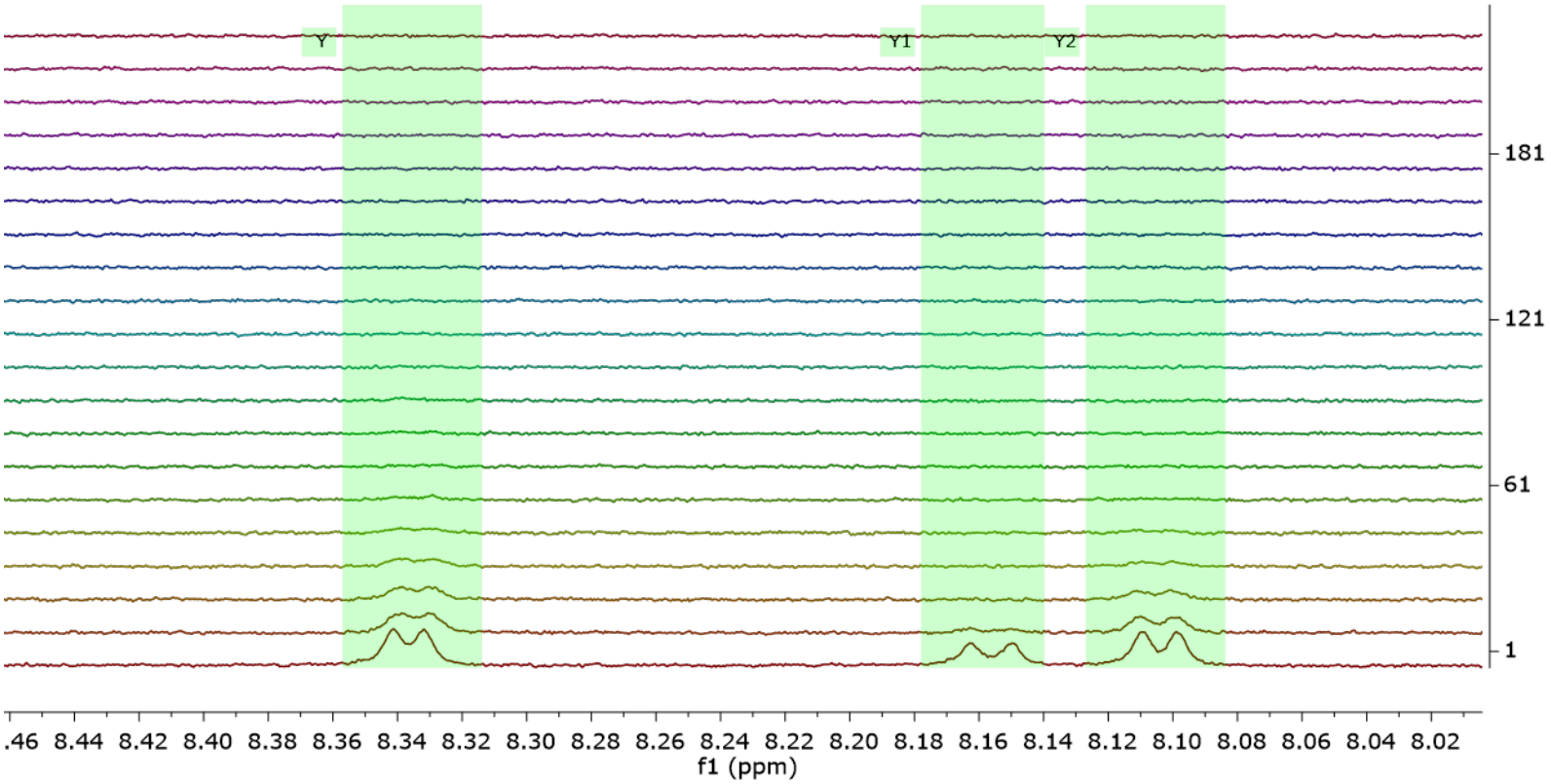

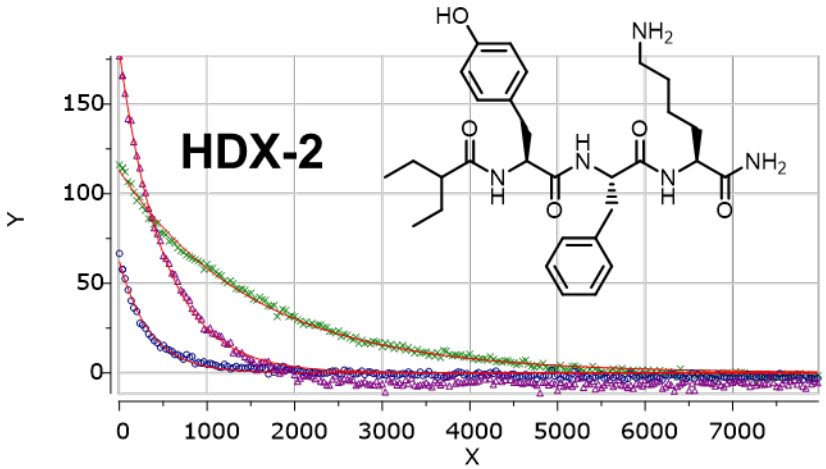

3/15/16, 3HDX-8 in D2O, 100 mM acetate, pD 3.41

Y' = Tyr1 = B*exp(-X*F)
B=112.8; F=0.0006588;
Error: 0.000003253

Y1' = Lys3 = B*exp(-X*F)
B=62.08; F=0.002850;
Error: 0.00005381

Y2' = Phe2 = B*exp(-X*F)
B=179.0; F=0.001974;
Error: 0.00002682

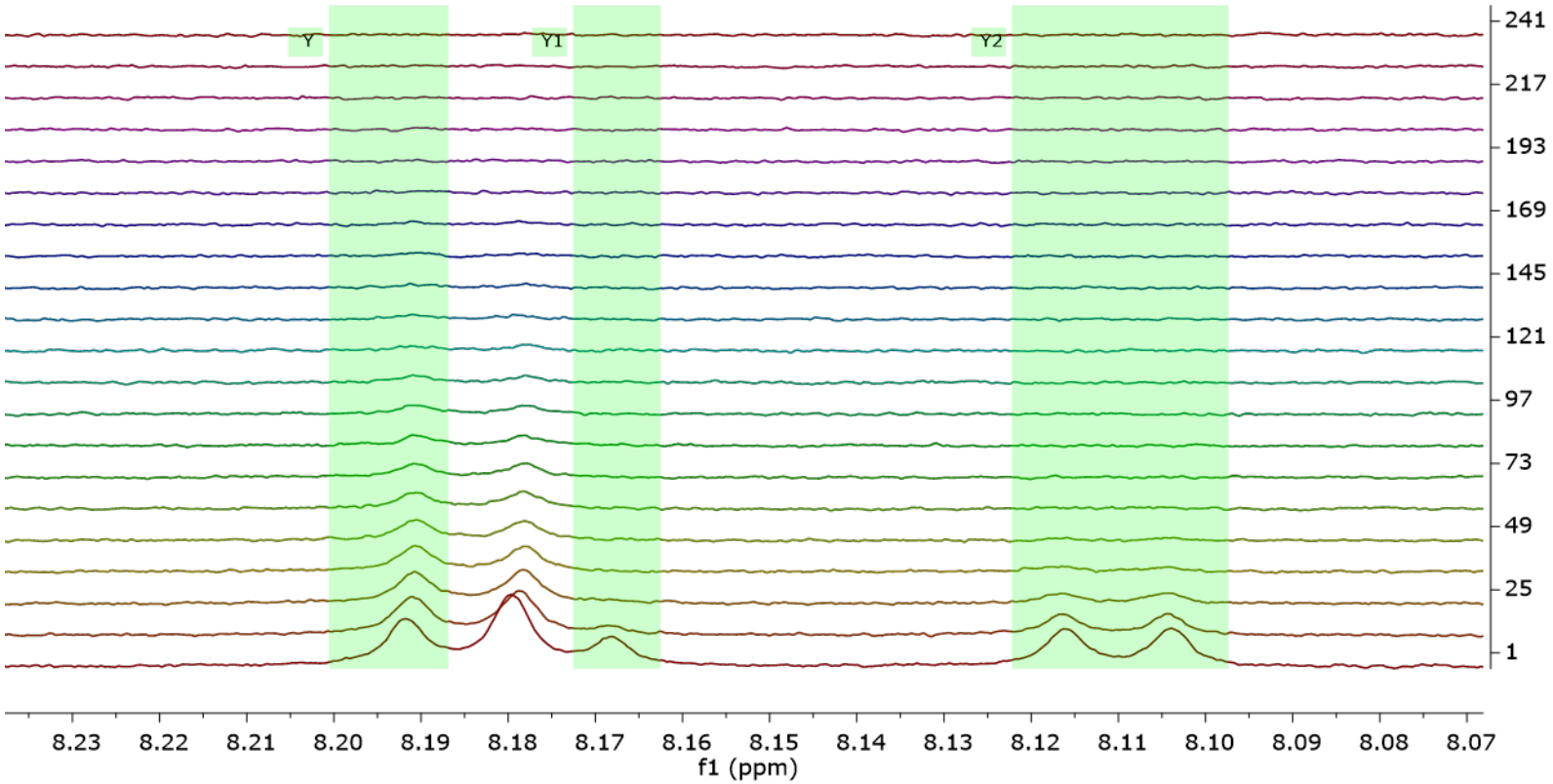

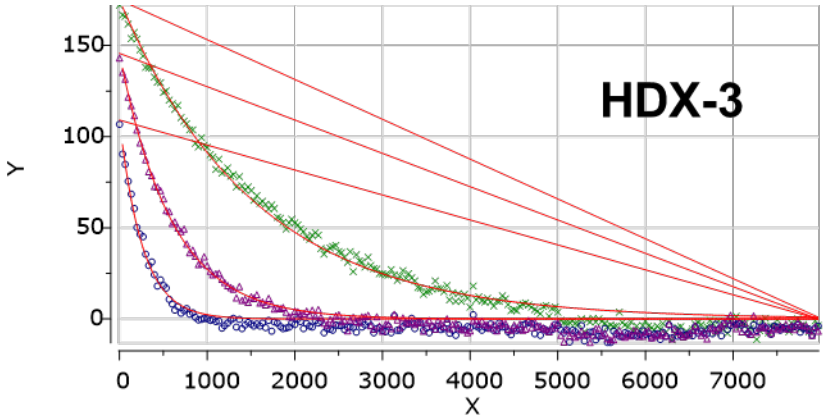

3/19/16, 3HDX-9 in 100 mM acetate, pD 3.41

Y' = Phe1 = B*exp(-X*F)
B=175.0; F=0.0006516;
Error: 0.000005156

Y1' = Lys3 = B*exp(-X*F)
B=109.1; F=0.003833;
Error: 0.0001249

Y2' = Tyr2 = B*exp(-X*F)
B=145.7; F=0.001675;
Error: 0.00002644

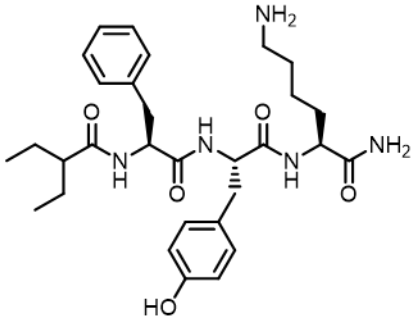

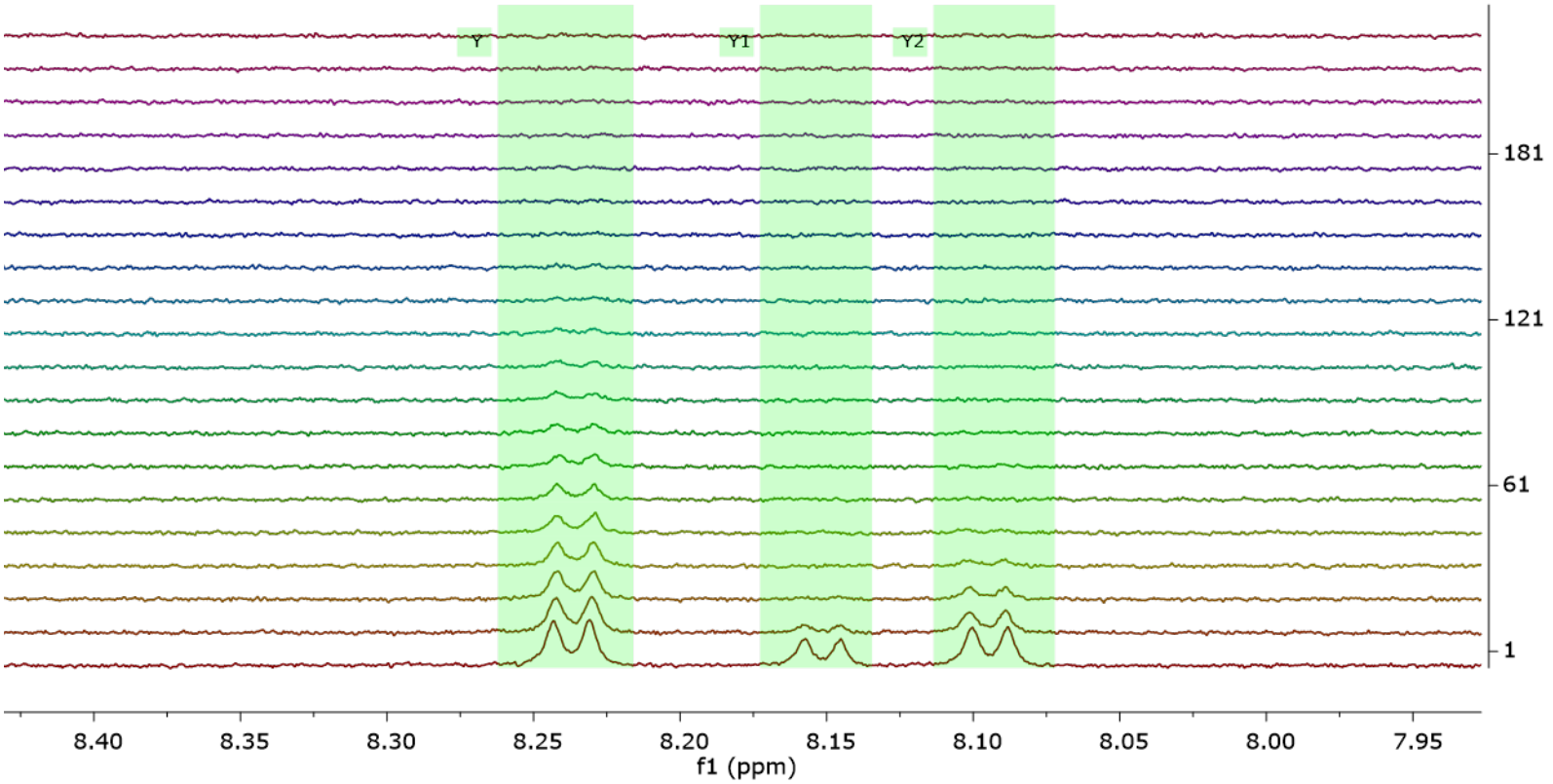

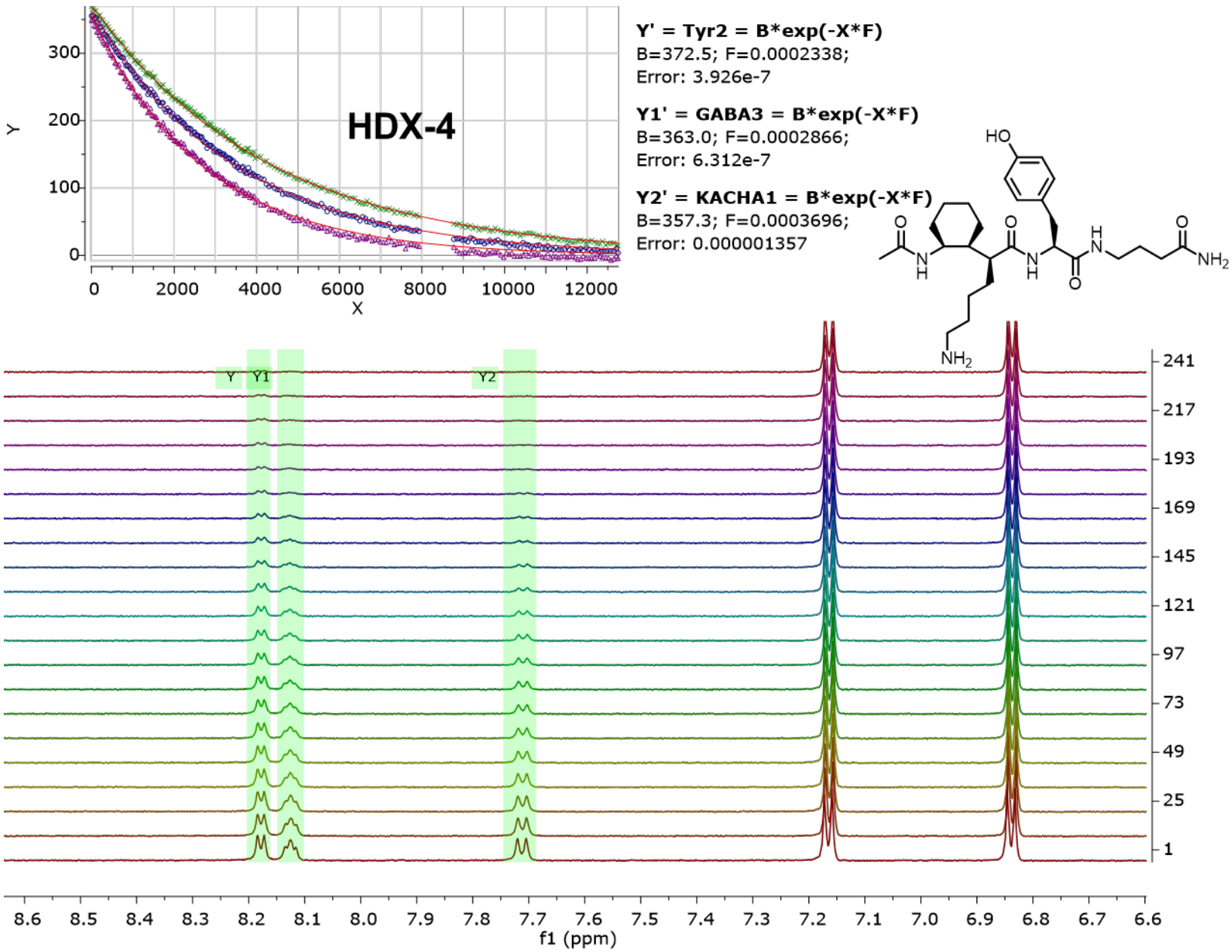
HDX-4
Y
X
0
100
200
300
0
2000
4000
6000
8000
10000
12000
Y' = Tyr2 = B*exp(-X*F)
B=372.5; F=0.0002338;
Error: 3.926e-7
Y1' = GABA3 = B*exp(-X*F)
B=363.0; F=0.0002866;
Error: 6.312e-7
Y2' = KACHA1 = B*exp(-X*F)
B=357.3; F=0.0003696;
Error: 0.000001357
HO
O
N
H
O
N
H
O
N
H
O
NH2
NH2
Y
Y1
Y2
241
217
193
169
145
121
97
73
49
25
1
8.6
8.5
8.4
8.3
8.2
8.1
8.0
7.9
7.8
7.7
7.6
7.5
7.4
7.3
7.2
7.1
7.0
6.9
6.8
6.7
6.6
f1 (ppm)

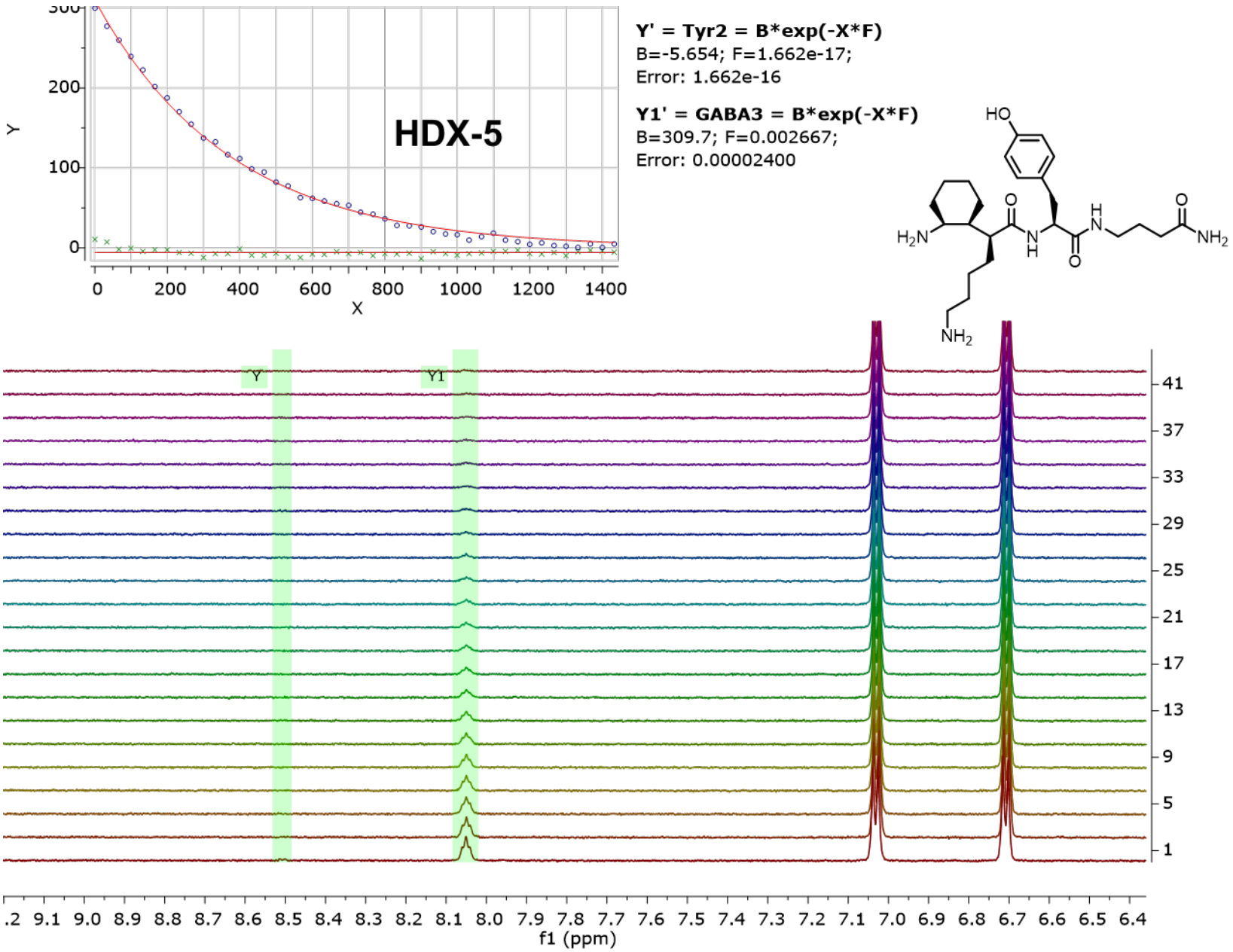
HDX-5
Y
X
0
100
200
0
200
400
600
800
1000
1200
1400
Y' = Tyr2 = B*exp(-X*F)
B=-5.654; F=1.662e-17;
Error: 1.662e-16
Y1' = GABA3 = B*exp(-X*F)
B=309.7; F=0.002667;
Error: 0.00002400
HO
H2N
NH2
NH2
Y
Y1
41
37
33
29
25
21
17
13
9
5
1
f1 (ppm)

E. 2D-NMR Spectra

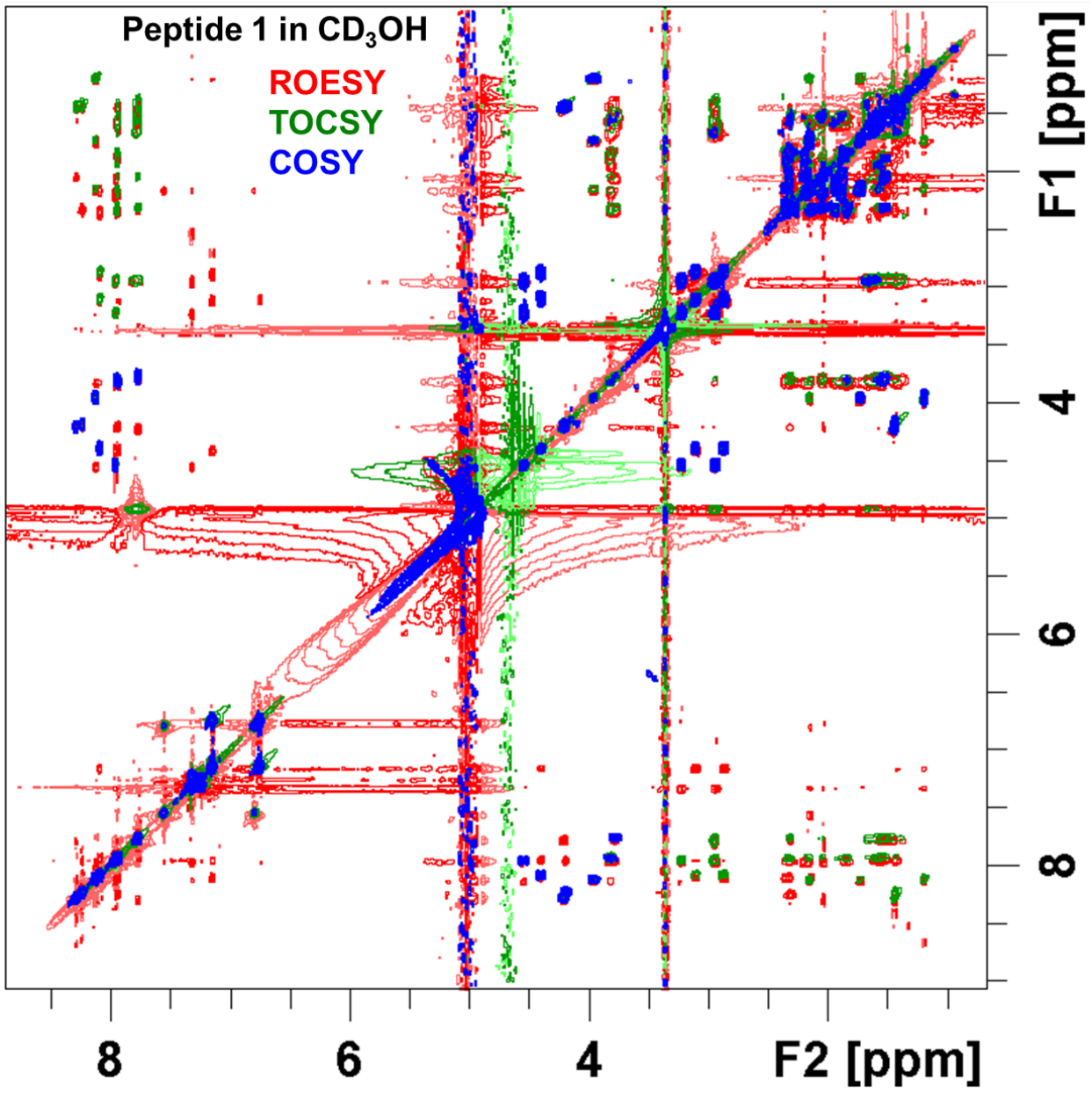

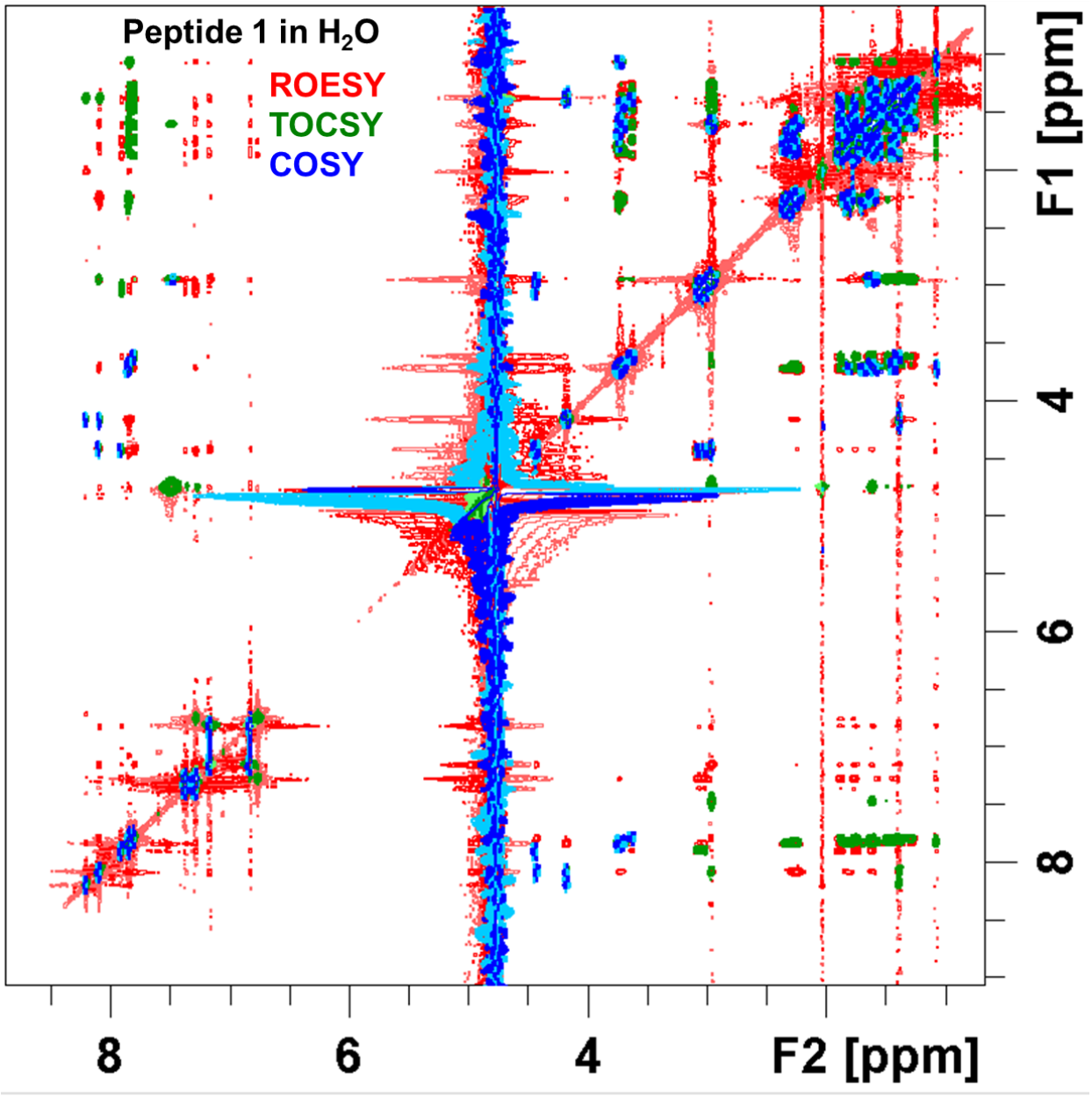
Peptide 1 in H_2O
ROESY
TOCSY
COSY
F1 [ppm]
4
6
8
8
6
4
F2 [ppm]

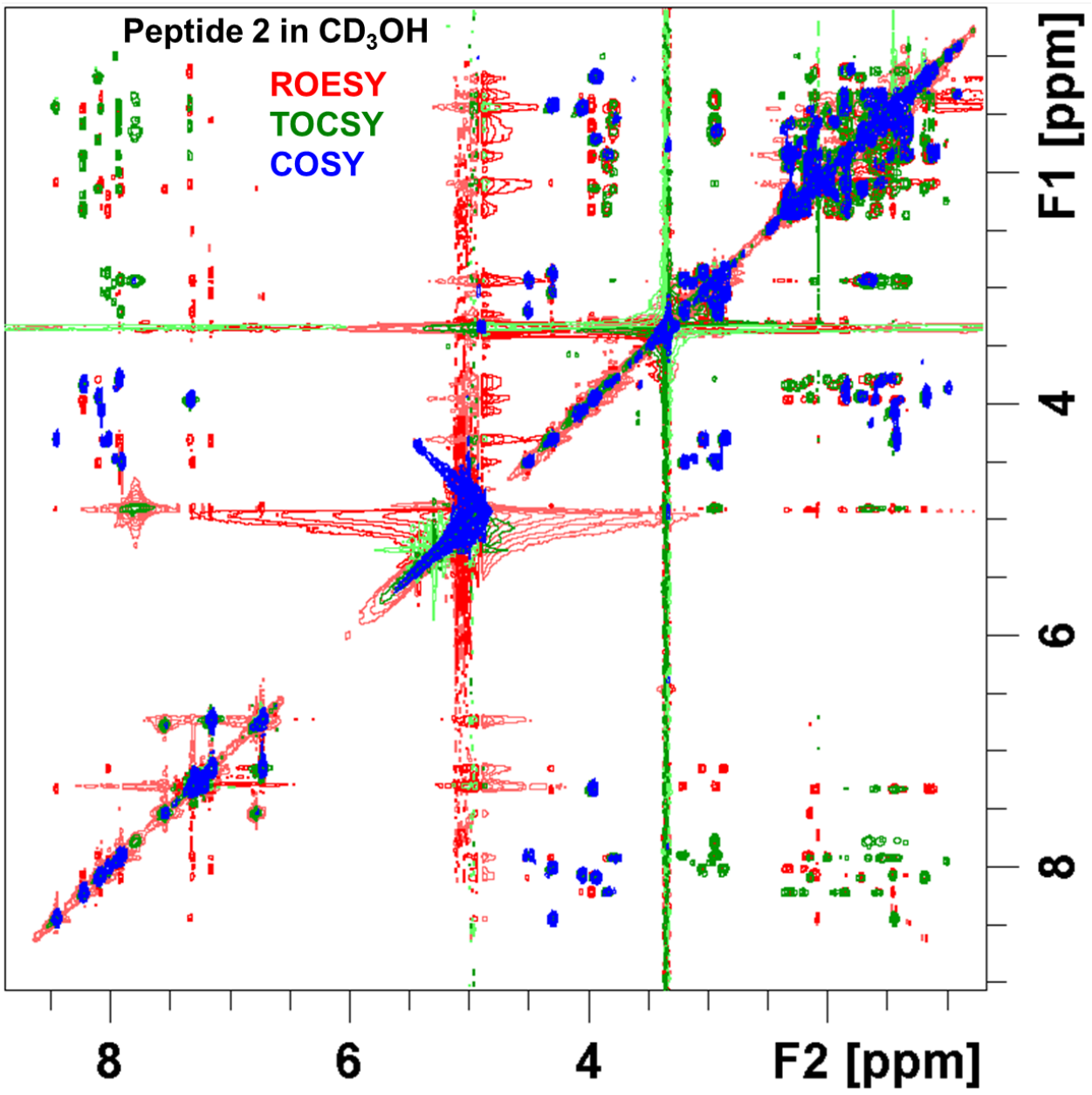
Peptide 2 in CD3OH
ROESY
TOCSY
COSY
F1 [ppm]
4
6
8
8
6
4
F2 [ppm]

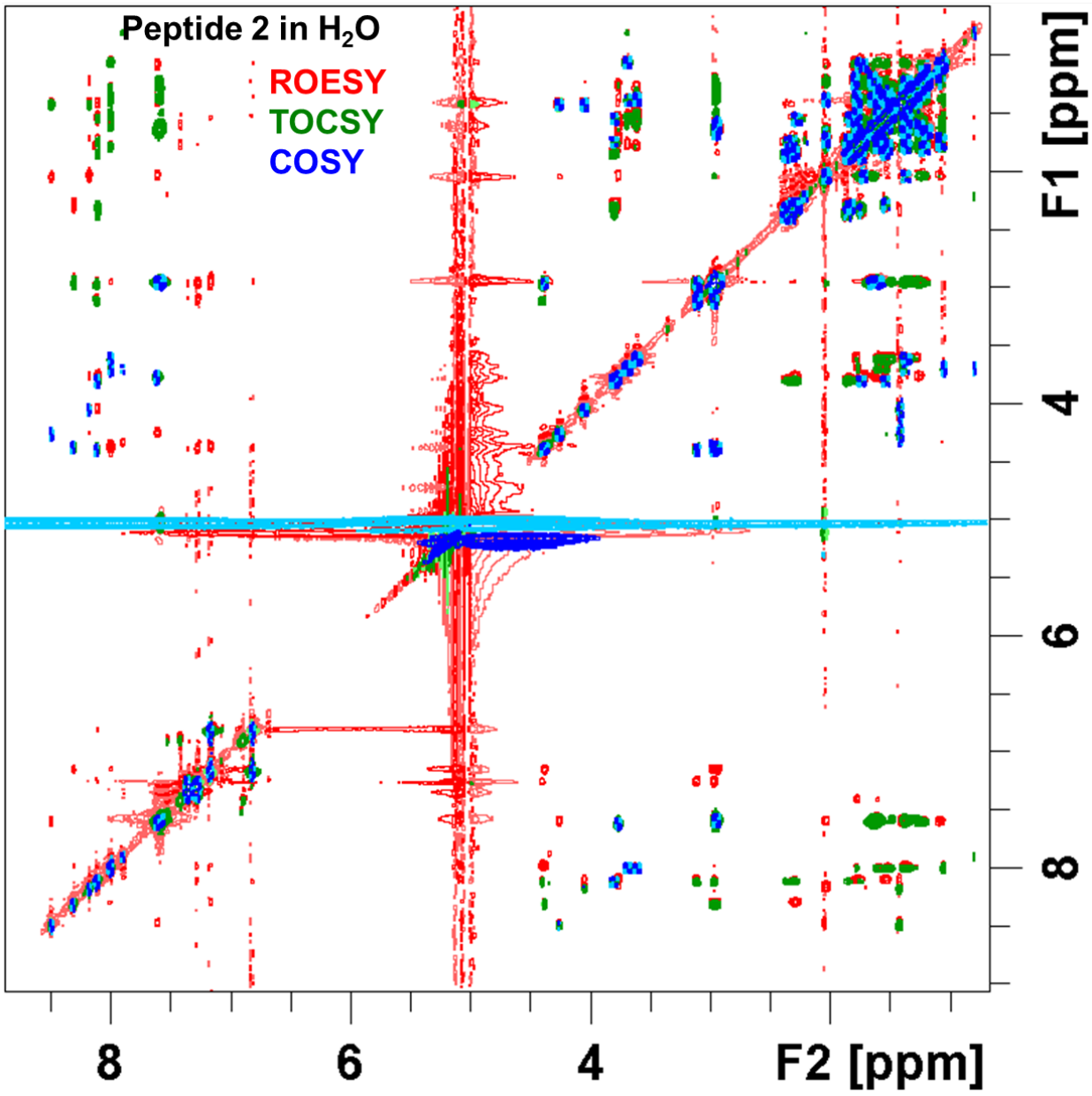
Peptide 2 in H_2O
ROESY
TOCSY
COSY
F1 [ppm]
4
6
8
8
6
4
F2 [ppm]

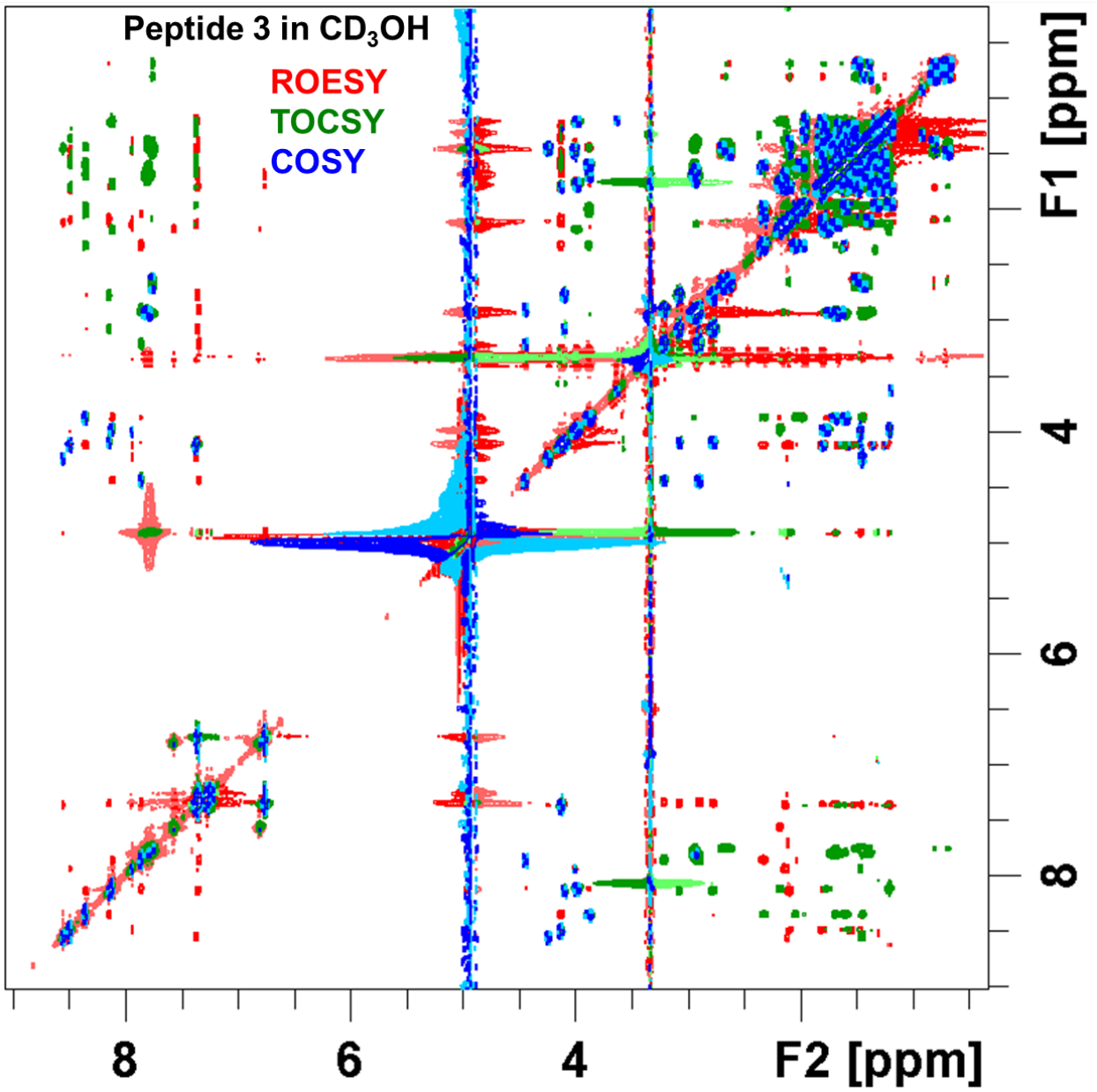
Peptide 3 in CD3OH
ROESY
TOCSY
COSY
F1 [ppm]
4
6
8
8
6
4
F2 [ppm]

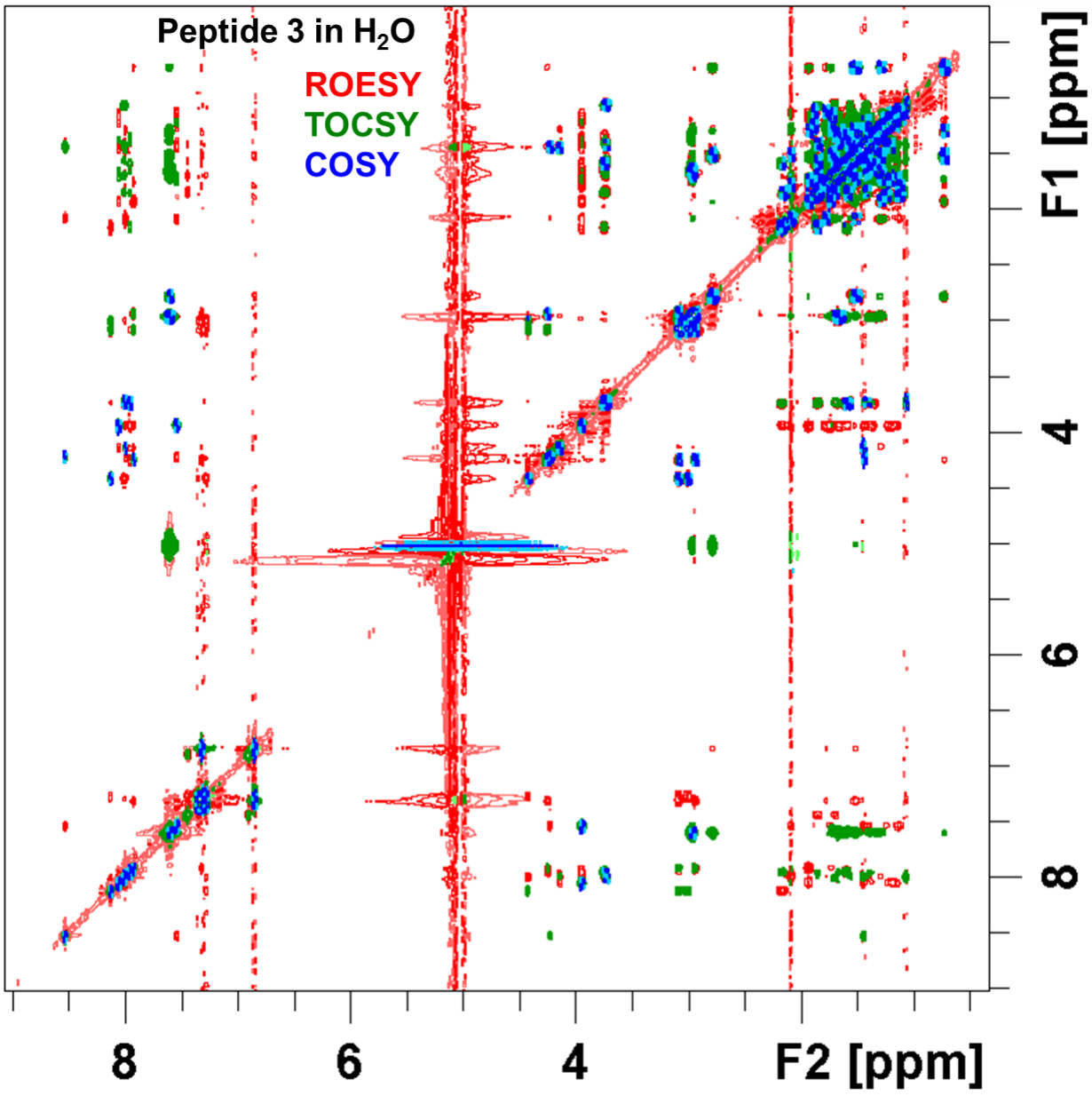
Peptide 3 in H_2O
ROESY
TOCSY
COSY
F1 [ppm]
8
6
4
F2 [ppm]

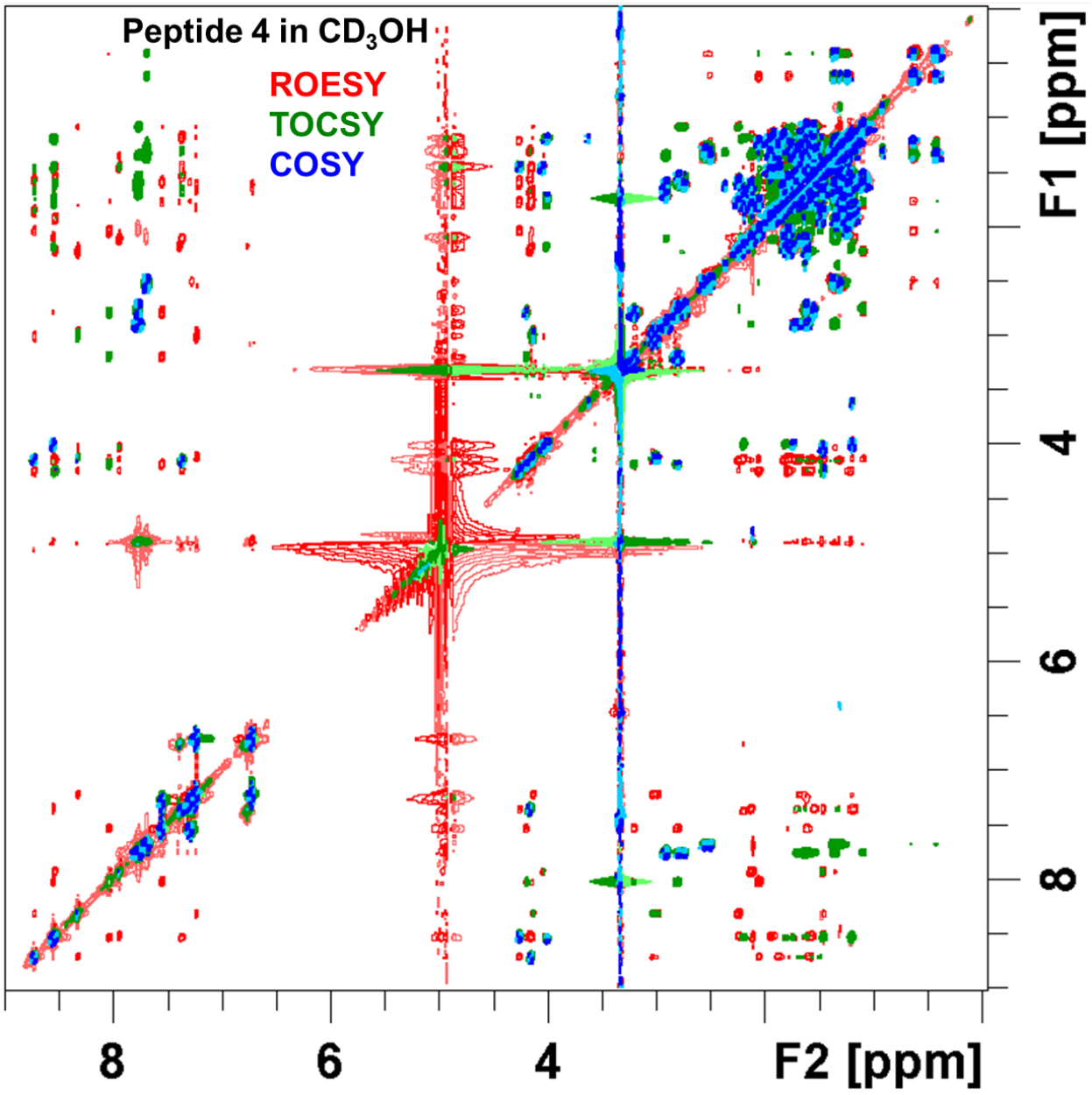
Peptide 4 in CD3OH
ROESY
TOCSY
COSY
F1 [ppm]
4
6
8
8
6
4
F2 [ppm]

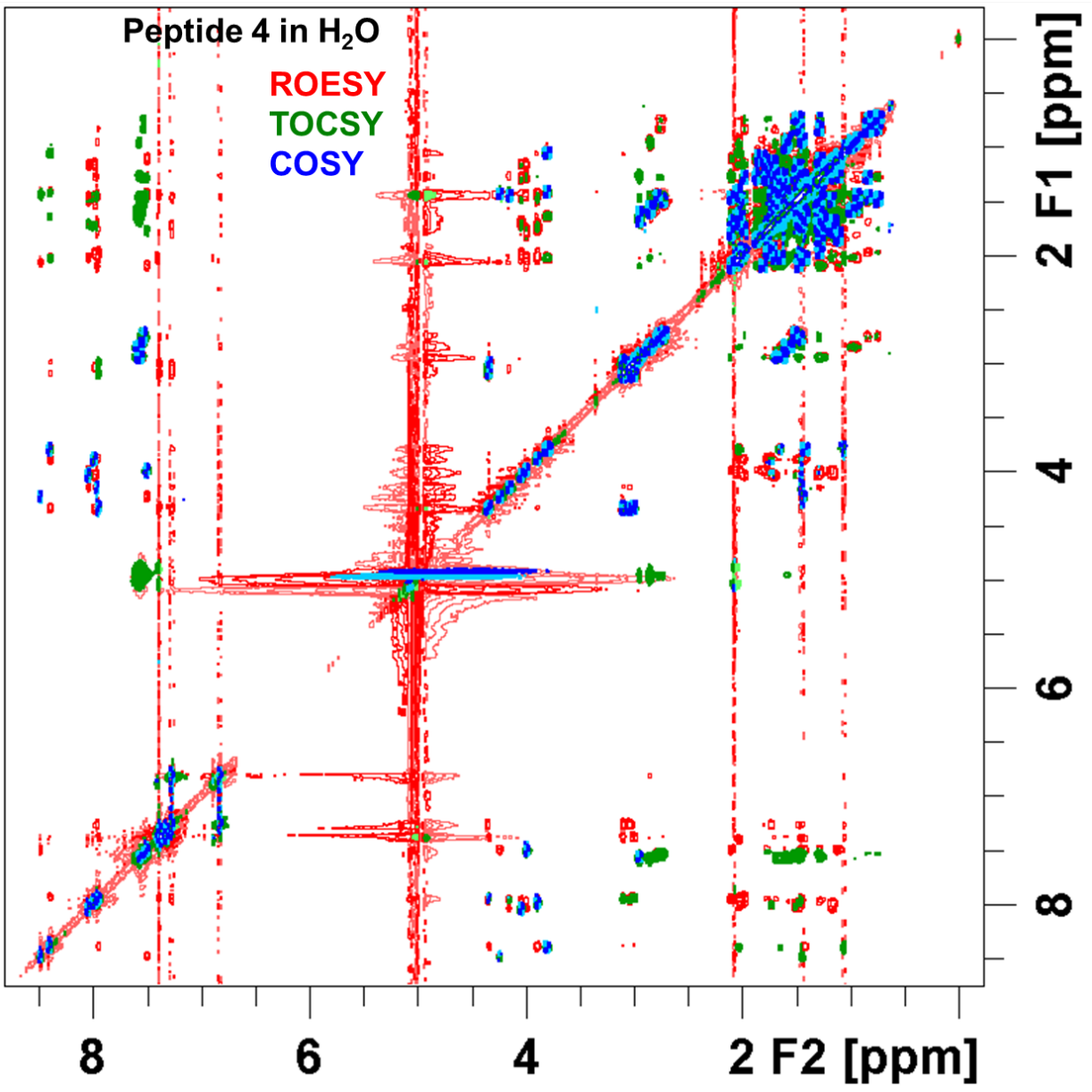

VIII. SI References

S1. (a) Akoka, S.; Barantin, L.; Trierweiler, M., *Anal. Chem.* **1999**, *71*, 2554; (b) Bharti, S. K.; Roy, R., *Trends Anal. Chem.* **2012**, *35*, 5.

S2. Castells, C. B.; Rafols, C.; Roses, M.; Bosch, E., *J. Chromatogr. A* **2003**, *1002*, 41.

S3. Lee, W.; Tonelli, M.; Markley, J. L., *Bioinformatics* **2015**, *31*, 1325.

S4. Wüthrich, K.; Wider, G.; Wagner, G.; Braun, W., *J. Mol. Biol.* **1982**, *155*, 311.

S5. Neuhaus, D.; Williamson, M. P., *The Nuclear Overhauser Effect in Structural and Conformational Analysis*; Wiley-VCH: New York, 2000.

S6. Kessler, H., *Angew. Chem. Int. Ed.* **1982**, *21*, 512.

S7. Dyson, H. J.; Wright, P. E., *Curr Opin Struc Biol* **1993**, *3*, 60.

S8. Rohl, C. A.; Scholtz, J. M.; York, E. J.; Stewart, J. M.; Baldwin, R. L., *Biochemistry* **1992**, *31*, 1263.

S9. Gademann, K.; Jaun, B.; Seebach, D.; Perozzo, R.; Scapozza, L.; Folkers, G., *Helv. Chim. Acta* **1999**, *82*, 1.

S10. Williamson, M. P.; Waltho, J. P., *Chem. Soc. Rev.* **1992**, *21*, 227.

S11. Jardetzky, O., *Biochim. Biophys. Acta* **1980**, *621*, 227.

S12. Nemeth, L. J.; Hegedus, Z.; Martinek, T. A., *J. Chem. Inf. Model.* **2014**, *54*, 2776.

S13. (a) Mierke, D. F.; Huber, T.; Kessler, H., *J Comput Aid Mol Des* **1994**, *8*, 29; (b) Case, D. A.; Dyson, H. J.; Wright, P. E., *Methods Enzymol.* **1994**, *239*, 392.

S14. Wang, A. C.; Bax, A., *J. Am. Chem. Soc.* **1995**, *117*, 1810.

S15. Pearlman, D. A., *J. Biomol. NMR* **1994**, *4*, 279.

S16. Smith, L. J.; Bolin, K. A.; Schwalbe, H.; MacArthur, M. W.; Thornton, J. M.; Dobson, C. M., *J. Mol. Biol.* **1996**, *255*, 494.

S17. Smith, L. J.; Fiebig, K. M.; Schwalbe, H.; Dobson, C. M., *Folding & design* **1996**, *1*, R95.

S18. Yao, J.; Dyson, H. J.; Wright, P. E., *FEBS Lett.* **1997**, *419*, 285.

S19. Wishart, D. S.; Sykes, B. D.; Richards, F. M., *Biochemistry* **1992**, *31*, 1647.

S20. Tremblay, M. L.; Banks, A. W.; Rainey, J. K., *J. Biomol. NMR* **2010**, *46*, 257.

S21. (a) Eghbalnia, H. R.; Wang, L.; Bahrami, A.; Assadi, A.; Markley, J. L., *J. Biomol. NMR* **2005**, *32*, 71; (b) Labudde, D.; Leitner, D.; Kruger, M.; Oschkinat, H., *J. Biomol. NMR* **2003**, *25*, 41.

S22. Wishart, D. S.; Sykes, B. D., *Methods Enzymol.* **1994**, *239*, 363.

S23. Wishart, D. S.; Sykes, B. D.; Richards, F. M., *J. Mol. Biol.* **1991**, *222*, 311.

S24. Baxter, N. J.; Williamson, M. P., *J. Biomol. NMR* **1997**, *9*, 359.

S25. Ohnishi, M.; Urry, D. W., *Biochem. Biophys. Res. Commun.* **1969**, *36*, 194.

S26. Andersen, N. H.; Neidigh, J. W.; Harris, S. M.; Lee, G. M.; Liu, Z. H.; Tong, H., *J. Am. Chem. Soc.* **1997**, *119*, 8547.

S27. Wagner, G.; Pardi, A.; Wüthrich, K., *J. Am. Chem. Soc.* **1983**, *105*, 5948.

S28. Andersen, N. H.; Chen, C. P.; Marschner, T. M.; Krystek, S. R., Jr.; Bassolino, D. A., *Biochemistry* **1992**, *31*, 1280.

S29. Englander, S. W.; Mayne, L.; Bai, Y.; Sosnick, T. R., *Protein Sci.* **1997**, *6*, 1101.

S30. Englander, S. W.; Sosnick, T. R.; Englander, J. J.; Mayne, L., *Curr Opin Struc Biol* **1996**, *6*, 18.

S31. Wagner, D. S.; Melton, L. G.; Yan, Y.; Erickson, B. W.; Anderegg, R. J., *Protein Sci.* **1994**, *3*, 1305.

S32. (a) Molday, R. S.; Englander, S. W.; Kallen, R. G., *Biochemistry* **1972**, *11*, 150; (b) Bai, Y.; Milne, J. S.; Mayne, L.; Englander, S. W., *Proteins* **1993**, *17*, 75.

S33. Hvidt, A.; Nielsen, S. O., *Adv. Protein Chem.* **1966**, *21*, 287.

S34. Fisher, B. F.; Guo, L.; Dolinar, B. S.; Guzei, I. A.; Gellman, S. H., *J. Am. Chem. Soc.* **2015**, *137*, 6484.

S35. Spera, S.; Bax, A., *J. Am. Chem. Soc.* **1991**, *113*, 5490.

S36. (a) Brünger, A. T.; Adams, P. D.; Clore, G. M.; DeLano, W. L.; Gros, P.; Grosse-Kunstleve, R. W.; Jiang, J. S.; Kuszewski, J.; Nilges, M.; Pannu, N. S.; Read, R. J.; Rice, L. M.; Simonson, T.; Warren, G. L., *Acta Crystallogr. D Biol. Crystallogr.* **1998**, *54*, 905; (b) Brunger, A. T., *Nat. Protoc.* **2007**, *2*, 2728.

S37. Nederveen, A. J.; Doreleijers, J. F.; Vranken, W.; Miller, Z.; Spronk, C. A.; Nabuurs, S. B.; Guntert, P.; Livny, M.; Markley, J. L.; Nilges, M.; Ulrich, E. L.; Kaptein, R.; Bonvin, A. M., *Proteins* **2005**, *59*, 662.

S38. *The PyMOL Molecular Graphics System, Version 1.7.0.3*, 1.7.0.3; Schrödinger, LLC.

S39. Kelly, S. M.; Jess, T. J.; Price, N. C., *Biochim. Biophys. Acta* **2005**, *1751*, 119.

S40. Gill, S. C.; von Hippel, P. H., *Anal. Biochem.* **1989**, *182*, 319.

S41. Dinesh, B.; Vinaya, V.; Raghothama, S.; Balaram, P., *European Journal of Organic Chemistry* **2013**, *2013*, 3590.

S42. (a) Glättli, A.; Daura, X.; Seebach, D.; van Gunsteren, W. F., *J. Am. Chem. Soc.* **2002**, *124*, 12972; (b) Niggli, D. A.; Ebert, M. O.; Lin, Z.; Seebach, D.; van Gunsteren, W. F., *Chem. Eur. J.* **2012**, *18*, 586.

S43. (a) Seebach, D.; Jaun, B.; Sebesta, R.; Mathad, R. I.; Flögel, O.; Limbach, M.; Sellner, H.; Cottens, S., *Helvetica Chimica Acta* **2006**, ; (b) Wang, D.; Freitag, F.; Gattin, Z.; Haberkern, H.; Jaun, B.; Siwko, M.; Vyas, R.; van Gunsteren, W. F.; Dolenc, J., *Helv. Chim. Acta* **2012**, *95*, 2562.

S44. (a) Bandyopadhyay, A.; Gopi, H. N., *Org. Lett.* **2012**, *14*, 2770; (b) Bandyopadhyay, A.; Jadhav, S. V.; Gopi, H. N., *Chem. Commun.* **2012**, *48*, 7170; (c) Basuroy, K.; Dinesh, B.; Shamala, N.; Balaram, P., *Angew. Chem. Int. Ed.* **2012**, *51*, 8736; (d) Dinesh, B.; Basuroy, K.; Shamala, N.; Balaram, P., *Tetrahedron* **2012**, *68*, 4374; (e) Basuroy, K.; Dinesh, B.; Reddy, M. B.; Chandrappa, S.; Raghothama, S.; Shamala, N.; Balaram, P., *Org. Lett.* **2013**, *15*, 4866; (f) Basuroy, K.; Dinesh, B.; Shamala, N.; Balaram, P., *Angew. Chem. Int. Ed.* **2013**, *52*, 3136; (g) Jadhav, S. V.; Bandyopadhyay, A.; Gopi, H. N., *Org. Biomol. Chem.* **2013**, *11*, 509; (h) Jadhav, S. V.; Gopi, H. N., *Chem. Commun.* **2013**, *49*, 9179; (i) Jadhav, S. V.; Misra, R.; Singh, S. K.; Gopi, H. N., *Chem. Eur. J.* **2013**, *19*, 16256; (j) Shin, Y. H.; Mortenson, D. E.; Satyshur, K. A.; Forest, K. T.; Gellman, S. H., *J. Am. Chem. Soc.* **2013**, *135*, 8149; (k) Jadhav, S. V.; Misra, R.; Gopi, H. N., *Chem. Eur. J.* **2014**, *20*, 16523; (l) Sonti, R.; Dinesh, B.; Basuroy, K.; Raghothama, S.; Shamala, N.; Balaram, P., *Org. Lett.* **2014**, *16*, 1656; (m) Ganesh Kumar, M.; Thombare, V. J.; Katariya, M. M.; Veeresh, K.; Raja, K. M. P.; Gopi, H. N., *Angew. Chem. Int. Ed.* **2016**, *55*, 7847.

S45. (a) Guo, L.; Chi, Y.; Almeida, A. M.; Guzei, I. A.; Parker, B. K.; Gellman, S. H., *J. Am. Chem. Soc.* **2009**, *131*, 16018; (b) Guo, L.; Almeida, A. M.; Zhang, W.; Reidenbach, A. G.; Choi, S. H.; Guzei, I. A.; Gellman, S. H., *J. Am. Chem. Soc.* **2010**, *132*, 7868; (c) Guo, L.; Zhang, W.; Reidenbach, A. G.; Giuliano, M. W.; Guzei, I. A.; Spencer, L. C.; Gellman, S. H., *Angew. Chem. Int. Ed.* **2011**, *50*, 5843; (d) Guo, L.; Zhang, W.; Guzei, I. A.; Spencer, L. C.; Gellman, S. H., *Tetrahedron* **2012**, *68*, 4413; (e) Kusaka, R.; Zhang, D.; Walsh, P. S.; Gord, J. R.; Fisher, B. F.; Gellman, S. H.; Zwier, T. S., *J. Phys. Chem. A* **2013**, *117*, 10847.

S46. Baldauf, C.; Gunther, R.; Hofmann, H. J., *J. Org. Chem.* **2006**, *71*, 1200.

S47. Baldauf, C.; Günther, R.; Hofmann, H. J., *Helv. Chim. Acta* **2003**, *86*, 2573.

S48. Frisch, M. J.; Trucks, G. W.; Schlegel, H. B.; Scuseria, G. E.; Robb, M. A.; Cheeseman, J. R.; Scalmani, G.; Barone, V.; Mennucci, B.; Petersson, G. A.; Nakatsuji, H.; Caricato, M.; Li, X.; Hratchian, H. P.; Izmaylov, A. F.; Bloino, J.; Zheng, G.; Sonnenberg, J. L.; Hada, M.; Ehara, M.; Toyota, K.; Fukuda, R.; Hasegawa, J.; Ishida, M.; Nakajima, T.; Honda, Y.; Kitao, O.; Nakai, H.; Vreven, T.; Montgomery Jr., J. A.; Peralta, J. E.; Ogliaro, F.; Bearpark, M. J.; Heyd, J.; Brothers, E. N.; Kudin, K. N.; Staroverov, V. N.; Kobayashi, R.; Normand, J.; Raghavachari, K.; Rendell, A. P.; Burant, J. C.; Iyengar, S. S.; Tomasi, J.; Cossi, M.; Rega, N.; Millam, N. J.; Klene, M.; Knox, J. E.; Cross, J. B.; Bakken, V.; Adamo, C.; Jaramillo, J.; Gomperts, R.; Stratmann, R. E.; Yazyev, O.; Austin, A. J.; Cammi, R.; Pomelli, C.; Ochterski, J. W.; Martin, R. L.; Morokuma, K.; Zakrzewski, V. G.; Voth, G. A.; Salvador, P.; Dannenberg, J. J.; Dapprich, S.;

Daniels, A. D.; Farkas, Ö.; Foresman, J. B.; Ortiz, J. V.; Cioslowski, J.; Fox, D. J. *Gaussian 09*, Gaussian, Inc.: Wallingford, CT, USA, 2009.

S49. Jeffrey, G. A., *An Introduction to Hydrogen Bonding*; Oxford University Press: New York, 1997.

S50. Wood, P. A.; Pidcock, E.; Allen, F. H., *Acta Crystallogr. B Struct. Sci.* **2008**, *64*, 491.

S51. Taylor, R.; Kennard, O.; Versichel, W., *Acta Crystallogr. B Struct. Sci.* **1984**, *40*, 280.

S52. Allen, F. H.; Harris, S. E.; Taylor, R., *J. Comput. Aided Mol. Des.* **1996**, *10*, 247.